

PAYMAN YADOLLAHPOUR

EXPLORING AND EXPLOITING DIVERSITY FOR IMAGE
SEGMENTATION

arXiv:1709.01625v1 [cs.CV] 5 Sep 2017

EXPLORING AND EXPLOITING DIVERSITY FOR IMAGE SEGMENTATION

by

PAYMAN YADOLLAHPOUR



A thesis submitted in partial fulfillment of the requirements for the degree of

Doctor of Philosophy in Computer Science

at the

TOYOTA TECHNOLOGICAL INSTITUTE AT CHICAGO
Chicago, IL

February 2017

Thesis committee:

Dr. Gregory Shakhnarovich (Thesis Advisor)

Dr. Dhruv Batra

Dr. Amir Globerson

Dr. David McAllester

Dr. Nathan Srebro

EXPLORING AND EXPLOITING DIVERSITY FOR IMAGE SEGMENTATION

A thesis presented
by
PAYMAN YADOLLAHPOUR

in partial fulfillment of the requirements for the degree of
Doctor of Philosophy in Computer Science
TOYOTA TECHNOLOGICAL INSTITUTE AT CHICAGO
Chicago, IL

February 2017

—Thesis Committee —

Dr. Dhruv Batra		Feb 06, 2017
Committee member	Signature	Date
Dr. Amir Globerson		Feb 06, 2017
Committee member	Signature	Date
Dr. Nathan Srebro		Feb 06, 2017
Committee member	Signature	Date
Dr. Gregory Shakhnarovich		Feb 06, 2017
Thesis/Research Advisor	Signature	Date
Dr. David McAllester		Feb 06, 2017
Chief Academic Officer	Signature	Date

Dedicated to my parents.

ABSTRACT

Semantic image segmentation is an important computer vision task that is difficult because it consists of both recognition and segmentation. It is important because it subsumes important aspects of scene understanding such as image classification and object localization. The task is often cast as a structured output problem on an exponentially large output-space, which is typically modeled by a discrete probabilistic model. The best segmentation is found by inferring the Maximum a-Posteriori (MAP) solution over the output distribution defined by the model. Due to limitations in optimization, the model cannot be arbitrarily complex. This leads to a trade-off: devise a more accurate model that incorporates rich high-order interactions between image elements at the cost of inaccurate and possibly intractable optimization OR leverage a tractable model which produces less accurate MAP solutions but may contain high quality solutions as other modes of its output distribution.

This thesis investigates the latter and presents a two stage approach to semantic segmentation akin to cascade models and proposal generation works. In the first stage a tractable segmentation model outputs a set of high probability segmentations from the underlying distribution that are not just minor perturbations of each other. Critically the output of this stage is a diverse set of plausible solutions and not just a single one. The first stage reduces the exponential space of solutions to just a handful of segmentations. In the second stage, a discriminatively trained re-ranking model selects the best segmentation from this set. The re-ranking stage can use much more complex features than what could be tractably used in the segmentation model, allowing a better exploration of the solution space than possible by simply producing the most probable solution from the segmentation model. The formulation of the first stage is agnostic to the underlying segmentation model (e.g. CRF, CNN, etc.) and optimization algorithm, which makes it applicable to a wide range of models and inference methods.

Evaluation of the approach on a number of semantic image segmentation benchmark datasets highlight its superiority over inferring the MAP solution.

PUBLICATIONS

The ideas and figures in this thesis have appeared previously in the following publications:

- [1] Dhruv Batra, Payman Yadollahpour, Abner Guzman-Rivera, and Gregory Shakhnarovich. “Diverse m-best solutions in markov random fields.” In: *European Conference on Computer Vision*. Springer. 2012, pp. 1–16.
- [2] Payman Yadollahpour, Dhruv Batra, and Gregory Shakhnarovich. “Discriminative re-ranking of diverse segmentations.” In: *Proceedings of the IEEE Conference on Computer Vision and Pattern Recognition*. 2013, pp. 1923–1930.
- [3] Payman Yadollahpour and Gregory Shakhnarovich. “Region ranking for figure-ground segmentation.” 2014.

ACKNOWLEDGMENTS

My deepest gratitude goes to my research advisor Dr. Gregory Shakhnarovich for continual guidance and stewardship of my graduate career. He has been a major source of insight and has significantly contributed to my understanding of Computer Vision and Machine Learning disciplines. I would also like to thank Dr. Dhruv Batra for his research collaboration, and much of this thesis owes to the joint collaboration I had with him and Greg. A big thanks to Dr. Ayan Chakrabarti for the many insightful discussions on my thesis.

I would like to mention my appreciation to the entire faculty at Toyota Technological Institute at Chicago for their insistence on research excellence and for making TTIC a leading graduate research institution.

I'd like to give special thanks to my fellow students at Toyota Technological Institute at Chicago, for making the many years enjoyable and the many fruitful discussions. I'd like to especially thank Avleen Bijral, Andrew Cotter, Heejin Choi, Somaye Hashemifar, Taehwan Kim, Gustav Larsson, Mohammadreza Mostajabi, Jian Peng, Karthik Sridharan, Siqi Sun, Hao Tang, Behnam Tavakoli, Shubhendu Trivedi, Zhiyong Wang, and Feng Zhao. I also owe gratitude to Steven Basart, Falcon Dai, Suriya Gunasekar, Nicholas Kolkin, and Mohammadreza Mostajabi, for giving me very useful feedback on my thesis draft.

Lastly, I would like to thank my family for being a source of support and for their patience these many years.

CONTENTS

1	INTRODUCTION	1
1.1	Segmentation	2
1.1.1	Methods	7
1.2	MAP Problem	28
2	DIVMBEST	37
2.1	Related Work	39
2.1.1	M-BEST	39
2.1.2	M-BEST and Max-Flow Propagation	41
2.1.3	M-BEST solutions for loopy graphs and the BMMF algorithm	46
2.1.4	M-BEST MAP and its linear programming formulation	48
2.1.5	M-BEST MAP LP when G is a tree	49
2.1.6	M-BEST MAP LP when G is a general graph	49
2.2	DivMBest Algorithm	51
2.2.1	Overview	53
2.2.2	Contributions	54
2.2.3	Notation	54
2.2.4	MAP problem	54
2.2.5	MAP integer program and its LP relaxation	55
2.2.6	<i>Div</i> MBEST: Formulation	56
2.2.7	<i>Div</i> MBEST: Lagrangian Relaxation and the Lagrangian dual function	57
2.2.8	Diversity Functions	58
2.2.9	Supergradient Ascent on Lagrangian dual function	60
2.2.10	How tight is the Lagrange relaxation?	61
2.2.11	Computing Supergradient under different diversity functions	63
2.2.12	Dual-Decomposition and the approximate supergradient for higher order potentials	64
2.2.13	Setting k: the amount of diversity	65
2.2.14	Summary	65
3	DIVMBEST+RERANK	67
3.0.1	Contributions	68
3.1	Related Work	69
3.1.1	Relation to cascade approaches	70
3.1.2	Relation to proposal-generation methods	72
3.1.3	Discriminative re-ranking in other domains.	73
3.2	DivMBest + Re-rank	74
3.2.1	Notation	74
3.2.2	Re-ranker model	75

3.2.3	Re-ranker loss	76
3.2.4	Summary	78
4	DIVMBEST EXPERIMENTS	81
4.1	Evaluating DivMBest segmentations	81
4.1.1	Baselines	81
4.1.2	Oracle Solution	82
4.2	Interactive Segmentation	82
4.2.1	CRF Model	82
4.2.2	Interactive segmentation + <i>DivMBEST</i>	84
4.2.3	Experiments	86
4.3	Figure-ground Segmentation	87
4.3.1	CRF Model	88
4.3.2	CRF potentials	88
4.3.3	Features	89
4.3.4	CRF learning	91
4.3.5	Task loss	92
4.3.6	Loss-augmented inference	92
4.3.7	<i>DivMBEST</i> inference with Hamming dissimilarity	93
4.3.8	Superpixels	93
4.3.9	Experiments	93
4.4	Multi-category segmentation	96
4.4.1	Hierarchical model	96
4.4.2	Feed-forward model	98
4.4.3	Convolutional neural network + dense CRF model	99
4.4.4	Summary	101
5	DIVMBEST+RERANK EXPERIMENTS	107
5.1	Evaluating DivMBest+ReRank pipeline	107
5.2	Figure-ground Segmentation	107
5.2.1	Re-ranking segmentations	107
5.2.2	Ranking features	108
5.2.3	Re-ranker training	108
5.2.4	Results	109
5.3	Multi-category segmentation	110
5.3.1	Dataset	110
5.3.2	Hierarchical model	110
5.3.3	Feed-forward model	110
5.3.4	Diversity and Oracles	111
5.3.5	Re-ranker features	116
5.3.6	Re-ranker training	117
5.3.7	Re-ranker results	117
5.3.8	Re-ranker Analysis	118
5.3.9	Human Ranking Experiments	118
5.3.10	Summary	119

6	CONCLUSION	123
	BIBLIOGRAPHY	125
I	APPENDIX	137
A	APPENDIX A	139
A.1	Sample of DivMBest solutions from figure-ground model	139
A.2	Sample of results when DivMBest is applied to multi-category segmentation	139
B	APPENDIX B	141
B.1	Example Re-ranking Results	141
B.2	Highest ranked vs. MAP	142

LIST OF FIGURES

Figure 1.1	Bottom-up segmentation using normalized <i>k-way cut</i> algorithm as a function of the number of segments (top eigenvectors), k . Note that a segment can consists of multiple disconnected components (<i>e.g.</i> segment on nose of horse).	12
Figure 1.2	SLIC superpixel results as a function of the desired number, k , and compactness, m . As m is increased the superpixels exhibit more regular appearance, aligning less with image contours and more with spatial grid.	15
Figure 1.3	For a given superpixel (red) zoom-out features are computed at multiple zoom-out levels (6 levels shown). The features from each level are stacked into a column vector representation of the superpixel, and a multi-layer perceptron is used to predict the superpixel class probabilities.	24
Figure 1.4	Examples of zoom-out regions. We show four out of fifteen levels: 1 (cyan, nearly matching the superpixel boundaries), 6 (olive), 10 (purple) and 13 (blue).	26
Figure 1.5	Zoom-out network architecture using an image classification CNN backbone, computed over superpixels. The output response from the convolutional layers plus the softmax output (scene level) are up-sampled to the image size and stacked into the final feature map representation over the image. For each superpixel a feature vector representation is constructed by pooling the feature map over the superpixel.	27
Figure 1.6	Example semantic segmentation on VOC2012 val images using a 3-layer perceptron classifier used to classify zoom-out features over superpixels across 15 zoom-out levels of a CNN originally trained for scene classification.	28
Figure 2.1	Semantic segmentations on test images from PASCAL VOC 2010. For each image, from left: input image, MAP segmentation, best out of 10 modes obtained with <i>DivMBEST</i>	53
Figure 2.2	Interactive segmentations. For each image, from left: input image, MAP solution, 2^{nd} best MAP, and the 2^{nd} best mode obtained with <i>DivMBEST</i>	53

Figure 3.1	An overview of the <i>DivMBEST+RE-RANK</i> approach. In <i>Stage 1</i> diverse segmentations are computed from a tractable probabilistic model. These are fed to a large-margin re-ranker in <i>Stage 2</i> . The top re-ranked segmentation is returned as the final solution. Even though the most probable segmentation from Stage 1 is incorrect, the set of segmentations does contain an accurate solution, which the re-ranker is able to score to the top.	68
Figure 4.1	<i>DivMBEST</i> modes under cardinality-based HOP. From left-to-right: image-scribble pair (X, S) , MAP solution, 2 nd -mode, . . . , 6 th -mode. The modes are ordered in increasing size of foreground object.	86
Figure 4.2	Examples of (left to right) input image with ground truth, MAP from the bottom-up CRF model, <i>oracle</i> out of 10 diverse solutions. All examples are from the test portions of Graz data sets.	102
Figure 4.3	Examples of (left to right) input image with ground truth, MAP from the bottom-up CRF model, <i>oracle</i> out of 10 diverse solutions. Examples are from the test portion of Weizmann horses data set, and from one of the test folds of the Ultrasound data set. Last row shows some failures.	103
Figure 4.4	(a) <i>Oracle</i> accuracy vs. number solutions on VOC2010 val for <i>DivMBEST</i> (red) and <i>confidence</i> based perturbations (blue), along with MAP performance (black dashed). (b) Mean hamming distances between each <i>mode</i> (<i>DivMBEST</i> solution) and the MAP solution (red), and average to previous <i>modes</i> (blue), normalized by image size on PASCAL VOC 2010 val set. Also show, histogram of energies (as % of MAP) over (c) 6 <i>modes</i> , (d) 31 <i>modes</i> , on validation set. The bar to the left of red vertical lines indicate number of <i>modes</i> with energy less than or equal to MAP.	104
Figure 4.5	<i>Oracle</i> performance (IoU accuracy against ground-truth) on PASCAL VOC 2012 val, when (a) selecting best-out-of- <i>m</i> solutions, and (b) composing full image labellings from connected components found among <i>m</i> solutions.	105
Figure 4.6	Result of composing solutions from <i>DivMBEST</i> segments. Second and third row show a subset of 40 <i>DivMBEST</i> segmentations generated from the CNN+CRF model of § 4.4.3. First row shows in order the image, ground-truth segmentation, and composed segmentation <i>oracle</i> using the second approach of § 4.4.3.2. Note how the composed segmentation <i>oracle</i> is a much better segmentation of the image than the MAP solution (first segmentation in the second row).	105
Figure 5.1	<i>DivMBEST+RE-RANK</i> performance on PASCAL VOC 2012 val using (a) ALE and (b) O ₂ P models vs. the number of solutions.	112
Figure 5.2	(a) Average minimum-covering (5.3) of MAP in the first $j \leq 10$ solutions vs. <i>j</i> . (b) Accuracy of an <i>oracle</i> restricted to labels present in the MAP, or (c) restricted to masks present in MAP. See text for details.	115

Figure 5.3	Statistics on PASCAL VOC 2012 val with O ₂ P model: (a),(b) show the number of images in which the <i>oracle</i> / top-re-ranked solution was originally at rank $j \leq 10$. We can see that there is a heavy tail in the oracle distribution, but a much lighter tail in the re-ranker, suggesting that the re-ranker “plays it safe” and predicts MAP very frequently; (c) shows a scatter plot of re-ranker score vs solution accuracy.	120
Figure 5.4	Cases where O ₂ P-DivMBEST+RE-RANK outperforms O ₂ P-MAP. In each group of images, the first column shows the original image followed by the ground-truth, MAP, and top re-ranked solution returned by DivMBEST+RE-RANK. PASCAL intersection-over-union accuracy is shown below the segmentations.	121
Figure 5.5	Example MTurk tasks along with user-provided responses which were instructive in the creation of segmentation-specific features.	122

LIST OF TABLES

Table 4.1	Superpixel features used to learn the appearance model for the interactive segmentation figure-ground cutout model.	83
Table 4.2	Interactive segmentation: pixel accuracies averaged over 50 test images.	87
Table 4.3	Segmentation performance on all data sets, in IoU values $\times 100$. MAP: single solution from the bottom-up CRF model. <i>Oracle</i> : (hindsight) best of 10 diverse solutions from the CRF. Third column: percentage of gap (oracle-MAP) recovered by the ranking. Last column: Figure-ground segmentation model of Kuettel <i>et al.</i> [66].	95
Table 4.4	Pascal VOC 2010 val set accuracies for ALE model.	97
Table 4.5	Pascal VOC 2010 test set accuracies for ALE model.	97
Table 5.1	Segmentation performance on all data sets, in IoU values $\times 100$. MAP: single solution from the bottom-up CRF model. <i>Oracle</i> : (hindsight) best of 10 diverse solutions from the CRF. Ranking: full ranking model (all features). last column: percentage of gap (oracle-map) recovered by the ranking.	109
Table 5.2	Comparative results between methods and feature sets for region ranking. All numbers are IoU $\times 100$. Shape: only shape and position. Textons: only textons. Color: only color histograms. full-entropy: shape, color and textons, but not their entropies. .	109

Table 5.3	Average covering score between oracle solutions and MAP: <i>(left)</i> show the category-independent measure and <i>(right)</i> shows the category-specific measure.	114
Table 5.4	PASCAL VOC 2012 test set accuracies.	116
Table 5.5	<i>(left)</i> Human accuracy in predicting <i>(Best-vs-Worst)</i> , <i>(M)AP-vs-(W)orst</i> , and <i>(Best-vs-(M)AP)</i> solutions. <i>(right)</i> Pascal VOC accuracies over 150 images for best, MAP, worst, and human response (HR) solutions. . .	118

INTRODUCTION

The task of automatically labeling every pixel in an image with the category label of the object it covers is an important computer vision problem. Known as full image labelling or semantic segmentation – because it partitions the image into semantically coherent regions – it is one valuable proxy for measuring how well a system can reason about what is being depicted in an image. It subsumes important aspects of scene understanding such as image classification and object localization. While its importance as an end task is debatable it is a more refined proxy for measuring a system’s discriminative capability on a finite set of object classes than image classification or object detection. This is because the prediction must be made over local regions in the image as opposed to a global prediction over the entire image or simple bounding boxes over objects.

Image segmentation is typically modelled either probabilistically, via Conditional or Markov Random Fields (CRFs/MRFs) or using discriminative feed forward approaches. Feed forward approaches include cascade type systems that first predict region proposals and then predict their most likely labels and heuristically paste the labelled regions into the image. More recently, neural network models for segmentation have been proposed, including Convolutional Neural Networks (CNNs) [42, 82] and Recursive Neural Networks [43], which achieve state-of-the-art accuracy on many difficult image segmentation benchmarks.

Semantic segmentation is a task that has a structured output space; the variables of interest (namely image regions such as pixels or superpixels) are not independent of each other, but rather must be predicted jointly. Given this fact and that the output space of possible labellings of the variables is exponential in size introduces certain limitations on how we can jointly model, train, and infer the variables. For instance, in order to be able to train and run inference, CRF or MRF models often make simplifying independence assumptions over the variables, either by limiting clique sizes, or approximating the partition function. The different sources of error – approximation error due to a poor choice of model class, optimization error due to limitations on optimizing over the variables of interest, and estimation error due to a finite training set – all contribute to the quality of the final predicted segmentation. Because of all these sources of error the predicted probability distribution over the output labeling might be significantly different from the true distribution. Thus the most probable label returned under the model distribution might not be the most probable under the true distribution.

One way to alleviate this is to build more complex models that can capture the complex interactions of the variables, at the cost of making learning and inference (i.e. optimization) more expensive or possibly intractable. In this thesis we explore an alternate approach. Instead of increasing model complexity at the cost of optimization complexity, we propose a framework whereby we can find a small set of highly probable and yet diverse segmentations (“modes”) under the model. By virtue of the fact that this “mode” finding algorithm has exponentially reduced the space of segmentations we need to consider, we can evaluate each of them using arbitrarily complex features that can take into account dependencies between variables that would be intractable to capture in the original model. Because of the exponential space of possible segmentations, producing this “handful” of highly probable yet diverse segmentations is going to require an approach that is more nuanced than simply enumerating all possible solutions under the model.

We show that combining this mode finding algorithm with an automatic approach to selecting the best segmentation from this smaller set leads to a framework that produces state-of-the-art results on challenging semantic segmentation datasets. It is also general enough to be applicable to a wide variety of problems in vision and elsewhere.

THESIS OUTLINE This chapter presents a review of the segmentation problem, and outlines some common approaches to it, citing related literature – specifically algorithms for *bottom-up* and *top-down* segmentation. The chapter closes with presentation of the well known MAP inference problem and its integer programming formulation which will become relevant in the formulation of the *DivMBEST* problem. Chapter 2 reviews a number of approaches for inferring multiple solutions from a discrete probabilistic model, instead of just the MAP solution and explains why they are not adequate for improving image segmentation. Chapter 2 concludes with presentation of an alternate approach called the *DivMBEST* problem — which leverages existing segmentation models, and algorithms used to do inference over them, in order to produce sets of high-quality segmentations that are diverse. Chapter 3 presents a discriminatively trained re-ranking model that selects the best segmentation from this set. Evaluation of the *DivMBEST* and *DivMBEST+RERANK* methods on a number of semantic segmentation tasks is presented in chapter 4 and chapter 5 respectively.

1.1 SEGMENTATION

The task of partitioning all or some of the pixels in an image into coherent regions is known as image segmentation. When the regions take on semantic labels, the partitioning is known as semantic segmentation — a major topic of this thesis. The non-semantic segmentation problem is ill-posed because what we mean by a segment is

not clearly defined — for example a segment might belong to a single or multiple connected components throughout the image. A primary goal of segmentation is to have pixels within segments share a consistent property or feature. This is another reason why segmentation is ill-posed because consistent property is problem specific. For example, a common property we find in the output of most segmentation algorithms is that pixels that fall within the same segment are all within a local spatial neighborhood in the image. This property is not necessarily required however. Other features that do not require it such as color and texture statistics of the regions around a pixel [24, 27], pixel depth information [40], image contour strength [3], can be considered depending on the segmentation task. A third reason, specific to non-semantic segmentation, is that we do not explicitly associate meaning with the individual segments. The segments could correspond to low-level image cues like regions of constant color or texture or could be associated with semantic meanings such as physical objects or parts of objects. Given an image if you were to ask a set of people to segment the image we would end up getting multiple interpretations of what is a good segmentation of that image.

Semantic segmentation, however, is a much better posed problem since the output label space is well defined (e.g. object classes). That is to say, one common semantic segmentation task that we care to define is labelling every image region (e.g. pixel or superpixel) with the appropriate object class that it is a part of in the image.

As the above examples of segmentation features illustrate, one axis along which we can define different segmentation algorithms is based on the features used to capture local information relative to pixels in the image. If the segmentation task is to partition the full image into spatially coherent segments where pixels within a segment have similar color, spatial, depth, or boundary statistics such as curvature — this is known as low-level, or bottom-up, image segmentation. On the other hand, in the case of semantic segmentation (also known as semantic image parsing), the pixels corresponding to a segment share similar semantic properties (such as a *pixel part of sky in image*). Additionally, if the semantic categories are limited to foreground objects and background clutter the partitioning is referred to as figure-ground, or simply, foreground segmentation. Segmentation can also be with respect to 3D cues of the objects, such as surface orientation or material properties [44].

Typically bottom-up image segmentation algorithms partition the image into disjoint segments. The union of segments is equal to the entire image; in other words the segmentation covers the entire image. In semantic segmentation whether the partitioning covers the entire image depends on the semantic categories considered and how the algorithm partitions the image. For instance, the algorithm could assign the area in the image not covered by the segments explicitly labeled with semantic categories to a catch-all category such as *background*, *don't care*, or *unknown* label. On the other hand the algorithm might explicitly try to predict ambiguous segments in the image as a

specific category onto itself such as *stuff*, in which case the partitioning might not cover the entire image.

The size and shape statistics of the segment that we get as the output from segmentation algorithms also differs depending on the image information used for segmentation, as well as the algorithm details itself. For example in semantic segmentation the desired segment shapes and sizes are governed by shapes and sizes of the objects depicted in the images. On the other hand the output of low-level segmentation algorithms such as SLIC [1] produce *over-segmentations* of the image, where segments exhibit nearly uniform shape and size with small spatial support. Usually, low-level segmentations that over-segment an image are a first step towards some other more complex downstream task, such as semantic segmentation. These segments provide convenient and predictable objects for downstream processing due to their consistent shape and size. That is not to say that the output of all low-level algorithms exhibit this regularity in size and shape. For example hierarchical image segmentation approaches [100], which do a bottom-up grouping of image regions, and segmentation based image contour detection [3] produce low level image segmentation results where segments can have a variety of shapes and sizes.

It is common to refer to segments that are the result of low-level image segmentation algorithms as *superpixels*. Analogously for 3-dimensional segmentation the 3D regions are referred to as *supervoxels*. Generally what is referred to as a superpixel is the result of an over segmentation of an image, and initially there is no semantic meaning associated with the superpixel. Most superpixel algorithms rely on low-level image evidence such as color, intensity, contour, and texture information. Many but not all of these algorithms produce superpixels with regular shape and size, that adhere to image contours and some additionally, roughly, *snap* to a regular grid pattern over the image. Image contour can be further separated into *internal* and *external* edges. By internal edges we mean contours that appear due to a marked difference in intensity, color, or texture between pixels that fall on the *same* object surface in the image, whereas external edges are those delineating locations where one object occludes another or of self occlusions. Many of the low-level algorithms produce superpixels that align to both types of contours. Indeed a single superpixel boundary can align with one or more internal and external edges. This is in contrast to the desired output from semantic segmentation algorithms where the segment boundaries should align to object-to-object or object-to-background boundaries.

As mentioned earlier it is common for semantic segmentation approaches to rely on superpixels, generated using low-level segmentation algorithms, as the basic primitives over which to construct larger segments. This isn't always the case however – in fact there are semantic segmentation methods [16, 17] that use complete or partially complete object *proposals* (*i.e.* segments) as their basic primitives, and these segments do tend to align better to external edges in the image. The figure-ground models used to generate the proposals are typically learned by maximizing an objectness score,

thereby generating segments that better correspond to objects of interest (i.e. *figure*) than to everything else (i.e. *background*).

As previously mentioned the segments that semantic segmentation methods generate can also span multiple connected components (in graph parlance). For example if object *A* is partially occluded by object *B* visually splitting *A* into two parts in the image, and the two objects are of different categories, then the correct segmentation component associated with object *A* is composed of two separate connected components. On the other hand if both *A* and *B* have the same object category then the correct semantic segmentation output would be a single component tightly covering *A* and *B*. Furthermore, if the task is *instance level* semantic segmentation, and *A* and *B* appear adjacent to each other in the image but are of the same category label, then the correct output should be two separate connected components each tightly covering one of the objects and each assigned a unique instance label.

For downstream computer vision tasks low-level image segmentation, and requisite superpixel output, provides a nice way to improve computational efficiency. Compared to working with pixels which number from tens of thousands to millions in typical images, superpixels tend to number in the dozens or hundreds. That's a few orders of magnitude reduction in the number of variables that need to be considered by a semantic segmentation algorithm. Since superpixels are the results of algorithms designed to align closely with significant image contours, they provide the added benefit of combining to produce segments that also align well to significant contours along their boundary. A third reason for using superpixels instead of pixels is that, in contrast, superpixels provide a boundary aligned spatial support on which to compute image features. The segment on which we should compute features for a pixel is less well defined, and usually local features [24, 76, 86] are computed on a spatial neighborhood around the pixel that is grid aligned. In conjunction, the fact that superpixels can span many pixels and cover a large pixel neighborhood, including neighbors that are more than one pixel apart, provides useful long-range dependencies between areas in the image. As we will elaborate on later in this chapter, these long-range dependencies allow short-range dependency (i.e. dependency between adjacent elements in a neighborhood) graph based semantic segmentation algorithms to incorporate implicit long-range information for local prediction of superpixel labels — producing segmentations that are more consistent with the image — at the same time bypassing the complexities involved with incorporating explicit long-range edges in the graph.

So far we have talked about a few different segmentation tasks: low-level, semantic, instance level, and figure-ground segmentation. This is by no means an exhaustive list of segmentation tasks. Some other common segmentation tasks that we'll mention here include interactive segmentation, cosegmentation, object-proposals, and holistic scene segmentation.

Interactive segmentation is an approach where the user is in the loop. In this task the goal is to have a system that, given an image, asks the user to input exemplars for the types of regions that the user would like the system to segment. The exemplars could be pixels, superpixels, or other regions, in the image and the user interacts with the system via scribbles [12], bounding boxes [93], or polygons, etc on the image indicating the regions corresponding to different categories they'd like to segment. Given the user *annotation* an initial segmentation of the image (be it a multi-category, figure-ground, or low-level segmentation) is produced by the system and offered to the user. Depending on the quality of the segmentation the user has the option to refine or provide more annotations as before and have the system refine the segmentation. This iterative process continues until the user is happy with the segmentation at which point the process terminates.

In cosegmentation [6, 94, 102] the task, usually, is to jointly segment different instances of the same object category that appear in a set of images. Alternately the images could contain the same object instance under different views or deformations. If the task is to segment frames in video sequences this approach to segmentation has clear advantages because it leverages more information in learning the segmentation model for object categories and instances.

A major advance in semantic segmentation came with the use of object proposals [16, 27]. The idea here is to produce multiple object proposals for the image. Each object proposal is either a figure-ground segment or bounding box in the image, and the proposals are allowed to overlap. The semantic segmentation task shifts from labeling pixels/superpixels in the image to selecting a subset of the top ranking object proposals and assigning them semantic labels. Using object proposals makes the problem much simpler because the set of object proposals is much smaller than the number of pixels/superpixels in the image. Object proposals also provide much larger spatial support for computing features useful in determining objectness likelihood of the underlying image region. It's also more likely that one of the object proposals is a good candidate segment for an object. The object proposals are usually generated using class-independent methods. For example the object proposals can be bottom-up segmentations computed over the image which are ranked according to an *objectness* score that takes into account cues like color, texture, location, saliency, etc [27]. Alternatively, a bottom-up approach can be taken to produce multiple figure-ground masks using a graph-based model initialized with different random seeds [16]. The masks are then ranked according to class specific regressors trained to maximize the likelihood that the mask tightly covers the underlying object of that category. One of the most successful approaches for building object proposals that is very fast and gives high recall on objects present in the image is Selective Search [100]. Here multiple hierarchical segmentations over superpixels are computed. The object proposals consist of either segments within this hierarchy or bounding boxes around them.

Finally, there are approaches [128] that try to reason about multiple tasks over the image in order to come up with a *holistic* interpretation of what is being depicted. The task, then, becomes to jointly reason about both the segmentation of the image into semantically meaningful segments while simultaneously predicting the scene classification and detecting what objects are in the image along with their locations and extents. Allowing for joint prediction of multiple tasks has the added benefit of incorporating multiple compatibility measures. Each of these compatibility features is an added source of rich information that the model can use in order to improve the segmentation accuracy.

In the next section we'll dive a little deeper into some of the most popular bottom-up and top-down segmentation methods and explain in more detail how they work. We'll also describe the specific segmentation models we used in the experiments of subsequent chapters.

1.1.1 Methods

Segmentation has a long and rich history and we will not try to enumerate all the different segmentation methods. Instead we'll highlight a few of the most popular methods for both low-level and semantic segmentation.

One class of segmentation methods is based on algorithms that try to find the maxima, or modes, of a data distribution given a discrete set of points. They are clustering methods because they assign all points within a *basin of attraction* of a mode to the same cluster. Another nice property is that these methods are non-parametric. That means that the space of data points can be viewed as the empirical probability density function of the parameter the data points represent. The modes of the density function will correspond to dense regions, or clusters, in the data space. That's why these methods are also referred to as hill-climbing or gradient based methods because they find the maxima of the data distribution. This is nice because we don't need to know a priori the number and shape of the clusters.

1.1.1.1 Mean Shift

One of the most popular such methods is based on the mean shift algorithm [23].

In the mean shift algorithm the unknown data density is estimated using the kernel density estimator,

$$\hat{f}(\mathbf{x}) = \frac{1}{nh^d} \sum_{i=1}^n K\left(\frac{\mathbf{x} - \mathbf{x}_i}{h}\right), \quad (1.1)$$

where \mathbf{x} , \mathbf{x}_i are d -dimensional data points, and K here is assumed to be a multivariate normal kernel with diagonal bandwidth matrix $h^2\mathbf{I}$ for simplicity (h is the bandwidth parameter), though any radially symmetric kernel that satisfies some mild assumptions would suffice. The modes of the density are locations where $\hat{\nabla}f(\mathbf{x}) = 0$. The density gradient when assuming normal kernel K is,

$$\hat{\nabla}f(\mathbf{x}) = \frac{1}{nh^d} \sum_{i=1}^n K\left(\frac{\mathbf{x}-\mathbf{x}_i}{h}\right) \left(\frac{\sum_{i=1}^n \mathbf{x}_i K\left(\frac{\mathbf{x}-\mathbf{x}_i}{h}\right)}{\sum_{i=1}^n K\left(\frac{\mathbf{x}-\mathbf{x}_i}{h}\right)} - \mathbf{x} \right). \quad (1.2)$$

The second term is the mean shift,

$$m(\mathbf{x}) = \frac{\sum_{i=1}^n \mathbf{x}_i K\left(\frac{\mathbf{x}-\mathbf{x}_i}{h}\right)}{\sum_{i=1}^n K\left(\frac{\mathbf{x}-\mathbf{x}_i}{h}\right)} - \mathbf{x}, \quad (1.3)$$

which is the difference between the weighted average of the points and \mathbf{x} . It can be shown [20, 23, 35] that the mean shift is proportional to,

$$m(\mathbf{x}) \propto \frac{\hat{\nabla}f(\mathbf{x})}{\hat{f}(\mathbf{x})}, \quad (1.4)$$

or in other words the mean shift points along the direction of steepest ascent of the empirical density at point \mathbf{x} . This is a nice property because it provides a natural algorithm for mode finding:

- Start at a data point \mathbf{x} ,
- Repeat the following steps till convergence (i.e. $m(\mathbf{x}) \approx 0$):
 - Compute the mean shift vector $m(\mathbf{x})$ (1.3),
 - Update the location of the kernel window using $m(\mathbf{x})$,

The fact that the mean shift is normalized by the density makes the mean shift algorithm an adaptive gradient ascent algorithm that takes large steps in areas of low density and takes increasingly smaller steps as it approaches high density areas where the modes are.

All points that converge to the same stationary point are within the *basin of attraction* of a mode. These points can all be considered as one cluster and assigned the same cluster label.

The mean shift algorithm has been applied to the task of image segmentation [23] where, normally, the \mathbf{x}_i — $i = 1, \dots, n$, where n is the number of pixels in an image — are d -dimensional feature vectors containing the pixel location and LAB (or LUV) color or intensity information. Typically d is small because mean shift suffers from the *curse of dimensionality*. A higher dimensional space will be sparsely populated with data points and the density concentrated in a very small part of the space making the

kernel density estimator a poor estimate of the true density. Another issue with mean shift is that the feature space is assumed to be a Euclidean space, or some other space where an inner product or Riemannian metric is defined, which might not generally hold. The mean shift algorithm is also pretty slow with $\mathcal{O}(n^2)$ running time.

1.1.1.2 Quick Shift

An alternative, simpler, strategy for mode seeking is quick shift [116]. Whereas in mean shift we had an iterative algorithm and had to compute the gradient, in quick shift we only need to take one step for each data point and no gradients are needed. In quick shift each data point is moved to the location of a neighboring point that increases the probability density. We can write the probability density estimate at \mathbf{x}_j as,

$$\hat{f}(\mathbf{x}_j) = \frac{c}{n} \sum_{l=1}^n k(d(\mathbf{x}_l, \mathbf{x}_j)), \quad (1.5)$$

where k is some radially symmetric kernel function, $d(\mathbf{x}_i, \mathbf{x}_j)$ is a metric on \mathbf{x} , and c is a normalization constant. For data point \mathbf{x}_i we assign it the data point \mathbf{y}_i such that,

$$\mathbf{y}_i \leftarrow \underset{j: \hat{f}(\mathbf{x}_j) > \hat{f}(\mathbf{x}_i)}{\operatorname{argmin}} d(\mathbf{x}_i, \mathbf{x}_j), \quad (1.6)$$

guaranteeing that we move up the hill toward a mode. Doing this procedure for every point \mathbf{x}_i connects all the points into a tree, with edge weights set to $d(\mathbf{x}_i, \mathbf{x}_j)$. Cutting edges with weight larger than some threshold t breaks the tree into subtrees that cluster the points with the root nodes as possible modes of the empirical distribution. Adjusting the threshold controls how much fragmentation of the modes there is which affects the number of segments you get. The method is still rather slow with $\mathcal{O}(dn^2)$ complexity, where d is a small constant.

1.1.1.3 Watershed Transform

Another approach to segmentation is based on the watershed transform. There are a number of different watershed transforms, such as watershed by immersion or by topographical distance [91]. The basic idea is simple though, you can view an intensity or grey level image as a landscape with *catchment basins* or wells in the topography and *watersheds* where multiple basins meet. The general approach is to start off by assigning local minima in the intensity or grey level image to distinct basins. In the watershed by immersion approach (cf. [91]) the basins are recursively grown by iteratively increasing the level set and assigning unlabeled pixels that have intensity value no greater than the level set value to the catchment basin that is closest. If the pixel is equidistant to two or more catchment basins then it is not assigned to any basin and is reconsidered in the next iteration. The process continues until all level sets (*i.e.* image intensity values)

have been considered, at which point all unlabeled pixels are assigned as watershed (*i.e.* boundary). The basins are the resultant segmentation of the image.

The watershed transform by topographical distance approach (cf. [91]) assumes a cost between neighboring pixels p and q that takes into account the slope between p and q . The topographical distance along a path is defined as the sum of costs between neighboring pixels along the path. The topographical distance between two points is then just the minimum topographical distance of any path connecting them. A catchment basin around a local minimum is then defined as all the pixels that are closer to that minimum in terms of topographical distance than to any other local minimum in the image. The watershed boundaries are the set difference of the image with the pixels in all the catchment basins.

1.1.1.4 Graph Based - Normalized Cuts

There are also graph based approaches for low-level segmentation that let each pixel be a node in a graph, with some edge connectivity between pixels, and partition the graph to produce a segmentation of disjoint components. Of these there is a subtype of algorithms that are based on spectral partitioning of the graph — normalized cuts being one such method. In the normalized cuts algorithm [104] we assume a graph $G = (V, E)$ where each vertex in V is associated with unique pixel in the image (vertices in V cover the image) and E contains edges between all pairs of pixels. For each edge $(v_i, v_j) \in E$ we assign a weight w_{ij} capturing how likely it is that v_i and v_j belong to the same object in the image. Usually w_{ij} is a similarity measure between feature vectors computed at i and j . A *cut* of G given two disjoint components C_1 and C_2 is defined as,

$$cut(C_1, C_2) = \sum_{i \in C_1, j \in C_2} w_{ij}. \quad (1.7)$$

The minimum cut of G , *i.e.* the subset of E that minimizes the total edge weight crossing the cut, is the optimal partition of the image into two components. Using the total edge weight crossing the cut is not ideal for segmentation because it tends to favor partitioning small components since the cut value grows as the number of edges across the bipartition grows. To account for this in normalized cuts they use the *normalized cut* (cf.[104]),

$$ncut(C_1, C_2) = \frac{cut(C_1, C_2)}{assoc(C_1, V)} + \frac{cut(C_1, C_2)}{assoc(C_2, V)}, \quad (1.8)$$

where $assoc(C_i, V) = \sum_{i \in C_i, j \in V} w_{ij}$ is the total weight of edges from pixels in C_i to all pixels in the graph. If C_1 is small, $assoc(C_1, V)$ will tend to also be small, increasing the cut value, $ncut(C_1, C_2)$. Consequently it prevents cuts that favor producing small components.

It turns out that computing a bipartition of the graph into C_1 and C_2 that minimizes 1.8 amounts to solving the following generalized eigenvalue problem

$$(\mathbf{D} - \mathbf{W})\mathbf{y} = \lambda\mathbf{D}\mathbf{y}, \quad (1.9)$$

where \mathbf{D} is an $n \times n$ diagonal matrix with $\mathbf{D}_{ii} = \sum_j w_{ij}$ along the diagonal, and \mathbf{W} is an $n \times n$ symmetric matrix with $\mathbf{W}_{ij} = w_{ij}$. It can be shown [104] that the eigenvector \mathbf{y} corresponding to the second smallest eigenvalue of 1.9 gives the assignment that partitions G into components C_1 and C_2 that minimize the normalized cut. The eigenvector \mathbf{y} ideally will have two discrete points $+1, -1$ indicating whether or not a pixel i is assigned to component C_1 . But in order to solve 1.9, \mathbf{y} is relaxed to take on real values. Therefore the final assignment can be done by either using 0 as the threshold on the values of \mathbf{y} — where all elements with value > 0 are assigned to C_1 and C_2 otherwise — or we can search over different thresholds and pick the partitioning that minimizes the *ncut*.

This leads to a simple normalized cut algorithm for segmenting the graph called *two-way ncut* [104],

- Construct a fully connected graph $G = (V, E)$ over pixels in the image, with edge weights w_{ij} measuring similarity between pairs of pixels.
- Solve the generalized eigenvalue problem $(\mathbf{D} - \mathbf{W})\mathbf{y} = \lambda\mathbf{D}\mathbf{y}$ for eigenvectors with smallest eigenvalues.
- Bipartition the graph using the eigenvector corresponding to the second largest eigenvalue. If \mathbf{y} contains more than two discrete values, search for the splitting point that gives the minimum *ncut* value.
- For each component created after the bipartition we can decide whether to recursively apply the same procedure again to partition the component into two separate components based on the *ncut* value.
- Stop partitioning when the *ncut* value is below a certain threshold.

The resulting segmentations have some nice properties. Because the cut is over a fully connected graph the solutions take global image information in producing the segmentation. The components in the segmentation also need not be connected components in the graph — a component can consist of pixels found in multiple disjoint regions in the image. The normalized cut algorithm is relatively slow with a running time complexity of $\mathcal{O}(n^{3/2})$, where n is the number of pixels in the image.

Results of the normalized cuts algorithm are shown in figure 1.1. These are based on the alternate *k-way* cut algorithm (cf. [104]) that produces a simultaneous segmentation into k regions. In the *k-way* cut approach they associate an n -dimensional vector with each pixel in the image by stacking the top n eigenvectors. An over-segmentation of

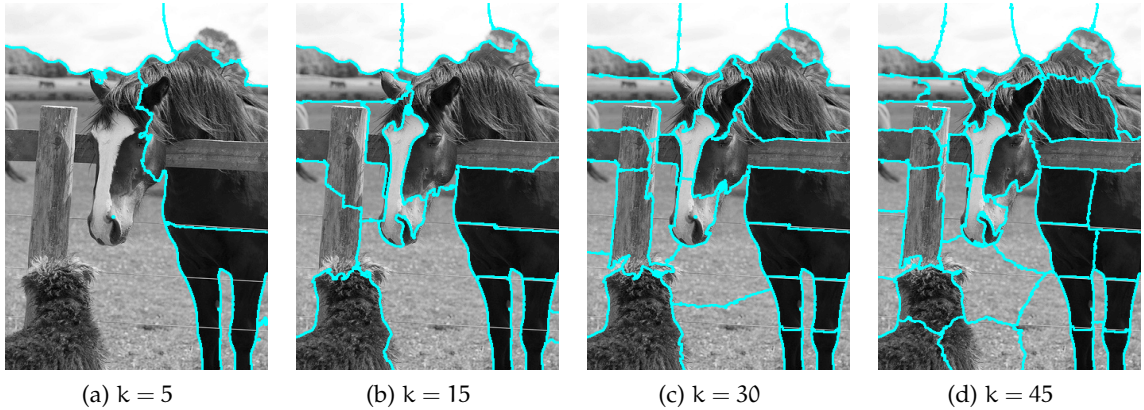


Figure 1.1: Bottom-up segmentation using normalized k -way cut algorithm as a function of the number of segments (top eigenvectors), k . Note that a segment can consist of multiple disconnected components (e.g. segment on nose of horse).

$p \geq k$ segments is produced by clustering the n -dimensional vectors using k -means. Next, either a greedy merging strategy can be used or a global recursive cut is performed. In the greedy merging approach regions are merged iteratively until k segments are left. In each iteration the two regions that minimize the following k -way normalized cut are merged,

$$\text{Ncut}_k = \frac{\text{cut}(A_1, V - A_1)}{\text{assoc}(A_1, V)} + \frac{\text{cut}(A_2, V - A_2)}{\text{assoc}(A_2, V)} + \dots + \frac{\text{cut}(A_k, V - A_k)}{\text{assoc}(A_k, V)} \quad (1.10)$$

where the A_i 's are the segments. Alternatively, a new graph can be constructed with the A_i 's as nodes and edge weights, w_{ij} , corresponding to $\text{assoc}(A_i, A_j)$, capturing the total weight between pixels in A_i and A_j . Recursively bipartitioning this new graph — by either solving the eigensystem defined earlier for the ncut criterion or exhaustively minimizing the ncut criterion when k is small results in the final k -way partition. For further details of the approach, refer to Shi and Malik [104].

1.1.1.5 Graph Based - Felzenswalb & Huttenlocher

A similar approach to the normalized cuts method is that of Felzenswalb and Huttenlocher [30]. Here again they assume a graph $G = (V, E)$ where for every pixel p_i in the image there is a corresponding node v_i in V . The edge set E is assumed to be locally connected however, where the local neighborhood could be 4 or 8-connected neighborhood of a pixel or any other local neighborhood connectivity. For each edge (v_i, v_j) there is an associated weight w_{ij} , similar to normalized cuts, that measures the dissimilarity between p_i and p_j . For example for an intensity image I we could define $w_{ij} = |I_{p_i} - I_{p_j}|$.

To determine whether two components should be connected they define a boundary predicate,

$$D(C_1, C_2) = \begin{cases} \text{true} & \text{if } Dif(C_1, C_2) > MInt(C_1) \\ \text{false} & \text{otherwise} \end{cases} \quad (1.11)$$

where $Dif(C_1, C_2)$ is defined as,

$$Dif(C_1, C_2) = \min_{v_i \in C_1, v_j \in C_2} w_{ij} \quad (1.12)$$

and $MInt(C_1, C_2)$ as,

$$MInt(C_1, C_2) = \min(Int(C_1) + \tau(C_1), Int(C_2) + \tau(C_2)), \quad (1.13)$$

where $Int(C)$ is the value of the maximum weight edge in the minimum spanning tree of component C in graph G . Intuitively $Dif(C_1, C_2)$ captures the difference between two connected components. For two connected components that don't have a connecting edge the value is set to ∞ . The value $MInt(C_1, C_2)$ captures the minimum internal difference of either C_1 or C_2 . When the difference between two components is larger than the minimum difference in at least one component then we want a boundary between the two components (*i.e.* $D(C_1, C_2) = \text{true}$), hence the inequality in eqn. 1.11. The threshold $\tau(C)$ controls how much larger the inter-component difference needs to be relative to the intra-component difference in order to have a boundary, and they set it to,

$$\tau(C) = \frac{k}{|C|} \quad (1.14)$$

for some constance k , where $|C|$ is the size of C . Increasing k results in larger components.

The Felzenswalb and Huttenlocher algorithm [30] for partitioning the graph using the predicate is straight forward:

1. Order the m edges in E according to decreasing edge weights w_{ij} .
2. Set each node $v_i \in V$ as a distinct component in the initial segmentation, S_0 .
3. Repeat the following from $k = 1, \dots, m$:
 - For edge $e_k = (v_i, v_j)$ in the ordering if v_i and v_j are in separate components of S_{k-1} and if $w_{ij} < MInt(C_i^{k-1}, C_j^{k-1})$ then merge C_i^{k-1} and C_j^{k-1} into a single component in S_k . Otherwise $S_k = S_{k-1}$.

This simple algorithm can be applied to different neighborhood relations between vertices in the graph — for example 8-pixel neighborhoods on grid graphs over the image, or nearest neighbor graphs over feature space. In the nearest neighbor graph edges

connect vertices that are neighbors in feature space, with weights equal to the distance between features. The neighborhood can be all vertices falling within a euclidean ball or simply a fixed number of nearest neighbors returned by an approximate nearest neighbor method. In either the grid or nearest neighbor graphs, using approximate nearest neighbor methods, the running time is shown to be $\mathcal{O}(n \log n)$. The results when partitioning in feature space using the nearest neighbor graph tend to contain higher level information because they capture more global image information. The resulting segmentations tend to align well with image boundaries.

Ratio cut [120] is another well known such method.

1.1.1.6 SLIC

Arguably one of the best low-level segmentation algorithms that produces compact superpixels with very good boundary adherence is *Simple Linear Iterative Clustering* (SLIC) [1]. It is remarkably simple, and one of the fastest algorithms with a linear runtime complexity in the number of pixels, $\mathcal{O}(n)$. It is also the superpixel algorithm we chose for a number of our experiments in chapters 4 and 5. SLIC relies on a k-means approach to clustering that assigns pixels with similar color features and spatial locations to the same cluster. The standard k-means approach of considering all pixels in the image when finding nearest neighbors of a pixel is prohibitively slow so in SLIC a different approach is taken. Initially a set of cluster centers, c_i , are assigned along a regular spatial grid over the entire image, corresponding to the centers of the superpixels. The cluster centers are usually 5-dimensional vectors containing the color intensity and spatial location. They are initialized with the pixel color and location falling under the grid locations. The grid spacing, $S = \sqrt{n/k}$ is proportional to the number of superpixels, k , that the user would like to have in the image. These initial centers are first adjusted to the lowest gradient locations within a 3×3 neighborhood of their initial locations so that they don't fall on boundaries or noisy pixel locations. The next step in the algorithm is to assign pixels to cluster centers, which means computing the feature distance between each c_i and the pixels that are within a spatial neighborhood. Limiting the search space to pixels within a local neighborhood of a cluster center is why this algorithm is so fast. Since the desired superpixel size is $S \times S$, the SLIC algorithm searches within a $2S \times 2S$ neighborhood of c_i . To each pixel the algorithm assigns the label of the cluster c_i that is closest to it in feature space. There are no more than eight possible cluster labels for a pixel to be assigned due to the limited search region during assignment. Once each pixel is assigned a cluster center the cluster centers are updated. The process is repeated until the residual error between the current and previous iteration cluster centers reduces below some threshold. Algorithm 1 is the same as that found in the SLIC paper [1]. A critical component of why SLIC superpixels tend to be compact is the distance function D that it employs.

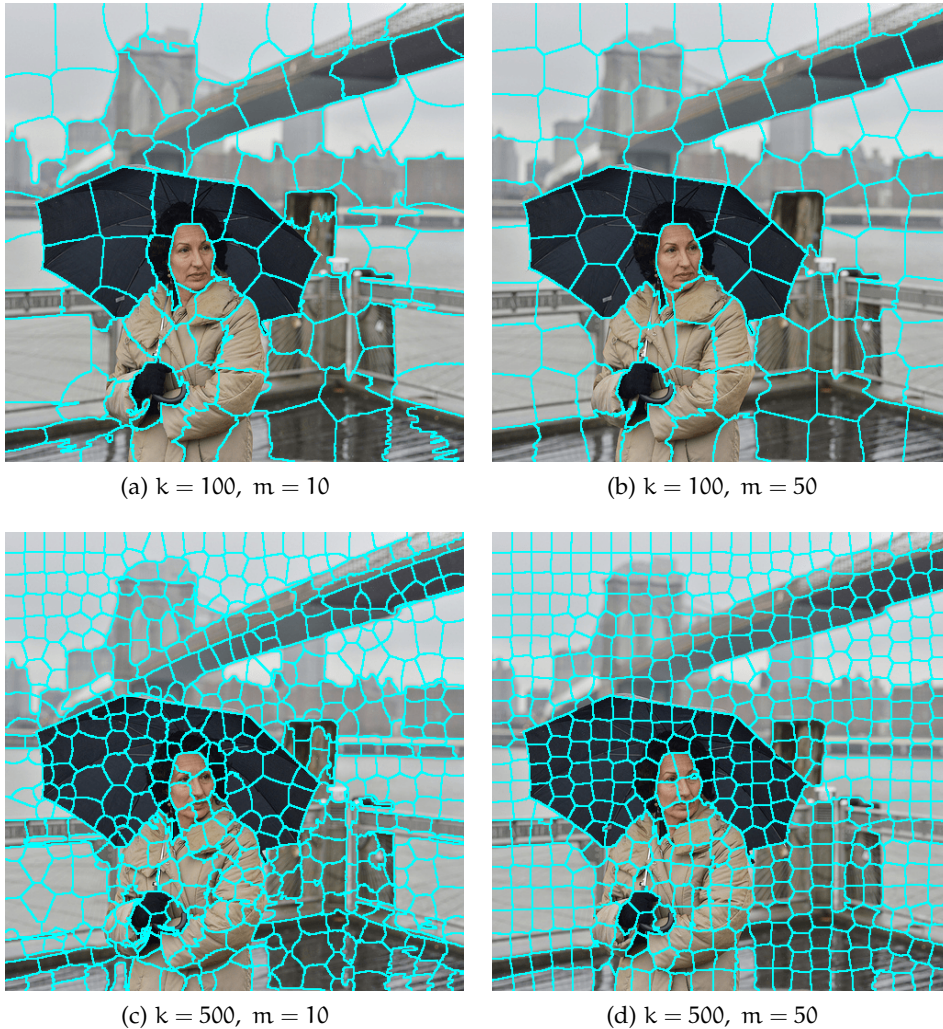


Figure 1.2: SLIC superpixel results as a function of the desired number, k , and compactness, m . As m is increased the superpixels exhibit more regular appearance, aligning less with image contours and more with spatial grid.

In order to balance between spatial compactness and color consistency of a superpixel, in SLIC they devise the following distance,

$$D = \sqrt{d_c^2 + \left(\frac{d_s}{S}\right)^2 m^2}, \quad (1.15)$$

where d_c and d_s are the Euclidean color and spatial distances between two points respectively, and constant m controls the relative importance of color similarity versus spatial compactness of the superpixels. Normalizing d_s by S above balances the spatial distance relative to color, which is important, otherwise compact superpixels would be favored by the distance measure. Other distance functions such as geodesic distance can also be considered. One issue that needs to be handled at the end of running

Algorithm 1 SLIC superpixel segmentation [1]

```

1: Initialize cluster centers  $c_i$  by sampling pixels at regular grid interval  $S$ .
2: Move cluster centers to lowest gradient location within  $3 \times 3$  neighborhood.
3: label  $l(p) \leftarrow -1$  for each pixel  $p$ .
4: distance  $d(p) \leftarrow \infty$  for each pixel  $p$ .
5: repeat ▷ Assignment
6:   for each cluster center  $c_i$  do
7:     for each pixel  $p$  in  $2S \times 2S$  neighborhood around  $c_i$  do
8:       Compute distance  $D$  between  $c_i$  and  $p$ .
9:       if  $D < d(p)$  then
10:         $l(p) \leftarrow i$ 
11:         $d(p) \leftarrow D$ 
12:       end if
13:     end for
14:   end for
15:   update cluster centers using assignments  $l(p)$ . ▷ Update
16:   compute residual error  $E$  between current and previous cluster centers.
17: until  $E \leq \text{threshold}$  ▷ Post-Process
18: enforce connectivity of superpixels by assigning orphaned pixels to nearest super-
    pixels.
```

algorithm 1 is that some pixels are orphaned from the superpixel they belong to. A post-processing step is done to reassign pixels to nearby superpixels so that they have a connected structure.

1.1.1.7 Object Proposals - CPMC

Another class of segmentation algorithms is based on producing a large set of region proposals that would provide good overlap with foreground objects. Object proposals have the benefit of providing a larger image support for tasks where we want to do category detection or semantic segmentation. Compared to the space of possible solutions over pixel/superpixels the set of proposals provides orders of magnitude fewer candidates and more efficient search. Given that the vast majority of possible solutions over pixels or superpixels do not conform to general appearances of objects in images — such as spatial connectivity — considering a much smaller subset of proposals that adhere to image cues like boundary, and color and spatial uniformity, is appealing. One popular region proposal approach is *constrained parametric min-cut* (CPMC) [16]. In CPMC a set of initial candidate figure-ground proposals are generated very efficiently which are subsequently pruned and ranked according to how likely the

proposals are to tightly cover a foreground object. The top ranking proposals can be retained for a higher level recognition task.

The initial set of proposal in CPMC is constructed by solving multiple parametric min-cut [16] problems on a submodular grid graph over the image, with multiple different initializations. Given a graph $G = (V, E)$ over pixels where adjacent pixels in a 4-neighborhood share edges, a figure-ground segmentation is performed by minimizing the following objective,

$$E(X, \lambda) = \sum_{i \in V} D(x_i, \lambda) + \sum_{(i,j) \in E} V_{ij}(x_i, x_j), \quad (1.16)$$

where the data term is defined to be,

$$D(x_i, \lambda) = \begin{cases} 0 & \text{if } x_i = 1, i \notin \mathcal{V}_b \\ \infty & \text{if } x_i = 1, i \in \mathcal{V}_b \\ \infty & \text{if } x_i = 0, i \in \mathcal{V}_f \\ f(x_i) + \lambda & \text{if } x_i = 0, i \notin \mathcal{V}_f \end{cases} \quad (1.17)$$

where \mathcal{V}_f and \mathcal{V}_b are the pixels in a seed region for the foreground and background respectively. The foreground seed regions are groupings of pixels forming small squares a few pixels wide, sampled regularly along a grid over the image, and the background seed regions are horizontal or vertical edges of the image. The pixel labeling takes on either foreground ($x_i = 1$) or background ($x_i = 0$). The cost of assigning pixels not in the foreground seed region to background is set by $f(x_i) + \lambda$. The first term is either uniformly set to 0 or is the log ratio of probabilities of pixel i belonging to foreground versus background, where the probability of foreground is,

$$p_f(i) = e^{-\gamma \min_j (||I(i) - I(j)||)}, \quad (1.18)$$

where j is over pixels in the seed region — and similarly for the background probability. The parameter λ is a foreground bias that can be adjusted, where for each setting a different solution is computed.

The pairwise term in eqn. 1.16 penalizes adjacent pixels that cross an image boundary,

$$V_{ij}(x_i, x_j) = \begin{cases} 0 & \text{if } x_i = x_j \\ e^{-\frac{\max(gPb(i), gPb(j))}{\sigma^2}} & \text{if } x_i \neq x_j \end{cases}, \quad (1.19)$$

where $gPb(i)$ is the contour strength at pixel i computed using globalPb [3]. Using a parametric min-cut solver minimization of eqn. 1.16 can be done for all setting of λ in the same time complexity as doing a single min-cut. The complexity of computing the initial set of regions using k different combinations of foreground/background seeds and choice of $f(x_i)$ is $\mathcal{O}(kmn \log n)$, where m is the number of edges and n is the number of pixels. Successively increasing values of λ given the same seeds and $f(x_i)$ results in nested regions that progressively get larger.

Given this initial bag of figure-ground proposal regions pruning is done by throwing away very small regions and sorting the remaining segments using ratio cut [120] value. The top sorted 2000 proposals are kept.

Ranking of the proposals is done by training a regressor (random forest) that takes region, Gestalt, and graph partition features over the proposal (details in [16]) to regress onto the intersection-over-union score of the proposal with the best overlapping ground-truth region. The objective is to retain the minimal set of ranked region proposals that maximize a covering of the ground-truth regions, and discard the rest. To do this CMPC uses the following covering score,

$$C(G, S(r)) = \frac{1}{n} \sum_{g \in G} |g| \max_{s \in S(r)} O(g, s), \quad (1.20)$$

where G and $S(r)$ are the ground-truth segments and region proposals with rank higher than r respectively, $|g|$ is the number of pixels in the ground-truth segment and $O(g, s)$ is the intersection-over-union score between ground-truth and region proposal segments. As the authors of CPMC note, many of the segments are similar in shape size and location. Similar segments end up having similar features which mean the regressor ranks them to similar scores, so the sorted list of region proposals will have many cases where sequentially ranked segments have the same quality of coverage for a ground-truth segment. Using the covering measure in eqn. 1.20 to pick a cut-off rank r would result in a bag of segments with many redundant ones. To alleviate this they propose to diversify the final bag using the *Maximal Marginal Relevance* (MMR) measure [14],

$$MMR = \operatorname{argmax}_{s_i \in S \setminus S_k} \theta \cdot \operatorname{score}(s_i) - (1 - \theta) \cdot \max_{s_j \in S_k} o(s_i, s_j), \quad (1.21)$$

where S is the set of all proposals, S_k is the set of selected proposals in round k , $\operatorname{score}(s_i)$ is the regressor score for proposal s_i , and $o(s_i, s_j)$ is the overlap between the two proposal. The *MMR* measure is applied in an iterative fashion. Starting with the highest scoring proposal which is placed in S_1 , the next proposal, s_i , picked is one that has the best trade-off in maximizing the regressor score at the same time minimizing its overlap with any of the previously picked proposals. This selection procedure can continue until the covering score using the current set of region proposals reaches some threshold.

This method produces very good quality region proposals and, at the time of our experiments in later chapters, was a state of the art region proposal method. It shows up as the underlying region-proposal method for the semantic segmentation model O_2P [17] which we use in Chapters 2 & 3.

1.1.1.8 Object Proposals - continued

There are a number of other noteworthy object proposal methods which we'll briefly outline here.

Endres and Hoiem [27, 28] introduced a region proposal method that generates an initial bag of region proposals and ranks them to produce a set of diverse region proposals that maximally cover foreground objects in the image. The initial set of region proposals is generated using the occlusion boundary algorithm [45] which constructs a hierarchical segmentation of the image.

This hierarchical segmentation algorithm uses cues on both regions, boundaries, and 3D surface and 3D depth to predict occlusion boundary probability (*i.e.* boundaries between different objects) as well as figure-ground probability at each pixel. After predicting the occlusion boundary probabilities, agglomerative clustering by iteratively merging regions with minimum boundary strength up to a threshold produces the hierarchical segmentation.

Given the segmentation hierarchy, initial seeds are picked from the hierarchy as starting points from which to construct object proposals. These seed regions are used to label superpixels as either belonging to the object or background depending on their affinity with the seed region (*i.e.* likelihood of belonging to the same foreground object as the seed). This problem is formulated as a CRF over superpixels consisting of two terms, an affinity measure between superpixels and the seed region, and an edge cost for two adjacent superpixels to take on a different label (*i.e.* foreground/background), which is proportional to the probability of the occlusion boundary between the two superpixels. The region affinity term uses features such as layout prediction of the seed and superpixel on the object (e.g. right+left of object) to capture their layout agreement, and their layout location (e.g. center, top, bottom, etc) on the object. Maximizing the CRF energy infers a labeling over the superpixels indicating which of them are part of the same foreground region as the seed.

Having generated a set of candidate proposals by considering multiple seed regions their method ranks the proposals so that higher ranked proposals will be more likely to tightly cover a foreground region while at the same time have minimal overlap with any higher ranked proposal. Given a ranking \mathbf{r} over a set of proposals \mathbf{x} they define the following score,

$$S(\mathbf{x}, \mathbf{r}; \mathbf{w}) = \sum_i \alpha(r_i) \cdot (\mathbf{w}_a^T \boldsymbol{\psi}(x_i) - \mathbf{w}_p^T \boldsymbol{\phi}(r_i)), \quad (1.22)$$

where $\boldsymbol{\psi}(x)$ are appearance features and $\boldsymbol{\phi}(r)$ is an overlap penalty incurring a cost for a proposal to overlap with the set of higher ranked proposals. The monotonically decreasing function of rank, $\alpha(r_i)$, encourages high ranked proposals to have higher score. The appearance features capture how likely the proposal is to be an object re-

gion. Therefore they use occluding boundary probabilities, interior and exterior boundary probabilities, likelihood of region being background from a background predictor, and statistical differences in color and texture between the region and the surrounding area to capture the appearance. It's not possible to maximize eqn. 1.22 with respect to r exactly so a greedy maximization strategy that incrementally selects proposals based on which one maximizes the marginal gain. To optimize over w a latent max-margin structure learning approach is used that minimizes the score of the highest scoring incorrect ranking order while simultaneously maximizing the score of correct ranking. They use a margin that encourages the best region proposals for each object to have the highest rank. More details can be found in [27, 28].

The resulting region proposals from this method are competitive with CPMC. The CPMC region proposals tend to be a bit less diverse and as the overlap threshold for removing redundant regions is lowered the recall of object regions is worse than Endres and Hoiem's method [27, 28].

1.1.1.9 ALE and the Associative Hierarchical CRF

A prime example of an object segmentation method that can achieve accurate segmentation results by solving an inference problem on a Conditional Random Field (CRF) over the image is the *Automatic Labelling Environment* [67]. It is a segmentation system that is the culmination of a number of papers by Ladicky et al [56, 59, 68, 69, 71, 72, 98, 110]. The underlying model is a hierarchical CRF on pixels, segments, and super segments over the image.

A main contribution of this segmentation model is the observation that the image quantization level that one chooses is critical in producing good segmentations. It is a common observation that inference on CRFs defined over random variables corresponding to pixels in the image often produce segmentations that do not align well with object boundaries. Conversely, the assumption that superpixels from bottom-up algorithms align well with object boundaries is often wrong. That is why CRFs over superpixels often yield segmentations that also do not align well with boundaries. Superpixels do offer advantages though — they provide both larger and specific spatial support (context) to compute features and as primitives they allow for more efficient inference over graphical models. Also, the assumption that all pixels falling within the same superpixel should take on the same label, though often incorrect, is nevertheless a strong prior that often holds true. So the natural question is, what is the right level of image quantization? The answer seems to be that it depends on image and the objects in it. The major technical contribution of ALE, the *associative hierarchical CRF* [68], tries to tackle this issue by considering multiple quantizations. The structure is a three-level hierarchical CRF (the model and algorithm have no constraint on the number of levels), where the bottom-most level consist of random variables over pixels in the image. At the pixel level the random field consists of a grid graph over pixels in the image with

a 4-pixel neighborhood for each pixel. The next level up consists of random variables over segments. Each segment's node has an edge (conditional dependence) between it and the pixels that fall under it in the image. Edges connect adjacent segments in the image. The top-most layer consists of random variables corresponding to super-segments that are composed of the segments. Once again, the super-segment nodes share an edge to the segment nodes beneath if the segment is contained by the super-segment. Super-segments share edges if they are adjacent to each other in the image. The initial (super)segmentations used at the different levels in the CRF hierarchy are produced by running the bottom-up mean shift segmentation algorithm with varying bandwidth parameters for the color and spatial channels to produce progressively coarser superpixels.

To summarize the model we can write the energy of the hierarchical model as presented in [68],

$$E^{(0)} = \sum_{i \in \mathcal{S}^{(0)}} \psi_i(x_i^{(0)}) + \sum_{ij \in \mathcal{N}^{(0)}} \psi_{ij}(x_i^{(0)}, x_j^{(0)}) + \min_{\mathbf{x}^{(1)}} E^{(1)}(\mathbf{x}^{(0)}, \mathbf{x}^{(1)}), \quad (1.23)$$

where $\mathbf{x} = \{x^{(0)}, \dots, x^{(k)}\}$ is the vector of random variables, called the labeling, taking on values from the label set \mathcal{L}^n . The term $\psi_i(x_i^{(0)})$ is the pixel-wise unary potential, and $\psi_{ij}(x_i^{(0)}, x_j^{(0)})$ is the pixel-wise label consistency term between neighboring pixels, $\mathcal{S}^{(k)}$ is the set of pixels or segments, and $\mathcal{N}^{(k)}$ is the set of neighbors of a pixel or segment at level k . The last term in eqn. 1.23 can be recursively written as,

$$E^{(k)}(\mathbf{x}^{(k-1)}, \mathbf{x}^{(k)}) = \sum_{c \in \mathcal{S}^k} \psi_c^p(x_c^{(k-1)}, x_c^{(k)}) + \sum_{cd \in \mathcal{N}^{(k)}} \psi_{cd}(x_c^{(k)}, x_d^{(k)}) + \min_{\mathbf{x}^{(k+1)}} E^{(k+1)}(\mathbf{x}^{(k)}, \mathbf{x}^{(k+1)}). \quad (1.24)$$

The unary pixel-wise potentials are based on classifiers trained on color, shape and texture features (*i.e.* textons of *TextonBoost* [106]), *histograms of oriented gradients* (HOG [24]), and pixel location. The classifiers are applied at each pixel to estimate the probability of the pixel to take on a particular label. The pairwise pixel terms are *contrast sensitive potentials* [12] that encourage neighboring pixels to take on the same label,

$$\psi_{ij}(x_i, x_j) = \begin{cases} 0 & \text{if } x_i = x_j \\ g(i, j) & \text{otherwise} \end{cases} \quad (1.25)$$

where $g(i, j) = |c|^{\theta_\alpha} (\theta_p + \theta_v \exp(-\theta_\beta \|f_i - f_j\|^2))$ [12, 60], where I_i and I_j are the color vectors at pixels i and j , and θ_p , θ_v , and θ_B are learned parameters.

The higher order potentials $\psi_c^p(x_c^{(k-1)}, x_c^{(k)})$ are robust P^n potentials [60] that are equivalent to minimizing a pairwise graph over x_c . Here $x_c^{(k)}$ is the random variable associate with a segment, or super-segment, c at level k in the hierarchy. The variable c also stands for the *clique* consisting of variables (*i.e.* segments or pixels) at level

$k - 1$ that fall within the (super)segment c at level k . Therefore, $\mathbf{x}_c^{(k-1)}$ are the random variables associated with the clique, c , of pixels or segments at level $k - 1$ that fall under segment c at level k . The robust P^n potential [68] is thus,

$$\psi_c^p(\mathbf{x}_c^{(k-1)}, \mathbf{x}_c^{(k)}) = \phi_c(\mathbf{x}_c^{(k)}) + \sum_{i \in c} \phi_c(\mathbf{x}_c^{(k)}, \mathbf{x}_i^{(k-1)}), \quad (1.26)$$

where $\mathbf{x}_c^{(k)}$ takes on labels from $\mathcal{L} \cup \{L_F\}$, and $\phi_c(\mathbf{x}_c^{(k)})$ is the (super)segment unary potential that has a cost of γ_c^l , if $\mathbf{x}_c^{(k)} = l$, or γ_c^{\max} , if $\mathbf{x}_c^{(k)}$ is assigned the free label L_F , where $\gamma_c^l \leq \gamma_c^{\max}$, $\forall l \in \mathcal{L}$. The pairwise potential [68] is defined as,

$$\phi_c(\mathbf{x}_c^{(k)}, \mathbf{x}_i^{(k-1)}) = \begin{cases} 0 & \text{if } \mathbf{x}_c^{(k)} = L_F \text{ or } \mathbf{x}_c^{(k)} = \mathbf{x}_i^{(k-1)} \\ w_i k_c^{\mathbf{x}_i^{(k-1)}} & \text{otherwise,} \end{cases} \quad (1.27)$$

where w_i are learned weights and k_c^l are costs associated with labeling a variable clique c in level $k - 1$ (*i.e.* child node) with a label l that is different than the label for (super)segment c in level k (*i.e.* parent node). Therefore, the pairwise potential in eqn. 1.27 encourages that all child variables in the lower level take on the same label as the parent node in the higher level. Otherwise there is a cost incurred on each and every variable in the clique taking on a different label. Combined with the unary potential 1.26, the robust P^n potential encourages child variables to take on the same label as the parent variables, but allows the possibility of heterogeneous labeling of the child nodes. More specifically, by ensuring that the constraint $\sum_i w_i k_c^l \geq 2\phi_c(l)$, $\forall l \in \mathcal{L}$, is satisfied, the parent variable will take a label $l \in \mathcal{L}$ if and only if the (weighted) majority of child nodes takes on the same label. Otherwise, if the parent node takes on label L_F , then the child nodes are free to take on any label that minimizes lower level unary and pairwise costs defined by the CRF, with an added cost for a heterogeneous labeling of γ_c^{\max} . In summary, the higher order robust P^n potentials favor homogeneous labelings of (super)segments but allow for the possibility that regions within the (super)segments take on different labels.

The unary potentials over (super)segments are the responses of classifiers trained on normalized histograms of clustered dense (pixel-level) features. The dense features include color, textons, HOG, and pixel location. The classifiers are multiple weak learners trained via AdaBoost [32, 33]. The variables, as define in [68], are set to,

$$\gamma_c^l = \lambda_s |c| \min(-H_l(c) + K, \alpha^h), \quad (1.28)$$

where the log probability of clique (aka (super)segment) c taking on label l is $H_l(c)$ (given by classifier), α^h is a truncation threshold, and $K = \log(\sum_{l \in \mathcal{L}} e^{H_l(c)})$. The other variables in the robust P^n potential are set to $\gamma_c^{\max} = |c|(\lambda_p + \lambda_s \alpha^h)$, and $k_c^l = (\gamma_c^{\max} - \gamma_c^l)/0.1|c|$ (up to 10% of the pixels in a segment can be assigned a different label than the segment variable before the variable is assigned L_F). The pairwise (super)segment potentials $\psi_{cd}(\mathbf{x}_c^{(k)}, \mathbf{x}_d^{(k)})$ are the Euclidean distance between normalized color histograms over pixels within the (super)segments.

What's hidden in eqn. 1.24 for every layer are weight constants, $\lambda_1^{(k)}$ and $\lambda_2^{(k)}$ for the unary and pairwise potentials. In order to learn these parameters the approach taken is to do a layer by layer search for the optimal parameter settings, on a validation set, that minimizes the error between the dominant ground truth label for a clique according to the ground-truth labeling and the label $x_c^{(k)}$ assigned by the *maximum a-posteriori estimate* (MAP) over the CRF.

Inference over the CRF, by computing the most probable label assignment (otherwise known as the MAP estimate) for the energy defined by eqn. 1.24 has been shown to run in polynomial time [99] using graph cut move making algorithms (α -expansion, $\alpha\beta$ -swap).

The ALE system also combines object detection with semantic segmentation by including potentials over detections into the CRF energy. Ladicky et al. argue [71] that since object detectors are good at localizing *things*, which have describable size and shape (as opposed to *stuff* which are shapeless), the detections can be used to improve segmentation accuracy. Object detections also provide object instance level information that semantic segmentation does not; and coupled with the bounding box size, shape, and location information provide rich information for scene understanding.

To incorporate detections from object detectors into the CRF, an additional term is added to the energy in eqn. 1.23. Denoting E_{hier} as the energy in eqn. 1.23, the new energy is defined as [71],

$$E(\mathbf{x}) = E_{\text{hier}}(\mathbf{x}) + \sum_{d \in \mathcal{D}} \psi_d(\mathbf{x}_d, H_d, l_d), \quad (1.29)$$

where \mathcal{D} are the set of detections given by a detection algorithm such as [31]. Each detection has associated with it the bounding box (*i.e.* spatial extent) surrounding the object, the predicted object label l_d , and corresponding label probability H_d . The detector potential introduces an auxiliary variable $y_d \in \{0, 1\}$ that indicates whether the detector prediction is used or not. The form of the detector potential as define by Ladicky et al. [71] is,

$$\psi_d(\mathbf{x}_d, H_d, l_d) = \min_{y_d \in \{0, 1\}} (g(N_d, H_d)y_d - f(\mathbf{x}_d, H_d)y_d), \quad (1.30)$$

where the first term is a cost for having pixels inside the detector bounding box take on different values that the detector label l_d , and the second term is the likelihood of an object being present inside the detector bounding box. The likelihood term is,

$$f(\mathbf{x}_d, H_d) = w_d |\mathbf{x}_d| \max(0, H_d - H_t), \quad (1.31)$$

with H_t a threshold controlling the number of detections. The label inconsistency term, $g(N_d, H_d)$, is defined to be,

$$g(N_d, H_d) = \frac{f(\mathbf{x}_d, H_d)}{p_d |\mathbf{x}_d|} N_d, \quad (1.32)$$

where N_d is the number of pixels inside the detector bounding box having a different label from l_d , and p_d is set to a threshold percentage of inconsistent pixels.

Recall that the first energy term in eqn. 1.29 can be minimized efficiently using graph cut move making algorithms [99]. It turns out that the detector potentials can also be minimized with respect to x_d using $\alpha\beta$ -swap and α -expansion algorithms [71], so inference on the CRF defined by the energy in eqn. 1.29 can be computed in polynomial time.

The addition of the detector potentials help further disambiguate and correct false labellings.

1.1.1.10 Zoom-out convolutional neural network

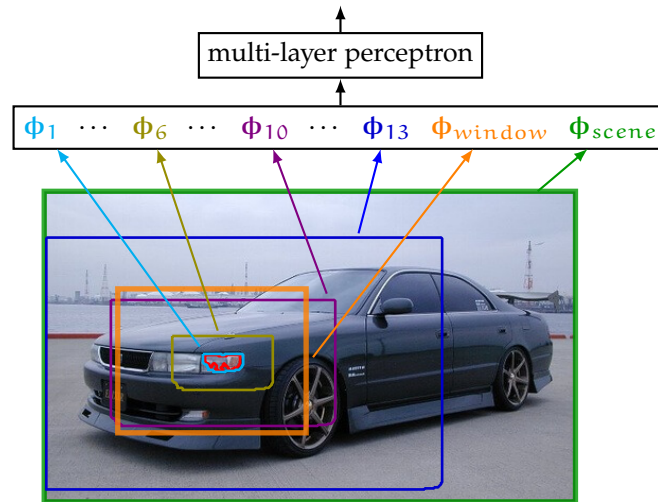


Figure 1.3: For a given superpixel (red) zoom-out features are computed at multiple zoom-out levels (6 levels shown). The features from each level are stacked into a column vector representation of the superpixel, and a multi-layer perceptron is used to predict the superpixel class probabilities.

Semantic segmentation is often viewed as a structured prediction task, because of the relationship between variables in the output space — for example pixels appearing in a similar context take the same segmentation label and the likelihood of pixels taking a particular label are conditionally dependent on what type of scene the image depicts. As the hierarchical CRF model in ALE demonstrated, one common way to do structured prediction is to model the variables and their conditional dependencies using a graphical model and running inference over the graph to compute the most likely labeling. Here we present another approach to doing structured prediction for semantic segmentation that side-steps the issue of explicitly imposing conditional dependencies between variables via a graph structure and higher order potentials. The advantage is a model that avoids the hard or intractable inference and learning that often plagues con-

ventional structured prediction problems, while simultaneously incorporating higher order clique interactions between regions in the image, in an implicit way.

The idea by Mostajabi et al. [82] proposes to label each region in the image by classifying it using features computed on the image. We will assume that the regions are the result of some bottom-up image segmentation algorithm such as SLIC. The task is to semantically label each superpixel by classifying it such that the majority ground-truth label over pixels falling in that superpixel agree with the semantic label predicted by the classifier. This approach has been taken before where the classification is based on features computed over the superpixel. What is new in the approach by Mostajabi is the spatial extent over which features are computed. Instead of computing features limited to the spatial extent of the superpixel, multiple spatial scales of influence or context around the superpixel are also considered. The increasing spatial scales, or *zoom-out levels*, can be broadly categorized as local, proximal, distant, and scene. They can be described as follows,

- *Local* — the spatial extent defined by the superpixel itself. Features computed in this region capture local color, texture pattern, and gradient cues specific to the superpixel. Neighboring superpixels can have very different features, for example if they appear on different objects in the image.
- *Proximal* — regions centered on the superpixel extending over a one or two superpixel neighborhood. Neighboring superpixels will have overlapping proximal regions and their corresponding features will have some similarity. As the distance between superpixels grows beyond the one or two superpixel neighborhood the features computed in their respective proximal regions will capture increasingly different image statistics. Therefore the proximal region features implicitly encode local conditional dependencies between superpixels that are in an approximate neighborhood of each other.
- *Distant* — further along the scale, distant regions are centered on the superpixels and capture a much larger portion of the image than proximal regions. Superpixels that are adjacent have very similar distant level features due to the large overlap in the regions. Distant level features implicitly capture long range dependencies between superpixels in the image. As the superpixels drift further apart their distant level features gradually differ. These higher-order interactions are difficult to incorporate into standard structured prediction models.
- *Scene* — this is at the level of the entire image. Features computed at the scene level capture what the scene is depicting as a whole and provide strong cues as to what object categories might be present in the scene. As such all superpixels share the same scene level features, which provides soft global constraints to the classifier that impact local predictions.

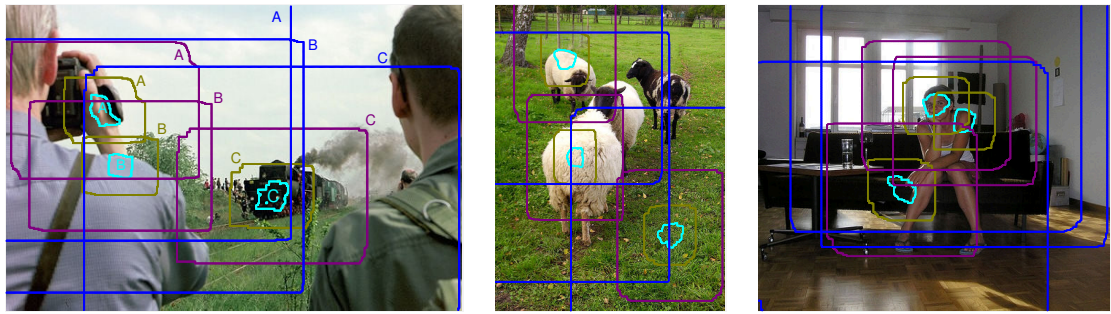


Figure 1.4: Examples of zoom-out regions. We show four out of fifteen levels: 1 (cyan, nearly matching the superpixel boundaries), 6 (olive), 10 (purple) and 13 (blue).

The spatial categories can be further refined along a more fine-grained scale pyramid. A depiction of the features used by the local region classifier is shown in figure 1.3. The features across the spatial regions are concatenated and used as input to the classifier. The classifier, in turn, is trained to predict the likelihood of the superpixel taking on a semantic label. Examples of the different zoom-out regions for three superpixels in various images is shown in 1.4. You will notice superpixels that are closely spaced in the image have overlapping proximal regions but as they are spaced further apart their proximal regions no longer overlap but their distant level regions do. Thus superpixels that are close share much of the same image statistics whereas distant superpixels do not. Note from the figures that if two nearby superpixels are on the same object but with very different local image features there's still a high likelihood that the classifier will assign them the same semantic label, given the fact that they share proximal and distant features. Conversely, if two nearby superpixels are on different objects their respective features computed over local regions will hopefully be different enough to bias the classifier to label them as different semantic classes.

In order to incorporate the concept of multi-scale feature pooling, including scene-level features, with state-of-the-art learned features, Mostajabi et al. use a *convolutional neural network* (CNN) architecture trained on scene level classification. The feature computation at multiple scales centered on a specific location in the image can be mapped directly to the filter response of different convolutional layers in the CNN, corresponding to the different spatial extents. Each filter response in a layer corresponds to a receptive field in the image centered at a particular location. The layer response is a three dimensional *feature map*, that is $w \times h \times d$ dimensional. Responses from different convolutional layers have different feature dimension, d . As you move further up the CNN the feature maps have progressively smaller spatial extents, $w \times h$, due to convolutional kernel stride and feature pooling layers. Inversely, feature map locations from further layers in the CNN have larger receptive field (region of influence) in the image. In order to replicate the zoom-out idea with a CNN the responses of the convolutional layers are upsampled so that their spatial extents match the image size, and subsequently pooled over superpixels to produce scale-space features. Figure 1.5 illus-

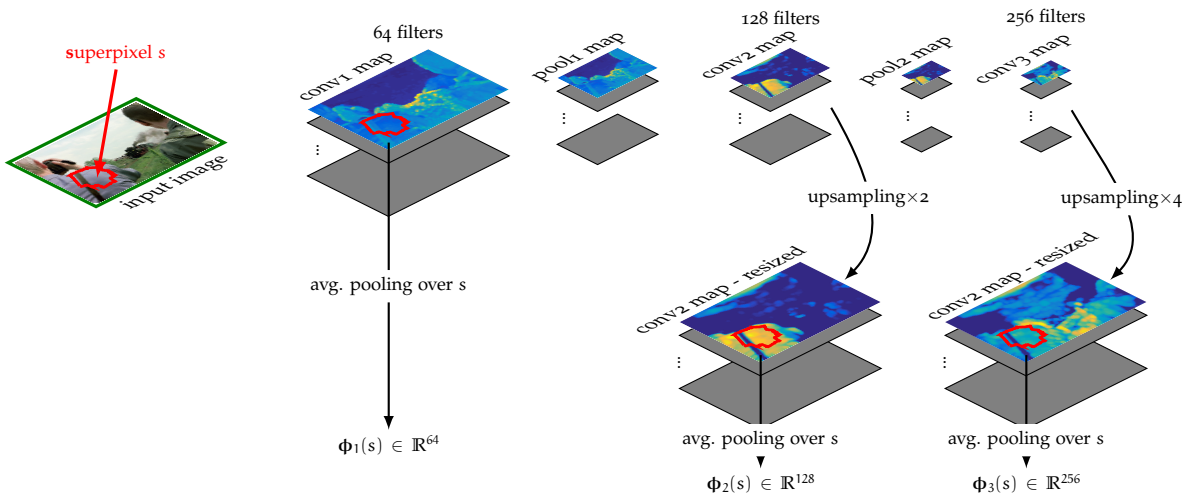


Figure 1.5: Zoom-out network architecture using an image classification CNN backbone, computed over superpixels. The output response from the convolutional layers plus the softmax output (scene level) are up-sampled to the image size and stacked into the final feature map representation over the image. For each superpixel a feature vector representation is constructed by pooling the feature map over the superpixel.

trates how the features for a superpixel are extracted from a CNN. Scene level features are also extracted from the CNN as the final softmax probabilities for each semantic category from the last layer of the CNN.

The CNN can be arbitrary, though deeper networks provide more spatial scales to consider. Mostajabi et al used the popular VGG-16 convolutional neural network [108] as the backbone, that is initially trained on the scene classification task.

The superpixel zoom-out features are next classified. Mostajabi et al. experiment with both linear and non-linear shallow *multilayer perceptron* classifiers, which are trained on Zoom-out features extracted from the training set. The classifier loss they minimize is the standard category classification cross-entropy loss. Note that the zoom-out feature classifier MLP and CNN used for extracting the superpixel features can be combined and trained in an end-to-end fashion so that the CNN feature extraction layers can benefit from supervision on the task of semantic segmentation over superpixels (as opposed to just scene level classification supervision). This segmentation task specific supervision further improves the accuracy (cf. [82]).

Experimental analysis of the relative importance of the features extracted at different scales shows that they all contribute a non-negligible signal toward the prediction of semantic labels [82]. The competitive performance (relative to state-of-the-art semantic segmentation algorithms) of the Zoom-out network coupled with its relative simplicity — and computational efficiency of a feed-forward model (relative to alternative structured prediction models) — make it an attractive semantic segmentation model. Figure 1.6 displays some typical segmentation results from the Zoom-out network.



Figure 1.6: Example semantic segmentation on VOC2012 val images using a 3-layer perceptron classifier used to classify zoom-out features over superpixels across 15 zoom-out levels of a CNN originally trained for scene classification.

The Zoom-out network of Mostajabi *et al.* can also be applied densely (to every pixel) instead of over superpixels. This is done by first converting the CNN backbone into a fully-convolutional CNN where the final fully-connected classification layers are converted to 1×1 -convolutional layers. Additional *skip-connections* are introduced that take the output response of the intermediate convolutional layers, and pass them through a concatenation layer that stacks the intermediate feature maps (after up-sampling to be the same size as the image using bilinear interpolation) into a *hyper-column* [42] representation for every pixel in the output. This feature map is then fed into the final fully-convolutional classification layers of the network followed by softmax activation to make predictions at every pixel. Further dense refinement of the label predictions can then be made by applying efficient approximate inference on a special dense (*i.e.* fully-connected) CRF [2, 65] over the pixels. This CRF uses the pixel label probabilities as unary potentials. The fully-convolutional CNN backbone (minus the CRF) can then be learned in an end-to-end fashion. Typically the CNN is initially trained on a complimentary task (and dataset) such as image classification and then converted into a fully-convolutional network with skip-connections which is then finetuned on the semantic segmentation task (and corresponding dataset). A similar approach is taken by contemporary works such as [18, 19, 42, 75].

1.2 MAP PROBLEM

A *Markov network* — also known as a *Markov random field* — is defined an undirected graph, $G = (V, E)$, with a set of vertices, V , associated with $n = |V|$ random variables $\mathbf{X} = \{X_v | v \in V\}$, and a set of edges, E , between variables associated with the probabilistic relationships between those variables. A Markov network structure encodes

the dependence assumptions associated with the random variables. The variables in the Markov network have the following *Markov properties*:

- any two non-neighboring variables are conditionally independent given all other variables in G ,

$$X_s \perp\!\!\!\perp X_t \mid X_{V \setminus \{s,t\}}, \quad \forall (s,t) \notin E \quad (1.33)$$

- any variable is conditionally independent of all other random variables in G given the random variables that are its immediate neighbors (*i.e.* those it shares an edge with),

$$X_s \perp\!\!\!\perp X_{V \setminus \{s \cup \text{ne}(s)\}} \mid X_{\text{ne}(s)} \quad (1.34)$$

This neighborhood of a node is referred to as its *Markov blanket*.

- any two subsets of variables, S_1 and S_2 , in G are conditionally independent given the subset of variable that connect them,

$$X_{S_1} \perp\!\!\!\perp X_{S_2} \mid X_C, \quad (1.35)$$

where every path from X_{S_1} to X_{S_2} in G pass through some variable(s) in X_C .

We will restrict ourselves to discrete Markov random fields where each random variable X_s takes values from the finite label set $\mathcal{X}_s := \{0, \dots, r-1\}$, so that the random vector $\mathbf{X} \in \mathcal{X}^n := \mathcal{X}_1 \times \dots \times \mathcal{X}_n$, encodes the joint configuration over all the variables.

According to the *Hammersley-Clifford theorem* any probability distribution that is strictly positive satisfies the above Markov properties if and only if it can be factorized according to cliques of the graph. Therefore a Markov random field where $p(\mathbf{x}) > 0$ for all $\mathbf{x} \in \mathcal{X}^n$ can be written as,

$$p(\mathbf{x}) = \frac{1}{Z} \prod_{c \in \mathcal{C}} \psi_c(\mathbf{x}_c), \quad (1.36)$$

where \mathcal{C} is the set of cliques in G , $\mathbf{x}_c = \{x_s \mid s \in c\}$, and $\psi_c(\mathbf{x}_c)$ are functions from $X_c \rightarrow \mathbb{R}$ called *factors* or *clique potentials*. A *clique* is a maximal subgraph of G . A clique, X_c , is *maximal* if any superset containing X_c is not a clique. Equation 1.36 is referred to as either the Gibbs distribution, Gibb random field, or Markov random field. The normalizing constant Z is called the partition function,

$$Z = \sum_{\mathbf{X} \in \mathcal{X}^n} \tilde{p}(\mathbf{X}), \quad (1.37)$$

with unnormalized value,

$$\tilde{p}(\mathbf{X}) = \prod_{c \in \mathcal{C}} \psi_c(\mathbf{x}_c) \quad (1.38)$$

Equivalently, the set \mathcal{C} in the factorization of eqn. 1.36 can be restricted to only contain maximal cliques. This is because any factorization over complete subgraphs can be equivalently written as a factorization over maximal cliques with corresponding clique potentials that are products over all factors whose scope is covered by the maximal clique.

The structure of the Markov network generally does not capture the factorization according to the Gibbs distribution, because the factorization could be over maximal or non-maximal cliques and the Markov network does not show this explicitly. An alternate parameterization of the Markov network is via a *factor graph*. In a factor graph additional factor nodes are introduced. Edges are only between variable nodes and factor nodes. Each factor, ψ , in the factorization is associated with a corresponding factor node in the graph. Variables are connected with a factor node with an edge if the variables are found in the scope of the factor corresponding to the factor node.

An even more explicit parameterization of a Markov network is via *log-linear models*. In this case each factor is written in an equivalent *energy function* form,

$$\psi(\mathbf{x}) = \exp(-\gamma(\mathbf{x})), \quad (1.39)$$

with energy function $\gamma(\mathbf{x}) = -\ln \psi(\mathbf{x})$. The joint probability can then be written as,

$$p(\mathbf{x}) = \frac{1}{Z} \exp\left(-\sum_{\mathbf{c} \in \mathcal{C}} \gamma_{\mathbf{c}}(\mathbf{x}_{\mathbf{c}})\right). \quad (1.40)$$

To get the log-linear representation we can associate one or more *potential functions* with each clique C . More specifically assume a set of potential functions $\{\phi_{\alpha} | \alpha \in \mathcal{J}(C)\}$. A potential function, $\phi : \mathcal{X}^n \rightarrow \mathbb{R}$, associated with a clique C , has \mathbf{x}_C as its scope, and $\mathcal{J}(C)$ is some index set over C . Let $\mathcal{J} = \cup_C \mathcal{J}(C)$ be the union over the index sets of all cliques. The log linear model can be written as,

$$p(\mathbf{x}; \theta) = \frac{1}{Z} \exp\left(\sum_{\alpha \in \mathcal{J}} \theta_{\alpha} \phi_{\alpha}(\mathbf{x})\right), \quad (1.41)$$

with parameters θ_{α} . Notice that any energy function over discrete variables, $\gamma_C(\mathbf{x}_C)$, can be written as a weighted sum, $\sum_{\alpha \in \mathcal{J}(C)} \theta_{\alpha} \phi_{\alpha}(\mathbf{x})$, with appropriate choice of potential functions and α . The above definitions and characterizations of Markov networks can be found in more detail in [61].

In what follows we will review a re-characterization of the MAP inference problem as an integer programming problem attributed to Wainwright *et al.* [118, 119].

If we let $\theta = [\theta_1, \dots, \theta_d]$, where $d = |\mathcal{J}|$, for the collection $\{\theta_{\alpha} | \alpha \in \mathcal{J}\}$ and define the mapping $\phi : \mathcal{X}^n \rightarrow \mathbb{R}^d$, for the collection $\{\phi_{\alpha} | \alpha \in \mathcal{J}\}$, we can write eqn. 1.41 more compactly as,

$$p(\mathbf{x}; \theta) = \frac{1}{Z} \exp\langle \theta, \phi \rangle. \quad (1.42)$$

Equation 1.42 defines a *linear exponential family* of distributions — therefore discrete MRFs are linear exponential families. Each θ defines a different MRF.

The class of random fields that we will focus on are *metric* MRFs with discrete random variables and at most pairwise factors. In fact any Markov random field with discrete random variables and higher order factors can be turned into an equivalent MRF with only pairwise factors (see [119]). For the pairwise MRF the index set is,

$$\mathcal{J} := \{(s;j) \mid s \in \mathcal{V}, j \in \mathcal{X}_s\} \cup \{(st;jk) \mid (s,t) \in \mathcal{E}, (j,k) \in \mathcal{X}_s \times \mathcal{X}_t\} \quad (1.43)$$

The metric pairwise MRF potential functions, ϕ , take specific form of indicator functions. Specifically, the node and pairwise interaction potentials are,

$$\mathbb{I}_{s;j}(x_s) := \begin{cases} 1 & \text{if } x_s = j, \\ 0 & \text{otherwise} \end{cases} \quad \forall s \in \mathcal{V}, j \in \mathcal{X}_s, \quad (1.44)$$

$$\mathbb{I}_{st;jk}(x_s, x_t) := \begin{cases} 1 & \text{if } x_s = j \text{ and } x_t = k, \\ 0 & \text{otherwise} \end{cases} \quad \forall (s,t) \in \mathcal{E}, (j,k) \in \mathcal{X}_s \times \mathcal{X}_t, \quad (1.45)$$

and are referred to as the *canonical overcomplete representation*, with the corresponding θ called the *canonical parameters* [118]. The representation is overcomplete because they satisfy certain linear constraints, namely,

$$\sum_{j \in \mathcal{X}_s} \mathbb{I}_{s;j}(x_s) = 1 \quad \forall s \in \mathcal{V}, \quad (1.46a)$$

$$\sum_{(j,k) \in \mathcal{X}_s \times \mathcal{X}_t} \mathbb{I}_{st;jk}(x_s, x_t) = 1 \quad \forall (s,t) \in \mathcal{E}, \quad (1.46b)$$

$$\sum_{j \in \mathcal{X}_s} \mathbb{I}_{st;jk}(x_s, x_t) = \mathbb{I}_{t;k}(x_t) \quad \forall (s,t) \in \mathcal{E} \quad \forall k \in \mathcal{X}_t, \quad (1.46c)$$

Plugging eqns. 2.34 and 2.35 into eqn. 1.42 and using the index set in eqn. 1.43 the joint probability distribution for the pairwise MRF can be written as,

$$p(\mathbf{x}; \theta) = \exp \left(\sum_{s \in \mathcal{V}} \sum_{j \in \mathcal{X}_s} \theta_{s;j} \mathbb{I}_{s;j}(x_s) + \sum_{(s,t) \in \mathcal{E}} \sum_{(j,k) \in \mathcal{X}_s \times \mathcal{X}_t} \theta_{st;jk} \mathbb{I}_{st;jk}(x_s, x_t) - A(\theta) \right), \quad (1.47)$$

where $A(\theta) := \ln Z(\theta)$. A more compact representation can be written if the following substitutions are made,

$$\theta_s(x_s) := \sum_{j \in \mathcal{X}_s} \theta_{s;j} \mathbb{I}_{s;j}(x_s), \quad (1.48)$$

$$\theta_{st}(\mathbf{x}_s, \mathbf{x}_t) := \sum_{(j,k) \in \mathcal{X}_s \times \mathcal{X}_t} \theta_{st;jk} \mathbb{I}_{st;jk}(\mathbf{x}_s, \mathbf{x}_t), \quad (1.49)$$

into eqn. 1.47 resulting in the pairwise MRF joint probability distribution,

$$p(\mathbf{x}; \boldsymbol{\theta}) = \exp \left(\sum_{s \in \mathcal{V}} \theta_s(\mathbf{x}_s) + \sum_{(s,t) \in \mathcal{E}} \theta_{st}(\mathbf{x}_s, \mathbf{x}_t) - A(\boldsymbol{\theta}) \right). \quad (1.50)$$

In this thesis we will only be concerned with a specific type of inference problem — namely finding the joint configuration \mathbf{x} that maximizes the distribution $p(\mathbf{x}; \boldsymbol{\theta})$ specified by a particular $\boldsymbol{\theta}$. This is known as the *maximum a posterior* or MAP assignment problem. Note that there can be multiple maximizing assignments. Formally we want to find an assignment \mathbf{x}^* such that,

$$\mathbf{x}^* \in \{\mathbf{x} \in \mathcal{X}^n \mid p(\mathbf{x}; \boldsymbol{\theta}) \geq p(\mathbf{y}; \boldsymbol{\theta}), \forall \mathbf{y} \in \mathcal{X}^n\} \quad (1.51)$$

Notice that in eqn. 1.50, $A(\boldsymbol{\theta})$ is independent of \mathbf{x} , so the value of the assignment that maximizes the joint probability is equivalent to,

$$\max_{\mathbf{x} \in \mathcal{X}^n} \langle \boldsymbol{\theta}, \boldsymbol{\phi}(\mathbf{x}) \rangle := \max_{\mathbf{x} \in \mathcal{X}^n} \sum_{s \in \mathcal{V}} \theta_s(\mathbf{x}_s) + \sum_{(s,t) \in \mathcal{E}} \theta_{st}(\mathbf{x}_s, \mathbf{x}_t). \quad (1.52)$$

A maximizing assignment is thus,

$$\mathbf{x}^* := \operatorname{argmax}_{\mathbf{x} \in \mathcal{X}^n} \langle \boldsymbol{\theta}, \boldsymbol{\phi}(\mathbf{x}) \rangle. \quad (1.53)$$

Equation 1.52 is an linear integer program (IP) because $\mathbf{x} \in \mathcal{X}^n$ take on integer values and both the constraint set and the objective function are linear. This integer program is a discrete combinatorial optimization problem that is known to be NP-hard to solve for general graphs [119]. To overcome this problem the integer program can be relaxed into a continuous *linear program*.

Take the set $\mathcal{P} := \{p(\mathbf{x}) \mid p(\mathbf{x}) \geq 0, \sum_{\mathbf{x}} p(\mathbf{x}) = 1\}$ of all probability distributions on \mathbf{x} . It is easy to see that the following equality holds,

$$\max_{\mathbf{x} \in \mathcal{X}^n} \langle \boldsymbol{\theta}, \boldsymbol{\phi}(\mathbf{x}) \rangle = \max_{p \in \mathcal{P}} \sum_{\mathbf{x} \in \mathcal{X}^n} p(\mathbf{x}) \langle \boldsymbol{\theta}, \boldsymbol{\phi}(\mathbf{x}) \rangle, \quad (1.54)$$

because for any \mathbf{x} that satisfies the LHS there exists a probability distribution $p(\cdot)$ that puts all probability mass on \mathbf{x} so the value of the RHS is at least as large as the LHS. The RHS is also a convex combination of $\langle \boldsymbol{\theta}, \boldsymbol{\phi}(\mathbf{x}) \rangle$ terms so cannot be any larger than $\max_{\mathbf{x} \in \mathcal{X}^n} \langle \boldsymbol{\theta}, \boldsymbol{\phi}(\mathbf{x}) \rangle$.

Expanding the RHS term of eqn. 1.54 we get,

$$\max_{\mathbf{x} \in \mathcal{X}^n} \langle \boldsymbol{\theta}, \boldsymbol{\phi}(\mathbf{x}) \rangle = \max_{\mathbf{p} \in \mathcal{P}} \sum_{\mathbf{x} \in \mathcal{X}^n} p(\mathbf{x}) \left(\sum_{s \in V} \theta_s(x_s) + \sum_{(s,t) \in E} \theta_{(s,t)}(x_s, x_t) \right) \quad (1.55)$$

$$\begin{aligned} &= \max_{\mathbf{p} \in \mathcal{P}} \sum_{s \in V} \sum_{j \in \mathcal{X}_s} \theta_{s;j} \sum_{\mathbf{x} \in \mathcal{X}^n} p(\mathbf{x}) \mathbb{I}_{s;j}(x_s) + \\ &\quad + \sum_{(s,t) \in E} \sum_{(j,k) \in \mathcal{X}_s \times \mathcal{X}_t} \theta_{st;jk} \sum_{\mathbf{x} \in \mathcal{X}^n} p(\mathbf{x}) \mathbb{I}_{st;jk}(x_s, x_t), \end{aligned} \quad (1.56)$$

We can define the following quantities,

$$\mu_{s;j} := \sum_{\mathbf{x} \in \mathcal{X}^n} p(\mathbf{x}) \mathbb{I}_{s;j}(x_s) = \mathbb{E}_{\mathbf{p}} [\mathbb{I}_{s;j}(x_s)] = \mathbb{P}[X_s = j], \quad (1.57)$$

$$\mu_{st;jk} := \sum_{\mathbf{x} \in \mathcal{X}^n} p(\mathbf{x}) \mathbb{I}_{st;jk}(x_s, x_t) = \mathbb{E}_{\mathbf{p}} [\mathbb{I}_{st;jk}(x_s, x_t)] = \mathbb{P}[X_s = j \wedge X_t = k], \quad (1.58)$$

called mean parameters which have intuitive meaning — namely $\mu_{s;j}$ is the node marginal probability that random variable x_s takes label j , and $\mu_{st;jk}$ is the edge marginal probability of the joint assignment ($x_s = j, x_t = k$). Plugging definitions 1.57 and 1.58 into eqn. 1.56 we get,

$$\max_{\mathbf{x} \in \mathcal{X}^n} \langle \boldsymbol{\theta}, \boldsymbol{\phi}(\mathbf{x}) \rangle = \max_{\mathbf{p} \in \mathcal{P}} \sum_{s \in V} \sum_{j \in \mathcal{X}_s} \theta_{s;j} \mu_{s;j} + \sum_{(s,t) \in E} \sum_{(j,k) \in \mathcal{X}_s \times \mathcal{X}_t} \theta_{st;jk} \mu_{st;jk}. \quad (1.59)$$

Similar to $\boldsymbol{\phi}$ we let $\boldsymbol{\mu} = \{\mu_\alpha \mid \alpha \in \mathcal{J}\}$. We can define the set of all possible marginal probabilities on graph G as,

$$\mathbb{M}(G) := \{\boldsymbol{\mu} \in \mathbb{R}^d \mid \exists p(\cdot) \in \mathcal{P} \text{ s.t. } \mu_{s;j} = \mathbb{E}_{\mathbf{p}} [\mathbb{I}_{s;j}(x_s)], \mu_{st;jk} = \mathbb{E}_{\mathbf{p}} [\mathbb{I}_{st;jk}(x_s, x_t)]\}. \quad (1.60)$$

$\mathbb{M}(G)$ is called a *marginal polytope* [118]. From $\mathbb{M}(G)$ we see that searching over probability distributions \mathcal{P} maps to searching over $\boldsymbol{\mu}$, which means that the RHS of eqn. 1.59 can be written as,

$$\max_{\mathbf{x} \in \mathcal{X}^n} \langle \boldsymbol{\theta}, \boldsymbol{\phi}(\mathbf{x}) \rangle = \max_{\boldsymbol{\mu} \in \mathbb{M}(G)} \sum_{s \in V} \sum_{j \in \mathcal{X}_s} \theta_{s;j} \mu_{s;j} + \sum_{(s,t) \in E} \sum_{(j,k) \in \mathcal{X}_s \times \mathcal{X}_t} \theta_{st;jk} \mu_{st;jk} \quad (1.61)$$

$$= \max_{\boldsymbol{\mu} \in \mathbb{M}(G)} \langle \boldsymbol{\theta}, \boldsymbol{\mu} \rangle. \quad (1.62)$$

Equation 1.62 is the linear programming (LP) relaxation of the original MAP integer program.

Note that $\mathbb{M}(G)$ is the convex hull of the overcomplete representation defined in eqn. 2.34 and eqn. 2.35 over the finite index set in eqn. 1.43. These indicator functions define the extreme points of $\mathbb{M}(G)$. Since the extreme points are indicator functions

they take $\{0, 1\}$ values, which means they are all integral. From standard linear programming optimization theory the optimal solution of an LP always lies at an extreme point of the feasible set (*i.e.* one of the vertices of $\mathbb{M}(G)$).

For each $\mathbf{x} \in \mathcal{X}^n$ the canonical overcomplete representation $\Phi(\mathbf{x})$ corresponds to an extreme point $\mu_{\mathbf{x}}$ of $\mathbb{M}(G)$, thus the optimal solution is integral and in one-to-one correspondence with assignments \mathbf{x} . Moreover this means that $\mathbb{M}(G)$ has $|\mathcal{X}^n|$ extreme points, which is exponential in n . Optimization over an exponential number of constraints is not feasible so a simpler (read fewer constraints) outer bound on the marginal polytope is desired.

According to the *Minkowski-Weyl theorem* any convex hull over a finite set of vectors can be represented equivalently by the intersection of a finite number of linear half-spaces (*i.e.* of the form $\{\mu : \mathbf{a}^T \mu \leq b\}$ for some $\mathbf{a} \in \mathbb{R}^d$ and $b \in \mathbb{R}$). Included in the half-space representation of $\mathbb{M}(G)$ the linear inequality (half-space) constraints also include the equality constraints that are a consequence of the overcomplete representation. They are analogous to the consistency constraints in eqns. 1.46a–1.46c, namely,

$$\sum_{j \in \mathcal{X}_s} \mu_{s;j}(\mathbf{x}_s) = 1 \quad \forall s \in V, \quad (1.63a)$$

$$\sum_{(j,k) \in \mathcal{X}_s \times \mathcal{X}_t} \mu_{st;jk}(\mathbf{x}_s, \mathbf{x}_t) = 1 \quad \forall (s, t) \in E, \quad (1.63b)$$

$$\sum_{j \in \mathcal{X}_s} \mu_{st;jk}(\mathbf{x}_s, \mathbf{x}_t) = \mu_{t;k}(\mathbf{x}_t) \quad \forall (s, t) \in E \quad \forall k \in \mathcal{X}_t, \quad (1.63c)$$

as well as non-negativity constraints on the marginal probabilities (*i.e.* $\mu_{\alpha} \geq 0$ for all $\alpha \in \mathcal{J}$). Note that each of the above equality constraints can be written as two inequality constraints — *i.e.* the constraint $\mathbf{a}^T \mu = b$ is equivalent to maintaining the following two constraints: $\mathbf{a}^T \mu \leq b$ and $-\mathbf{a}^T \mu \leq -b$.

It turns out that for general graphs with cycles representing the marginal polytope $\mathbb{M}(G)$ as an intersection of half-spaces, or *facets*, becomes difficult because the number of half-spaces becomes exponential. Other than for tree structured graphs the number of facets of $\mathbb{M}(G)$ in a general graph are not known. Instead a simpler outer bound on $\mathbb{M}(G)$ can be constructed by simply considering the intersection of a subset of the half-space constraints, namely those in eqns. 1.63a– 1.63c, along with the non-negativity constraint on μ . This gives the *local polytope* which is set of locally consistent marginal distributions [118, 119],

$$\mathbb{L}(G) := \{\mu \in \mathbb{R}_+^d \mid \text{eqns. 1.63a– 1.63c hold}\} \quad (1.64)$$

$\mathbb{L}(G)$ is the intersection of a subset of the half-space constraints required to represent $\mathbb{M}(G)$, thus $\mathbb{M}(G)$ is a subset of $\mathbb{L}(G)$. It can be shown [118] that for trees (*i.e.* any acyclic connected graph) $\mathbb{L}(G) = \mathbb{M}(G)$. For general graphs with cycles though $\mathbb{M}(G)$ will be a strict subset of $\mathbb{L}(G)$. The number of facets of $\mathbb{L}(G)$ is polynomial in graph

size. The number of extreme points of $\mathbb{L}(G)$ is larger than $\mathbb{M}(G)$ for general graphs, which include the integral extreme points, $\{\mu_x \mid x \in \mathcal{X}^n\}$, plus a set of fractional extreme points that lie outside of $\mathbb{M}(G)$, the total number of which is unknown for general graphs. But that fact that $\mathbb{L}(G)$ can be represented as polynomial number of facets (*i.e.* inequality constraints) means that the following alternate problem,

$$\max_{\mu \in \mathbb{L}(G)} \langle \theta, \mu \rangle \tag{1.65}$$

can be efficiently solved. From eqns. 1.61–1.62 and the definition of the local polytope in eqn. 1.64 we have the following relations,

$$\max_{x \in \mathcal{X}^n} \langle \theta, \phi(x) \rangle = \max_{\mu \in \mathbb{M}(G)} \langle \theta, \mu \rangle \leq \max_{\mu \in \mathbb{L}(G)} \langle \theta, \mu \rangle \tag{1.66}$$

The relaxation on the RHS of eqn. 1.66 is tight for tree structured graphs, but is not guaranteed to be tight for general graphs with cycles. Solutions to the RHS are optimal (*i.e.* the relaxation is tight) if they lie at one of the integral vertices but on general graphs with cycles the solutions are often at one of the fractional vertices. Much work has been done to develop algorithms that give the tightest upper bound on the solution, and the relationship between the the RHS relaxation (and its dual) and various efficient approximate MAP inference algorithms such as *tree-reweighted max-product message-passing* [118] and *dual decomposition* [64] have been established.

The MAP integer program and its linear relaxation formulation described above can be credited to Wainwright *et al.* and a more detailed exposition can be found in the respective material [118, 119].

The primary objective of the research efforts described in this thesis is to improve semantic segmentation. Typically, improving on an existing segmentation model means devising a new model that produces more accurate segmentations. There are a number of sources of error in any model that need to be addressed in order to improve upon it. *Approximation error* — the error due to limitations imposed by the choice of model class — is addressed by devising more accurate, and often more complex, models for semantic segmentation. Unfortunately, as is often the case, more complex models exhibit more optimization and estimation error. When models become too complex for exact inference the approximate inference surrogate methods introduce *optimization error*. More complex models often incorporate higher order interactions between variables and typically have more free variables — all of which require more examples to train. The limitation of a finite training set to train the more complex model leads to larger *estimation error*. Worse yet, it may not even be clear how to incorporate certain higher-order information into a model for segmentation. Even if we are able to, we may end up with models that are intractable to train or do inference on.

For all of the above reasons coming up with a new model can be difficult. Suppose we would like to improve upon an existing discrete semantic segmentation model which can be trained efficiently on a finite training set and on which inference is tractable. Without loss of generality, given an image, the model is trained to minimize the average error over the training set between the segmentation it produces and the ground-truth for the image. At test time, given an image, we use the trained model to infer the most likely (read probable) semantic segmentation of the image. When we are working with a probabilistic model this segmentation is the *maximum a-posteriori* (MAP) solution (or MAP assignment). Without loss of generality we'll use MAP solution to mean the most likely segmentation returned by the model irrespective of it being a probabilistic model or not. We can assume that the model assigns a score to every possible labelling (*i.e.* assignment to all the variables over the image), indicating how likely the labeling is a correct segmentation of the image. Alternatively, we can associate a probability with the likelihood of the image returning a certain segmentation for an image.

When we devise a more accurate segmentation model in effect what we want to achieve is a model that produces a MAP solution that is at least as close to the ground-truth segmentation for the image as the MAP solution produced by a less accurate model.

However, the more accurate model might be intractable or at best comes at a cost of higher estimation and approximation error.

Instead we can consider using the less accurate model to output multiple highly probable solutions, not just the MAP. One of these other solutions might be a more accurate segmentation of the image. We can then consider returning a set of segmentation for the image or pick a single one from the set. If we consider that we are reasonably confident in our sub-optimal segmentation model to return to give high probability to solutions that "do the right thing" in many areas of a typical image, then by producing multiple high probability segmentations from the model we are considering alternate explanations that the model exhibits for the same image. This approach is analogous to cascade models [101, 117, 122] where successive stages of the cascade refine the output of previous stages. Since the space of segmentations (*i.e.* labelings over (super)pixels) is exponential, by producing an initial set of segmentations, instead of just the MAP, and then refining it simplifies the inference problem by reducing it from a 1-out-of- $|\mathcal{L}|^n$ to a 1-out-of- M inference task (where \mathcal{L} is the cardinality of the label set on each of the n variables, and M is the number of high probability segmentations in the set, where $M \ll |\mathcal{L}|^n$). By producing not just one but multiple high probability segmentations we are simultaneously providing an explicit way to manage the uncertainty in the model. That is to say, compared to a single MAP solution, we are better summarizing the uncertainties that the model has about the output space of labellings.

The problem of producing the M most probable solutions, which are different from MAP and each other, is called the M-BEST MAP problem. We will see that in fact this idea has been studied in the context of problems outside segmentation and vision. We will review the most well known approaches.

We will show that for the semantic segmentation task the M-BEST segmentations are not an ideal set of segmentations of an image. This is because the M-BEST formulation only enforces the segmentations not to be the same — there is no explicit control on how diverse the segmentations in the set are. Contrary to problems in other domains, generating a set of segmentations that are simultaneously *highly probable* and *diverse* is a better way of managing uncertainty in the segmentation task. To this end, this chapter presents the *DivMBEST* problem that produces a set of highly probable segmentations that are different from the MAP solution (and each other), with explicit control over the amount of diversity between solutions. Intuitively the goal of the *DivMBEST* approach is to construct a set of segmentations that correspond to the modes of the output distribution of the underlying segmentation model. We will show that *DivMBEST* is a very general framework that can be applied to virtually any tractable segmentation model, and it can be particularly efficient when we consider special forms of dissimilarity between solutions. In fact *DivMBEST*, like the M-BEST algorithm, can be applied to any problem that can benefit from inferring more than just the MAP solution. We also show that *DivMBEST* generalized the M-BEST method and more generally contains other related formulations as special cases.

For the case of a probabilistic segmentation model, a simple alternate way to generate multiple segmentations is to sample from it, such as with Markov chain Monte Carlo (MCMC) sampling. There have been a number of works [5, 88, 89] that take this strategy. It could, however, be a prohibitively time consuming approach, because of the time required to return samples from modes with small support. Additionally, in contrast to the *DivMBEST* approach, there isn't any explicit control over diversity in the set of sampled solutions, which would necessitate sampling a larger set to cover the space of alternate explanations of the image. Related to *DivMBEST*, Papandreou and Yuille [87] present an approach (perturb-and-MAP) to sample from a discrete probabilistic model (e.g. random field) by perturbing the model parameters with random noise and solving for the MAP solution using existing discrete optimization algorithms. This extends deterministic MAP inference to non-deterministic iid sampling of the model distribution. In contrast to perturb-and-MAP the *DivMBEST* approach modifies the model parameters in a deterministic way resulting in a set of highly probable diverse solutions.

In this chapter we review the related M-BEST algorithms and present the *DivMBEST* formulation, limiting the discussion to the case of discrete probabilistic models for ease of exposition. We formulate the *DivMBEST* problem as an integer program (see § 1.2) minimizing a discrete energy (probability distribution) model over a set of random variables subject to diversity constraints on the solutions and consider a linear programming relaxation of it. We present a greedy iterative algorithm to efficiently compute the *DivMBEST* solutions, as well as a gradient ascent method to set search over the diversity parameters. We show that for certain measures of diversity the LP dual of the *DivMBEST* problem enjoys some nice theoretical guarantees. In subsequent chapters we show the superiority of *DivMBEST* over MAP, and M-BEST MAP inference, for various segmentation tasks. In order to handle the 1-out-of-M inference task we also introduce an approach to rank the *DivMBEST* segmentation sets in order to return a single segmentation.

2.1 RELATED WORK

In the next section we begin with a review of the M-BEST MAP problem and related literature.

2.1.1 M-BEST

One of the earliest methods to address the M-BEST problem was by Lawler [74]. It is a simple and general method for computing the M optimal solutions of discrete optimization problems, and is agnostic to the optimization algorithm used to compute

the solution of any specific problem. It is a divide-and-conquer method that solves multiple independent discrete optimization problems that are created by iteratively partitioning the assignment space. We'll outline the basic method here (cf. [74]).

Without loss of generality the method assumes a set of binary variables, $x_1, \dots, x_n \in \{0, 1\}$. Note that in problems where the discrete variables take on more than two values one can make a straightforward transformation to $\{0, 1\}$ -valued variables — e.g. $\forall x_i \in \{0, \dots, \ell - 1\}$ replace with ℓ variables: $x_{i;j} \in \{0, 1\}$, where $x_{i;j} = \llbracket x_i == j \rrbracket$, with an implicit constraint that $\sum_j x_{i;j} = 1$.

The task is to return the top-M solutions to a discrete optimization problem (*w.l.o.g.* assume a minimization) over the x_i 's — that is the M solutions that best minimize the problem. The method starts by computing the optimal solution to the original problem. It then iteratively partitions the assignment space into disjoint sets in a way that removes the previous top $m - 1$ solutions from consideration, and for each set solves a new optimization problem returning a candidate solution, whereby the next best solution is the one in the set of candidates with lowest value.

The algorithm is reproduced in alg. 2. More specifically, in each iteration m , of alg. 2, $n - s$ new problems are created, where s is the number of variables that were fixed in the optimization problem that produced the previous solution $x^{(m-1)}$. The key, in line 9 of alg. 2, is to partition the assignment space into $n - s$ disjoint sets, P_1, \dots, P_{n-s} . Each problem P_j has the first s variables plus an additional j variables fixed. The j additional variables are fixed in such a way to remove $x^{(m-1)}$ from the set of feasible solutions to P_j . Note that if for any j , x_{s+j} is set to $1 - x_{s+j}^{(m-1)}$, then $x^{(m-1)}$ has been removed from the set of feasible solutions for P_j . Additionally the set of feasible solutions for P_j is disjoint from the rest of the problems $\{P_i \mid i \neq j\}$. Moreover,

$$\bigcup_{j=1}^{n-s} P_j = X - \{x^{(m-1)}\}.$$

Since in each iteration the s variables from the problem used to produce solution $x^{(m-1)}$ remain fixed all the previous optimal solutions are also removed from consideration in each problem, *i.e.* in iteration m we have

$$\bigcup_{j=1}^{n-s} P_j = X - \{x^1, \dots, x^{(m-1)}\}.$$

Effectively alg. 2 recursively partitions the assignment space. Each new partitioning occurs on the set of feasible solutions used to constraint the problem that produced the optimal solution in the previous round. For example in the first iteration the partitioning is over the entire assignment space because no variables were fixed in the optimization problem that compute the initial best assignment $x^{(1)}$.

The computational complexity of computing the top-M solutions using alg. 2 is $\mathcal{O}(Mn\rho(n))$, where $\rho(n)$ is the cost of solving a single optimization problem over n variables. Since it is a general M-BEST algorithm it is not tailored to any specific discrete optimization problem so it cannot simultaneously solve for the top M solutions. This makes the

Algorithm 2 M-BEST-Lawler [74]

```

1:  $OPTS = \emptyset, TOP-M = \emptyset.$ 
2:  $m \leftarrow 1$ : compute optimal solution  $\mathbf{x}^{(1)} \leftarrow \operatorname{argmax}_{\mathbf{x}} f(\mathbf{x})$ , without fixing any variables in  $\mathbf{x}$ 
3:  $OPTS \leftarrow OPTS \cup (\mathbf{x}^{(1)}, \emptyset).$ 
4: repeat
5:    $(\mathbf{x}^{(m)}, P^{(m)}) \leftarrow \operatorname{bestsol}(OPTS), TOP-M \leftarrow \mathbf{x}^{(m)}$   $\triangleright$  bestsol returns the minimum value solution along with the set of fixed variables in the corresponding problem  $P^{(m)}$ .
6:   if  $m = M$  then
7:     break;
8:   end if
9:   Let  $x_1, \dots, x_s$  be the variables that were fixed in the problem solved to get  $\mathbf{x}^{(m)}$ , i.e.  $P^{(m)}$ . Construct  $(n - s)$  new problems by fixing additional variables:
       $(P_1)$ :  $x_1 = x_1^{(m)}, \dots, x_s = x_s^{(m)}, x_{s+1} = 1 - x_{s+1}^{(m)}$ 
       $(P_2)$ :  $x_1 = x_1^{(m)}, \dots, x_s = x_s^{(m)}, x_{s+1} = x_{s+1}^{(m)}, x_{s+2} = 1 - x_{s+2}^{(m)}$ 
       $(P_3)$ :  $x_1 = x_1^{(m)}, \dots, x_s = x_s^{(m)}, x_{s+1} = x_{s+1}^{(m)}, x_{s+2} = x_{s+2}^{(m)}, x_{s+3} = 1 - x_{s+3}^{(m)}$ 
       $\vdots$ 
       $\vdots$ 
       $(P_{n-s})$ :  $x_1 = x_1^{(m)}, \dots, x_s = x_s^{(m)}, x_{s+1} = x_{s+1}^{(m)}, x_{s+2} = x_{s+2}^{(m)}, \dots, x_{n-1} = x_{n-1}^{(m)}, x_n = 1 - x_n^{(m)}$ 
10:  for  $j = 1, \dots, n - s$  do
11:    Solve  $\mathbf{x}^{P_j} \leftarrow \operatorname{argmin}_{\mathbf{x} \text{ s.t. } P_j \text{ satisfied}} f(\mathbf{x})$ 
12:     $OPTS \leftarrow OPTS \cup (\mathbf{x}^{P_j}, P_j).$ 
13:  end for
14:   $m \leftarrow m + 1$ 
15: until  $m = M$ 

```

algorithm less efficient than specialized inference methods and in each iteration of the algorithm $n - s$ separate optimization problems need to be solved.

The space required for the algorithm is $M(n - 1)$ because at most that many items are in $OPTS$.

2.1.2 M-BEST and Max-Flow Propagation

Dawid [25] and later Nilsson [84] extended the M-BEST task to the problem of computing optimal configurations over directed and undirected graphical models with cycles. Their approach relies on the ability to exactly and efficiently compute the maximizing assignment to a joint distribution, over a set of random variables, which factorizes according to cliques in the graphical model. In order to achieve this, the approach is

based on constructing a higher order structure, called a *junction tree*, from the graph. We'll denote the junction tree with \mathcal{T} . We won't explain the junction tree construction here (details can be found in [47, 61, 73]) but instead mention important properties. In a junction tree nodes correspond to cliques of random variables from the set $\{C_i : i \in \mathcal{C}\}$, where \mathcal{C} is an index set over cliques. Edges in the set $\{S_{ij} : (i, j) \in \mathcal{S}\}$, connect adjacent nodes C_i and C_j , and are associated with the variables shared between the two cliques, *i.e.* $S_{ij} = C_i \cap C_j$. The edge sets S_{ij} are called *separators*. For any variable x_u , if it appears in any two cliques C_i and C_j of the junction tree, then it must also appear in all the cliques in the unique path from C_i to C_j . This is known as the *junction tree property* [61, 84].

The joint probability function, f , over random variables X , taking values $\mathbf{x} \in \mathcal{X}$, factorizes according to the cliques and edges in the tree as follows,

$$f(\mathbf{x}) = \frac{\prod_{i \in \mathcal{C}} f_{C_i}(\mathbf{x}_{C_i})}{\prod_{(i,j) \in \mathcal{S}} f_{S_{ij}}(\mathbf{x}_{S_{ij}})}, \quad (2.1)$$

where f_C and f_S are non-negative real functions on cliques and edges respectively. As before these functions are referred to as potentials. Since computing the probabilities of f over the space of configurations \mathcal{X} can often be exponential in the number of variables, a factorization of f over cliques can be computationally advantageous if the clique sizes are limited. Using a message-passing algorithm that limits computation of (max) probabilities over just the cliques allows for efficient inference, as long as the *tree width* (*i.e.* the maximum size of any clique in the tree) is small.

To compute the assignment of variables $\mathbf{x} \in \mathcal{X}$ that maximizes f a max-flow message passing algorithm over the junction tree is used.

2.1.2.1 Max-flows over Junction Tree

Assume that we are given an initial factorization of f over a set of clique and separator potentials,

$$(\{f_{C_i} : i \in \mathcal{C}\}, \{f_{S_{ij}} : (i, j) \in \mathcal{S}\}), \quad (2.2)$$

A message from node C_i to an adjacent node C_j is defined as the normalized max-flow from C_i to C_j :

$$\delta_{i \rightarrow j} = \frac{f'_{S_{ij}}}{f_{S_{ij}}}, \quad (2.3)$$

where,

$$f'_{S_{ij}} = \max_{C_i \setminus S_{ij}} f_{C_i}. \quad (2.4)$$

Given two sets $B \subset A$, and function g on \mathcal{X}_B , the above max notation means,

$$\max_{A \setminus B} g(\mathbf{x}_B) = \max_{\mathbf{z} \in \mathcal{X}_A} \{g(\mathbf{z}) : \mathbf{z}_B = \mathbf{x}_B\}, \quad (2.5)$$

where $\mathbf{x}_B \in \mathcal{X}_B \doteq \times_{u \in B} \mathcal{X}_u$. The update to clique potential f_{C_j} is then,

$$f'_{C_j} = f_{C_j} \cdot \delta_{i \rightarrow j}. \quad (2.6)$$

Message-passing proceeds with the following update schedule: pick any node in \mathcal{T} , say C_1 , as the root node. Starting from the leaves of \mathcal{T} pass max-flow messages up to C_1 and back down to the leaves. A clique sends a message to its neighbor C_j once it has received all messages from its neighbors with possible exception of C_j , such a message is called an *active* max-flow. After this two-phase propagation of messages the potentials are guaranteed to have reached equilibrium resulting in *max-marginal* potentials [25],

$$(\{\hat{f}_{C_i} : i \in \mathcal{C}\}, \{\hat{f}_{S_{ij}} : (i, j) \in \mathcal{S}\}), \quad (2.7)$$

where the max-marginal potential over set A is defined to be,

$$\hat{f}_A(\mathbf{x}_A) = \max_{\mathbf{z} \in \mathcal{X}} \{f(\mathbf{z}) : \mathbf{z}_A = \mathbf{x}_A\}. \quad (2.8)$$

An important property of the update rule is that f in eqn. 2.1 is invariant to max flow updates. To see this consider adjacent cliques C_i , C_j and the separator, S_{ij} between them. A max-flow update gives,

$$\begin{aligned} f'_{S_{ij}} &= \max_{C_i \setminus S_{ij}} f_{C_i}, & \delta_{i \rightarrow j} &= \frac{f'_{S_{ij}}}{f_{S_{ij}}} \\ f'_{C_j} &= f_{C_j} \cdot \delta_{i \rightarrow j} = f_{C_j} \cdot \frac{f'_{S_{ij}}}{f_{S_{ij}}}, & \frac{f'_{C_j}}{f'_{S_{ij}}} &= \frac{f_{C_j} \cdot f'_{S_{ij}}}{f'_{S_{ij}} \cdot f_{S_{ij}}} = \frac{f_{C_j}}{f_{S_{ij}}}, \end{aligned} \quad (2.9)$$

where the RHS of the bottom row shows the invariance in max-flow update to f in the contribution by C_j and S_{ij} .

Also note the following property [84],

$$\max_{C_i \setminus S_{ij}} \hat{f}_{C_i} = \hat{f}_{S_{ij}} = \max_{C_j \setminus S_{ij}} \hat{f}_{C_j}, \quad (2.10)$$

known as the *max-consistency* property, which holds after computing the max-marginal potentials. Also note the following theorem,

Theorem 2.1.1 (Max-marginal theorem [84]). *The joint distribution f and the marginals agree on the maximum value,*

$$\max_{\mathbf{x} \in \mathcal{X}} f(\mathbf{x}) = \max_{\mathbf{x}_{C_k} \in \mathcal{X}_{C_k}} \hat{f}_{C_k}(\mathbf{x}_{C_k}). \quad \forall k \in \mathcal{C} \quad (2.11)$$

This is a direct result of the definition of \hat{f}_{C_k} ,

$$\max_{\mathbf{x}_{C_k} \in \mathcal{X}_{C_k}} \hat{f}_{C_k}(\mathbf{x}_{C_k}) = \max_{\mathbf{x}_{C_k} \in \mathcal{X}_{C_k}} \left\{ \max_{\mathbf{z} \in \mathcal{X}} \{f(\mathbf{z}) : \mathbf{z}_{C_k} = \mathbf{x}_{C_k}\} \right\} = \max_{\mathbf{x} \in \mathcal{X}} f. \quad (2.12)$$

2.1.2.2 Maximizing assignment and traceback

To compute the maximizing assignment, \mathbf{x}^* , given the max-marginal potentials (eqn. 2.7) the algorithm starts at the root of \mathcal{T} , say C_i , and picks the assignment $\mathbf{x}_{C_i}^*$ that maximizes $\widehat{f}_{C_i}(\mathbf{x}_{C_i})$. It then propagates *simple max-flows* [84]. From thm. 2.1.1 we have that $\widehat{f}_{C_i}(\mathbf{x}_{C_i}^*) = \max_{\mathbf{x} \in \mathcal{X}} f(\mathbf{x})$. Next the algorithm takes an incident separator S_{ij} and assigns the variables $X_{S_{ij}}$ the corresponding values in $\mathbf{x}_{C_i}^*$ to get $\mathbf{x}_{S_{ij}}^*$. Because of max-consistency (eqn. 2.10) we have that $\widehat{f}_{S_{ij}}(\mathbf{x}_{S_{ij}}^*) = \max_{\mathbf{x} \in \mathcal{X}} f(\mathbf{x})$. The algorithm now moves to C_j and assigns values from $\mathbf{x}_{S_{ij}}^*$ to variables in X_{C_j} that coincide with $X_{S_{ij}}$. Then the algorithm finds the maximizing assignment, $\mathbf{x}_{C_j}^*$, to \widehat{f}_{C_j} over the remaining variables in C_j – such that $\widehat{f}_{C_j}(\mathbf{x}_{C_j}^*) = \max_{\mathbf{x} \in \mathcal{X}} f(\mathbf{x})$ due to max-consistency. The algorithm proceeds until it's processed the leaves of \mathcal{T} .

In a tree with m nodes there's $m - 1$ edges. Thus, given that $\widehat{f}_{C_i} = \max f$, for all $i \in \mathcal{C}$, and $\widehat{f}_{S_{ij}} = \max f$, for all $(i, j) \in \mathcal{S}$, then we are assured [84],

$$f(\mathbf{x}^*) = \frac{\prod_{i \in \mathcal{C}} \widehat{f}_{C_i}(\mathbf{x}_{C_i}^*)}{\prod_{(i,j) \in \mathcal{S}} \widehat{f}_{S_{ij}}(\mathbf{x}_{S_{ij}}^*)} = \frac{(\max_{\mathbf{x} \in \mathcal{X}} f(\mathbf{x}))^{|\mathcal{C}|}}{(\max_{\mathbf{x} \in \mathcal{X}} f(\mathbf{x}))^{|\mathcal{S}|}} = \max_{\mathbf{x} \in \mathcal{X}} f(\mathbf{x}). \quad (2.13)$$

2.1.2.3 Simplified max-flow propagation algorithm [84]

A rather simple but inefficient approach of producing M-BEST solutions uses Lawler's M-BEST algorithm of § 2.1.1. This algorithm is referred to as the simplified max-flow propagation algorithm or SMFP [84]. Assume the vector of random variable assignments $\mathbf{x}^{(1)} = (x_1^{(1)}, \dots, x_n^{(1)})$, represents the maximizing assignment to the joint probability distribution $f(\mathbf{x})$ on \mathcal{T} that we get after running the max-flow propagation algorithm of the previous section. In order to compute the next highest assignment SMFP partitions the space into n subsets that cover $\mathcal{X} \setminus \{\mathbf{x}^{(1)}\}$,

$$\begin{aligned} (P_1): & \{ \mathbf{x} \in \mathcal{X} : x_1 \neq x_1^{(1)} \} \\ & \vdots \quad \dots \\ (P_i): & \{ \mathbf{x} \in \mathcal{X} : x_1 = x_1^{(1)}, \dots, x_{i-1} = x_{i-1}^{(1)}, x_i \neq x_i^{(1)} \} \\ & \vdots \quad \dots \\ (P_n): & \{ \mathbf{x} \in \mathcal{X} : x_1 = x_1^{(1)}, \dots, x_{n-1} = x_{n-1}^{(1)}, x_n \neq x_n^{(1)} \} \end{aligned}$$

Note that each assignment space P_i constrains one of the variables to take on a different value than it did in $\mathbf{x}^{(1)}$, thereby removing $\mathbf{x}^{(1)}$ from the space of assignments. In

order to encode the constraints for an assignment space P_i , SMFP defines a series of functions as follows,

$$\bar{f}_i(\mathbf{x}) = \begin{cases} f(\mathbf{x}) & \text{if } x_1 = x_1^{(1)}, \dots, x_{i-1} = x_{i-1}^{(1)}, x_i \neq x_i^{(1)}, \\ 0 & \text{otherwise.} \end{cases} \quad (2.14)$$

Then it's easy to see that,

$$\max_{i \in [n]} \max_{\mathbf{x} \in \mathcal{X}} \bar{f}_i(\mathbf{x}) = \max_{\mathbf{x} \in \mathcal{X} \setminus \{x^{(1)}\}} f(\mathbf{x}). \quad (2.15)$$

To compute $\max_{\mathbf{x} \in \mathcal{X}} \bar{f}_i(\mathbf{x})$ (*i.e.* the maximum assignment to $f(\mathbf{x})$ constrained to P_i) a subset of variables are fixed,

$$X_1 = x_1^{(1)}, \dots, X_{i-1} = x_{i-1}^{(1)}, X_i \neq x_i^{(1)}, \quad (2.16)$$

by introducing the following representation that modifies the potential functions: given,

$$\delta_1(x_1; C) = \begin{cases} 1 & \text{if } (X_1 \in C \wedge x_1 = x_1^{(1)}) \text{ or } X_1 \notin C, \\ 0 & \text{otherwise} \end{cases} \quad (2.17)$$

\vdots

$$\delta_{i-1}(x_{i-1}; C) = \begin{cases} 1 & \text{if } (X_{i-1} \in C \wedge x_{i-1} = x_{i-1}^{(1)}) \text{ or } X_{i-1} \notin C, \\ 0 & \text{otherwise} \end{cases} \quad (2.18)$$

$$\delta_i(x_i; C) = \begin{cases} 1 & \text{if } (X_i \in C \wedge x_i \neq x_i^{(1)}) \text{ or } X_i \notin C, \\ 0 & \text{otherwise} \end{cases}, \quad (2.19)$$

SMFP modifies the clique and separator potentials as follows,

$$f_{C_k}(\mathbf{x}_{C_k}) = f_{C_k}(\mathbf{x}_{C_k}) \prod_{q=1}^i \delta_q(x_q; C_k) \quad (2.20)$$

Max-flows are then propagated in \mathcal{T} until equilibrium. Given the max-consistency property (eqn. 2.10) and thm. 2.1.1 the maximum of $\bar{f}_i(\mathbf{x})$ can be computed, and the corresponding maximizing assignment $\mathbf{x}^{(2)}$.

To find the third highest assignment to $f(\mathbf{x})$, the partitioning is as follows. If $\mathbf{x}^{(2)}$ belongs to subset P_i , then it is refined by partitioning it into the following subsets,

$$(P_{n+1}): \{x \in \mathcal{X} : x_1 = x_1^{(2)}, \dots, x_{i-1} = x_{i-1}^{(2)}, x_i \neq \{x_i^{(1)}, x_i^{(2)}\}\}$$

$$(P_{n+2}): \{x \in \mathcal{X} : x_1 = x_1^{(2)}, \dots, x_i = x_i^{(2)}, x_{i+1} \neq x_{i+1}^{(2)}\}$$

$\vdots \quad \dots$

$$(P_{2n-i+1}): \{x \in \mathcal{X} : x_1 = x_1^{(2)}, \dots, x_{n-1} = x_{n-1}^{(2)}, x_n \neq x_n^{(2)}\}.$$

Together with $\mathcal{P}^0 = \{P_1, \dots, P_n\} \setminus P_i$ the new partitioning $\mathcal{P}^1 = \{P_{n+1}, \dots, P_{2n+1-i}\}$ covers $\mathcal{X} \setminus \{\mathbf{x}^{(1)}, \mathbf{x}^{(2)}\}$. Repeating the above procedure for computing eqn. 2.15, $\mathbf{x}^{(3)}$ can be found. Continuing in this way SMFP finds the M-BEST solutions [84].

The down side of the approach is that many max-flow operations over \mathcal{T} have to be done in order to compute $\max_{i \in [n]} \max_{\mathbf{x} \in \mathcal{X}} \bar{f}_i(\mathbf{x})$ each round – a two-pass max flow propagation thru the entire tree for each assignment set.

Nilsson [84] also presents an alternate partitioning strategy that’s much more efficient which relies on the *running intersection property* of junction trees. This improved partitioning strategy allows for the max of f over partitions to be found with a single root to leaf propagation of max flows.

2.1.3 M-BEST solutions for loopy graphs and the BMMF algorithm

So far we have discussed M-BEST algorithms when exact inference is tractable. This included inference over general graphs with small tree-width that could be converted to junction trees in order to carry out exact inference. When the tree-width of the graph becomes large however inference over the junction tree becomes infeasible because the clique sizes are too large, so alternate M-BEST algorithms are needed.

Recall that when the graph is a tree (e.g. junction tree) exact inference can be carried out using the max-product message-passing algorithm we reviewed earlier. Also, recall from theorem 2.1.1 that the max-marginals and joint posterior distribution over the variables agree on the maximizing value. When the graph is a tree the max-marginals can be computed exactly and a traceback operation can be subsequently carried out to find the most probable variable assignments.

If we have a loopy graph, using the junction tree representation for inference becomes inefficient and approximate inference methods are needed for computing the *approximate* max-marginals over the graph. Moreover using traceback operation over the max-marginals on a loopy graph isn’t guaranteed to return the maximizing assignment (see [127] for an example). Independently picking the variable assignments that maximize each individual max-marginal will not work either because ties can exist in the max-marginal tables (i.e. max-marginal has more than one maximizing label for a variable) which means that theorem 2.1.1 will not hold (cf. [127]). Since ties can exist and traceback over a loopy graph will not work the alternative is to have multiple rounds of computing the max-marginals, where in each round additional tied variables are constrained to take on a single maximizing label. This process is continued until no more ties exist and we can get the maximizing assignment by independently maximizing over individual max-marginals.

Nilsson’s SMFP algorithm that we discussed in 2.1.2.3 is an example of an M-BEST algorithm that computes the max-marginals in a junction tree by using max-product message passing algorithm and subsequently uses the max-consistency property (eqn. 2.10) and thm. 2.1.1 to find the maximizing assignment. It needs $\mathcal{O}(Mn)$ computations of the max-marginals which is very expensive, where M is the number of M-BEST solutions and n is the number of variables in the graph.

The following algorithm by Yanover and Weiss [127] can find the M-BEST solutions in loopy-graphs with only $2M$ computations of max-marginals (M is the number of M-BEST solutions), and no trace-back operations (relying only on thm. 2.1.1).

Algorithm 3 Best Max-Marginal First (BMMF) algorithm for M-BEST solutions [127]

```

1:  $\text{SCORE}_1(i, j) \leftarrow \max_{\mathbf{x} : \mathbf{x}_i = j} f(\mathbf{x})$ 
2:  $\mathbf{x}_i^{(1)} \leftarrow \underset{j}{\operatorname{argmax}} \text{SCORE}_1(i, j)$ 
3:  $\text{CONSTRS}_1 \leftarrow \emptyset$ 
4:  $\text{USED}_2 \leftarrow \emptyset$ 
5: for  $m = 2, \dots, M$  do
6:    $\text{SEARCH}_m \leftarrow (i, j, k < m : \mathbf{x}_i^{(k)} \neq j, (i, j, k) \notin \text{USED}_m)$ 
7:    $(i_m, j_m, k_m) \leftarrow \underset{(i, j, k) \in \text{SEARCH}_m}{\operatorname{argmax}} \text{SCORE}_k(i, j)$ 
8:    $\text{CONSTRS}_m \leftarrow \text{CONSTRS}_{k_m} \cup \{\mathbf{x}_{i_m} = j_m\}$ 
9:    $\text{SCORE}_m(i, j) \leftarrow \max_{\mathbf{x} \mid \mathbf{x}_i = j, \text{CONSTRS}_m} f(\mathbf{x})$ 
10:   $\mathbf{x}_i^{(m)} \leftarrow \underset{j}{\operatorname{argmax}} \text{SCORE}_m(i, j)$ 
11:   $\text{USED}_{m+1} \leftarrow \text{USED}_m \cup \{(i_m, j_m, k_m)\}$ 
12:   $\text{CONSTRS}_{k_m} \leftarrow \text{CONSTRS}_{k_m} \cup \{\mathbf{x}_{i_m} \neq j_m\}$ 
13:   $\text{SCORE}_{k_m}(i, j) \leftarrow \max_{\mathbf{x} \mid \mathbf{x}_i = j, \text{CONSTRS}_{k_m}} f(\mathbf{x})$ 
14: end for
15: return  $\{\mathbf{x}^{(m)}\}_{m=1}^M$ 

```

In alg. 3 the joint probability over all variables of interest (e.g. posterior probability) is represented as $f(\mathbf{x})$. The algorithm start by inferring the max-marginals in line 1. In line 2 the maximizing MAP assignment is found using the max-marginal theorem. To compute the remaining $M - 1$ solutions the algorithm repeats the following operations: the max-marginal tables are searched to find the variable with next best max-marginal value, (cf. lines 6-7). The variable is fixed to the label corresponding to this value (i.e. $\mathbf{x}_{i_t} = j_t$) and added as a constraint for the next round of max-marginal computations (see cf. lines 8-9). Using th max-marginal theorem the next best solution is computed (see cf. line 10). The complementary constraint (i.e. $\mathbf{x}_{i_t} \neq j_t$) is added to the constraint set used to produce the max-marginals that gave the highest value earlier and the max-marginals are recomputed with this augmented set of constraints (cf. lines 12-13). In each iteration, t , a new set of max-marginals is added (i.e. $\text{SCORE}_t(i, j)$) that is the result of a running inference on the graph with some of the variables fixed. This fixing

of variables successively refines the partitioning of the assignment space in such a way that the previous best solutions are removed from consideration.

It turns out that for exact max-marginal computation, the assignment $\mathbf{x}^{(m)}$ produced by the BMMF algorithm 3 is the m -th most probable assignment under $f(\mathbf{x})$ (cf. [127]).

For loopy graphs where approximate inference algorithms have to be used for computing the max-marginals (e.g. loopy max-product belief propagation), the solutions produced by BMMF (so called loopy-BMMF) are not guaranteed to correspond to the M-BEST solutions but tend to be quite good in practice, compared to the top M assignments produced by Gibbs sampling.

2.1.4 M-BEST MAP and its linear programming formulation

We've seen that when computing MAP assignments is not tractable approximate methods can be used to compute the approximate M-BEST solutions. Yanover and Weiss' M-BEST MAP method (loopy-BMMF) [127], that we reviewed earlier, is one such method. The downside of approaches such as loopy max-product is that they do not provide bounds on the optimal values of the solutions. However, LP approximations to MAP do provide bounds on the optimal value and Fromer and Globerson [34] provide an extension of the LP MAP formulation to the M-BEST setting. This section provides an overview of their approach.

To start, recall from the review in chapter 1 that the MAP problem can be formulated as the following LP,

$$\max_{\mathbf{x}} f(\mathbf{x}) = \max_{\boldsymbol{\mu} \in \mathbb{M}(G)} \boldsymbol{\mu} \cdot \boldsymbol{\theta} \quad (2.21)$$

and that the maximizing $\boldsymbol{\mu}^{(*)}$ is integral and found at a vertex of $\mathbb{M}(G)$ — where $\mathbb{M}(G)$ is the marginal polytope defined in eqn. 1.60. Moreover, $\boldsymbol{\mu}^{(*)}$ corresponds to the MAP assignment $\mathbf{x}^{(1)}$. For general graphs representing $\mathbb{M}(G)$ requires an exponential number of inequalities so recall that the LP is relaxed by using an outer bound on $\mathbb{M}(G)$, called the local polytope (cf. eqn. 1.64), $\mathbb{L}(G)$ which can be represented by far fewer inequality constraints over the variables (i.e. half-spaces). As we mentioned in § 1.2, it has been shown that $\mathbb{M}(G) = \mathbb{L}(G)$ for tree structured graphs, so solving the LP-relaxation yields the exact MAP assignment.

2.1.5 M-BEST MAP LP when G is a tree

First consider tree-structured graphs. In order to extend the MAP LP formulation in eqn. 2.21 to the 2nd best MAP problem Fromer and Globerson [34] propose to swap $\mathbb{M}(G)$ for the following *assignment-excluding marginal polytope*,

$$\widehat{\mathbb{M}}(G, \mathbf{x}^{(1)}) = \{\boldsymbol{\mu} \mid \exists \mathbf{p}(\mathbf{x}) \in \mathcal{P} \text{ s.t. } \mathbf{p}(\mathbf{x}^{(1)}) = 0, \mathbf{p}(\mathbf{x}_s, \mathbf{x}_t) = \boldsymbol{\mu}_{st}(\mathbf{x}_s, \mathbf{x}_t), \mathbf{p}(\mathbf{x}_s) = \boldsymbol{\mu}_s(\mathbf{x}_s)\}, \quad (2.22)$$

where $\widehat{\mathbb{M}}(G, \mathbf{x}^{(1)})$ is the convex hull of a set of integral vectors corresponding to the different assignments, excluding only $\mathbf{x}^{(1)}$. They show that,

$$\max_{\mathbf{x} \neq \mathbf{x}^{(1)}} f(\mathbf{x}) = \max_{\boldsymbol{\mu} \in \widehat{\mathbb{M}}(G, \mathbf{x}^{(1)})} \boldsymbol{\mu} \cdot \boldsymbol{\theta}. \quad (2.23)$$

In order to represent $\widehat{\mathbb{M}}(G, \mathbf{x}^{(1)})$ as inequalities in the MAP LP, Fromer and Globerson propose the following: when G is a tree they show that adding the single inequality $I(\boldsymbol{\mu}, \mathbf{x}^{(1)}) \leq 0$ to $\mathbb{M}(G)$ will result in $\widehat{\mathbb{M}}(G, \mathbf{x}^{(1)})$, *i.e.*

$$\widehat{\mathbb{M}}(G, \mathbf{x}^{(1)}) = \{\boldsymbol{\mu} \mid \boldsymbol{\mu} \in \mathbb{M}(G), I(\boldsymbol{\mu}, \mathbf{x}^{(1)}) \leq 0\} \quad (2.24)$$

where,

$$I(\boldsymbol{\mu}, \mathbf{x}^{(1)}) = \sum_{s \in V} (1 - d_s) \boldsymbol{\mu}_s(\mathbf{x}_s^{(1)}) + \sum_{(s,t) \in E} \boldsymbol{\mu}_{st}(\mathbf{x}_s^{(1)}, \mathbf{x}_t^{(1)}), \quad (2.25)$$

and d_s is the degree of the nodes s in the tree (cf. [34]). They show that when G is a tree the polytope $\widehat{\mathbb{M}}(G, \mathbf{x}^{(1)})$ will remove only the integral solutions $\mathbf{x}^{(1)}$ and will not introduce fractional solutions. They point out that for general graphs however, adding $I(\boldsymbol{\mu}, \mathbf{x}^{(1)}) \leq 0$ to G removes some other integral vertices and may introduce fractional vertices.

2.1.6 M-BEST MAP LP when G is a general graph

Recall from chapter 1 that when G is a general graph the polytope of feasible solutions, $\mathbb{M}(G)$, for the MAP LP needs an exponential number of constraints, so the simpler outer-bound approximation, $\mathbb{L}(G)$ is used. Analogously, for the M-BEST MAP problem Fromer and Globerson [34] propose an outer-bound approximation to $\widehat{\mathbb{M}}(G, \mathbf{x}^{(1)})$. The approach they takes is to add inequalities to $\mathbb{L}(G)$ to separate $\mathbf{x}^{(1)}$ from the other integral vertices. Each new constraint also removes some fractional vertices. If enough such constraints are added then maybe only an intergral solution is left. The type of constraints they add are inequalities over *spanning trees* on the graph,

$$I^T(\boldsymbol{\mu}, \mathbf{x}^{(1)}) = \sum_{s \in V} (1 - d_s^T) \boldsymbol{\mu}_s(\mathbf{x}_s^{(1)}) + \sum_{(s,t) \in E} \boldsymbol{\mu}_{st}(\mathbf{x}_s^{(1)}, \mathbf{x}_t^{(1)}), \quad (2.26)$$

where d_s^T is the degree of node s in spanning-tree T . Analogous to when G is a tree (eqn. 2.24), for general graphs they propose an assignment-excluding marginal polytope that incorporates all spanning-tree inequalities of the graph,

$$\widehat{\mathbb{L}}^{ST}(G, \mathbf{x}^{(1)}) = \{\boldsymbol{\mu} \mid \boldsymbol{\mu} \in \mathbb{L}(G), \forall \text{ tree } T \subseteq E \quad I^T(\boldsymbol{\mu}, \mathbf{x}^{(1)}) \leq 0\}. \quad (2.27)$$

The 2nd best MAP LP for general graphs is thus,

$$\max_{\boldsymbol{\mu} \in \widehat{\mathbb{L}}^{ST}(G, \mathbf{x}^{(1)})} \boldsymbol{\mu} \cdot \boldsymbol{\theta}, \quad (2.28)$$

which is an approximation to solving over the feasible set $\widehat{\mathbb{M}}(G, \mathbf{x}^{(1)})$. They note that maximizing over $\widehat{\mathbb{M}}(G, \mathbf{x}^{(1)})$ is guaranteed to give an integral solution whereas maximizing over $\widehat{\mathbb{L}}^{ST}(G, \mathbf{x}^{(1)})$ does not.

The number of spanning trees over G is exponential in n but Fromer and Globerson use an efficient approach to consider all spanning trees. They first note that given $\boldsymbol{\mu}$ and spanning tree T , the quantity $I^T(\boldsymbol{\mu}, \mathbf{x}^{(1)})$ can be decompose over edges,

$$I^T(\boldsymbol{\mu}, \mathbf{x}^{(1)}) = \sum_{(s,t) \in E} (\boldsymbol{\mu}_{st}(\mathbf{x}_s^{(1)}, \mathbf{x}_t^{(1)}) - \boldsymbol{\mu}_s(\mathbf{x}_s^{(1)}) - \boldsymbol{\mu}_t(\mathbf{x}_t^{(1)})) + \sum_{s \in V} \boldsymbol{\mu}_s(\mathbf{x}_s^{(1)}), \quad (2.29)$$

therefore to find the tree that maximizes $I^T(\boldsymbol{\mu}, \mathbf{x}^{(1)})$ is equivalent to computing the max-weight spanning-tree over G where the edge weights are set to,

$$w_{st} = \boldsymbol{\mu}_{st}(\mathbf{x}_s^{(1)}, \mathbf{x}_t^{(1)}) - \boldsymbol{\mu}_s(\mathbf{x}_s^{(1)}) - \boldsymbol{\mu}_t(\mathbf{x}_t^{(1)}). \quad (2.30)$$

They then rely on existing efficient algorithms for computing the max-weight spanning-tree of a graph.

To solve the LP-relaxation in eqn. 2.28 they use a cutting-plane algorithm that adds the most violated constraint $I^T(\boldsymbol{\mu}, \mathbf{x}^{(1)}) > 0$ to the LP. Starting with any spanning-tree of G the most violated spanning-tree inequality for the current setting of $\boldsymbol{\mu}$ is found and added to the LP. This inequality removes $\boldsymbol{\mu}$ from the polytope of feasible solutions. The LP is solved again for a new setting of $\boldsymbol{\mu}$. The process continues until a non-fractional $\boldsymbol{\mu}$ is found or all the constraints are satisfied. If there are no violated constraints and $\boldsymbol{\mu}$ is still fractional Fromer and Globerson propose additional constraints that can be added but they note that typically only a few iterations of the cutting-plane algorithm are required to give integral solutions.

To extend the 2nd best MAP problem to the M-BEST MAP problem they propose an algorithm that recursively partitions the assignment space, similar to that of Nilsson [84] and Weiss [127] which we reviewed earlier. Their Partitioning for Enumerated Solutions (PES) algorithm is shown in alg. 4.

The most computationally expensive part of the algorithm is the inference on line 17. The LP's are solved using general LP solvers such as CPLEX [46]. When the M-BEST inference in line 17 is the LP-relaxation of eqn. 2.28, Fromer and Globerson refer to the algorithm as Spanning Tree Inequalities and Partitioning for Enumerated Solutions (STRIPES) [34].

Algorithm 4 PES Algorithm (cf. [34])

```

1: for  $m = 1, \dots, M$  do
2:   if  $m = 1$  then
3:      $\mathbf{x}^{(1)} \leftarrow \arg \max_{\mathbf{x}} f(\mathbf{x})$  ▷ MAP assignment
4:      $\text{CONSTRS}_1 \leftarrow \emptyset$ 
5:   else
6:      $k \leftarrow \underset{k \in \{1, \dots, m-1\}}{\text{argmax}} f(\mathbf{y}^{(k)})$  ▷ find assignment space containing highest valued assignment
7:      $\mathbf{x}^{(m)} \leftarrow \mathbf{y}^{(k)}$  ▷ next best assignment
8:      $(v, a) \leftarrow \text{any member of the set } \{(s, \mathbf{x}_s^{(m)}) \mid \mathbf{x}_s^{(m)} \neq \mathbf{x}_s^{(k)}\}$ 
9:      $\text{CONSTRS}_m \leftarrow \text{CONSTRS}_k \cup \{\mathbf{x}_v = a\}$  ▷ remove  $\mathbf{x}^{(k)}$  from assignment space  $m$ 
10:     $\text{CONSTRS}_k \leftarrow \text{CONSTRS}_k \cup \{\mathbf{x}_v \neq a\}$  ▷ remove  $\mathbf{x}^{(m)}$  from assignment space  $k$ 
11:     $\mathbf{y}^{(k)} \leftarrow \text{NextBestSolution}(\text{CONSTRS}_k, \mathbf{x}^{(k)})$ 
12:   end if
13:    $\mathbf{y}^{(m)} \leftarrow \text{NextBestSolution}(\text{CONSTRS}_m, \mathbf{x}^{(m)})$ 
14: end for
15: return  $\{\mathbf{x}^{(m)}\}_{m=1}^M$ 

16: procedure NextBestSolution(CONSTRS,  $\mathbf{x}^{(*)}$ )
17:   return  $\mathbf{y} \leftarrow \underset{\mathbf{x} \neq \mathbf{x}^{(*)}, \text{CONTRS}}{\text{argmax}} f(\mathbf{x})$ 
18: end procedure

```

2.2 DIVMBEST ALGORITHM

¹ M-BEST algorithms only constrain the m -th solution to be different than the previous $m - 1$ high probability solutions. For each of the previous solutions the current one needs to have a different value for at least one variable. While the set of M-BEST solutions is a more diverse set to pick from than the MAP assignment, the amount of diversity in the M-BEST set is not a parameter that can be adjusted and the minimum amount of diversity between solutions is not a-priori quantifiable. This is why applying M-BEST methods to discrete probabilistic models for image segmentation tend to produce M-BEST segmentations that are very similar to the MAP solution and each other. The number of possible segmentations for a typical image is $|\mathcal{L}|^n$, where n is the number of pixels (between tens of thousands to millions), and the number of labels per pixel, \mathcal{L} (two or more). The number of segmentations is exponential in n . If the discrete distributions over the space of assignments, that our probabilistic models learn, had spiky modes around very different solutions with nearly equal probability then the exact M-BEST solutions would indeed be diverse. Generally though the learned distributions contain modes that are smooth around neighborhoods of very similar

¹ The contributions to the thesis presented in this section are found in [7], and are in collaboration with Gregory Shakhnarovich and Dhruv Batra.

solutions giving them nearly equal probability, which results in M-BEST solutions that are very similar. Given that the space of segmentations is large, these neighborhoods around modes can contain a large number of very similar segmentations, each with nearly the same high probability. Having a set of segmentations that are very similar to one another and the MAP segmentation, both qualitatively and quantitatively, doesn't provide an advantage over choosing the MAP segmentation. Instead we want to produce a set of segmentations that meet certain criteria.

The key criteria of the set of segmentations produced with an M-BEST-like method include,

1. the set contains highly probable segmentations,
2. the segmentations are sufficiently different from one another and the MAP segmentation,
3. the set is as small as possible

The last property is important because we would like to reduce the assignment space to a set small enough on which more complex inference methods can be applied to pick a single high probability segmentation. This includes having a user in the loop to pick from the set. Clearly the first two properties are opposing — the more diverse the segmentations are the more likely that the set contains low probability ones, and inversely, higher probability segmentations tend to come from the same mode, hence are very similar.

The ideal set containing segmentations corresponding to the M-BEST-*modes* of the distribution learned by the probabilistic model satisfy the three properties above.

In this section we introduce an M-BEST-like approach that tries to ensure the above properties, called *DivMBEST*— in contrast to M-BEST MAP, the *DivMBEST* approach emphasizes diversity between solutions. We will show that the M-BEST MAP problem is a special case of the *DivMBEST* formulation.

To ensure that the set of segmentations contains sufficiently diverse segmentations the *DivMBEST* formulation incorporates a measure on dissimilarity between two segmentations. The formulation maximizes a linear combination of the probability of solution and dissimilarity to previous solutions. In fig. 2.1 and fig. 2.2 we illustrate, qualitatively, the differences between the MAP segmentation, and various alternate segmentations returned by M-BEST and *DivMBEST* methods, for two segmentation tasks.

Figure 2.1 provides evidence that a diverse set of highly probably segmentations under the learned model can contain significantly more accurate explanations of the image compared to the MAP assignment. Figure 2.2 compares segmentations corresponding to the MAP, 2nd best MAP, and 2nd best mode (second assignment of *DivMBEST*

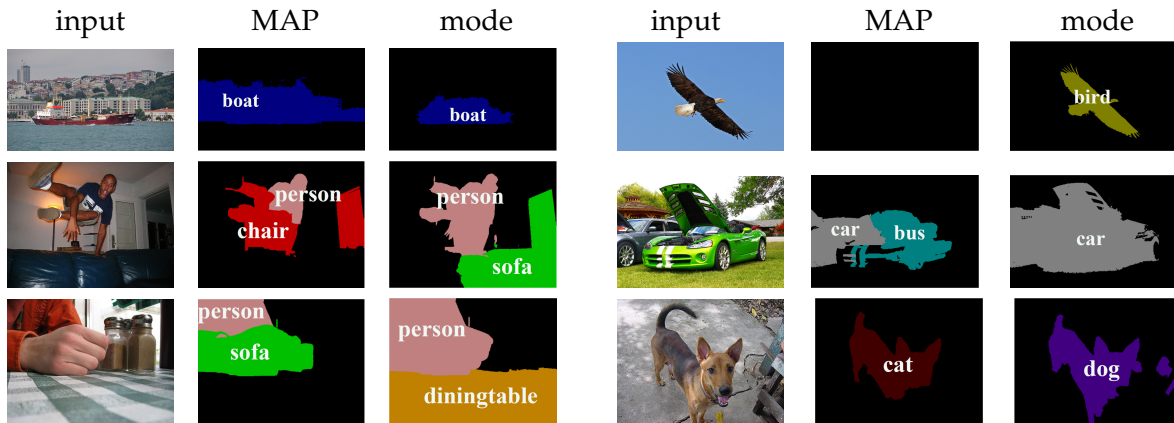


Figure 2.1: Semantic segmentations on test images from PASCAL VOC 2010. For each image, from left: input image, MAP segmentation, best out of 10 modes obtained with *DivMBEST*.

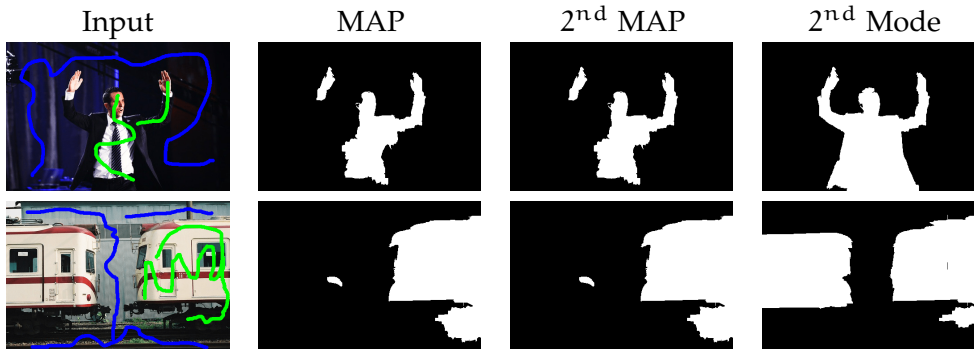


Figure 2.2: Interactive segmentations. For each image, from left: input image, MAP solution, 2nd best MAP, and the 2nd best mode obtained with *DivMBEST*.

algorithm) for an interactive segmentation task. The discrete probabilistic model is learned over bottom-up superpixels computed over the image. The 2nd best MAP segmentation is almost identical to the MAP estimate, and one must look closely to see the minor difference. In contrast, the 2nd best mode of the *DivMBEST* approach recovers a large portion of the object in one case and gives a drastically different explanation of the image in the other image. The advantage of using a *DivMBEST* approach to segmentation over M-BEST MAP is apparent from these examples.

2.2.1 Overview

This section presents the *DivMBEST* approach which is a generalization of the M-BEST MAP problem. It borrows a similar formulation as that of the M-BEST MAP integer

programming problem [34]. The *DivMBEST* problem has access to, and so assumes is available, a dissimilarity function, $\Delta(\cdot, \cdot)$, measuring the difference between two solutions. The Lagrangian relaxation of the *DivMBEST* integer program yields a problem that minimizes a linear combination of the energy and similarity to previous solutions. We conclude the section by presenting some nice properties of this linear programming relaxation of the original *DivMBEST* problem.

2.2.2 Contributions

The main contributions of the thesis in this section include,

- the first principled formulation for extracting a set of diverse highly probable solutions in discrete MRFs. The M-BEST MAP problem is a special case of this.
- For certain families of diversity functions between solutions, we show that the Lagrangian relaxation to the *DivMBEST* integer program is no more difficult to solve than the MAP problem. This makes it an attractive approach for inference because the same exact or provable approximate algorithms used to compute the MAP solution can be used to compute the *DivMBEST* solutions.

2.2.3 Notation

To refresh the notation we gave in Chapter 1, recall that we are given a set of discrete random variables $\mathbf{X} = \{X_s \mid s \in [n]\}$ (where $[n] \doteq 1, 2, \dots, n$), each takes a value from a finite set, $x_s \in \mathcal{X}_s$. Give a clique $C \subseteq [n]$, from a set of cliques $C \in \mathcal{C}$, let \mathbf{x}_C denote $\{x_s \mid s \in C\}$, and the label space \mathcal{X}_C be the cartesian product of the label spaces in the clique, $\times_{s \in C} \mathcal{X}_s$.

2.2.4 MAP problem

Let $G = (V, E)$ be a graph defined over the random variables \mathbf{X} , and $\theta_C : \mathcal{X}_C \rightarrow \mathbb{R}$ be functions defining the energy over cliques in the graph. Let $\mathcal{J}(C)$ be some index set over C and let $\mathcal{J} \doteq \cup_C \mathcal{J}(C)$ be the union over index sets of all cliques in the graph. The maximum a-posteriori (MAP) problem is to find the assignment $\mathbf{x} \in \mathcal{X}^n$ that minimizes the following energy function:

$$\min_{\mathbf{x} \in \mathcal{X}^n} \sum_{\alpha \in \mathcal{J}} \theta_\alpha(\mathbf{x}_\alpha) = \min_{\mathbf{x} \in \mathcal{X}^n} \sum_{s \in V} \theta_s(x_s) + \sum_{(s,t) \in E} \theta_{st}(x_s, x_t), \quad (2.31)$$

where we've restricted the cliques to be over nodes and edges of the graph for ease of exposition, but the method developed here apply to higher-order MRFs as well.

2.2.5 MAP integer program and its LP relaxation

Representing the energy in exponential form, the MAP problem can be written using the canonical overcomplete representation [118] where the node and edge energy functions can be defined as,

$$\theta_s(x_s) \doteq \sum_{j \in \mathcal{X}_s} \theta_{s;j} \mathbb{I}_{s;j}(x_s), \quad (2.32)$$

$$\theta_{st}(x_s, x_t) \doteq \sum_{(j,k) \in \mathcal{X}_s \times \mathcal{X}_t} \theta_{st;jk} \mathbb{I}_{st;jk}(x_s, x_t), \quad (2.33)$$

using the following node and edge potential functions,

$$\mathbb{I}_{s;j}(x_s) \doteq \begin{cases} 1 & \text{if } x_s = j, \\ 0 & \text{otherwise} \end{cases} \quad \forall s \in V, j \in \mathcal{X}_s, \quad (2.34)$$

$$\mathbb{I}_{st;jk}(x_s, x_t) \doteq \begin{cases} 1 & \text{if } x_s = j \text{ and } x_t = k, \\ 0 & \text{otherwise} \end{cases} \quad \forall (s,t) \in E, (j,k) \in \mathcal{X}_s \times \mathcal{X}_t, \quad (2.35)$$

yielding the re-written MAP inference problem,

$$\min_{x \in \mathcal{X}^n} \sum_{s \in V} \theta_s \cdot \mathbb{I}_s + \sum_{(s,t) \in E} \theta_{st} \cdot \mathbb{I}_{st} \quad (2.36)$$

where for each clique C we have the set of energies for all possible configurations of x_C , $\theta_C \doteq \{\theta_{C;\rho} \mid \rho \in \mathcal{X}_C\}$, and corresponding potential functions $\mathbb{I}_C \doteq \{\mathbb{I}_{C;\rho}(x_C) \mid \rho \in \mathcal{X}_C\}$.

Instead of minimizing over x we could alternatively assume that there are unknown variables μ such that the above MAP inference problem is equivalent to,

$$\min_{\mu_s, \mu_{st}} \sum_{s \in V} \theta_s \cdot \mu_s + \sum_{(s,t) \in E} \theta_{st} \cdot \mu_{st} \quad (2.37a)$$

$$\text{s.t.} \quad \sum_{j \in \mathcal{X}_s} \mu_{s;j}(x_s) = 1 \quad \forall s \in V, \quad (2.37b)$$

$$\sum_{(j,k) \in \mathcal{X}_s \times \mathcal{X}_t} \mu_{st;jk}(x_s, x_t) = 1 \quad \forall (s,t) \in E, \quad (2.37c)$$

$$\sum_{j \in \mathcal{X}_s} \mu_{st;jk}(x_s, x_t) = \mu_{t;k}(x_t) \quad \forall (s,t) \in E \quad \forall k \in \mathcal{X}_t, \quad (2.37d)$$

$$\sum_{k \in \mathcal{X}_t} \mu_{st;jk}(x_s, x_t) = \mu_{t;k}(x_s) \quad \forall (s,t) \in E \quad \forall j \in \mathcal{X}_s, \quad (2.37e)$$

$$\mu_{s;j}(x_s), \mu_{st;jk}(x_s, x_t) \in \{0, 1\} \quad (2.37f)$$

where the constraints enforce that each variable is assigned a single label and the assignments agree across edges. Note that when indicator variable $\mu_A(v)$ is set to 1, this corresponds to x_A taking label v . If we let $\mathcal{L}(G)$ denote the set of constraints in (2.37a)-(2.37e) then we can write eqn. 2.37 more concisely as,

$$\min_{\mu \in \mathcal{L}(G), \mu_A(x_A) \in \{0,1\}} \sum_{A \in V \cup E} \theta_A \cdot \mu_A. \quad (2.38)$$

The above integer program is equivalent to the MAP problem in eqn. 2.36, and is known to be NP-hard in general. We describe a Linear Programming relaxation of this problem in Chapter 1. A good review is also found in [123].

2.2.6 *DivMBEST: Formulation*

This section presents the *DivMBEST* formulation. The goal is to generate a diverse set of low-energy (high-probability) solutions. The approach is an iterative greedy algorithm — in each iteration we find the lowest energy solution that is at least some minimum dissimilarity from the previously generated solutions. To measure the dissimilarity between solutions the algorithm has access to a dissimilarity function $\Delta(\mu^{(1)}, \mu^{(2)})$ between two solutions. Suppose that we have already computed the MAP solution, which we denote as $\mu^{(1)}$. In order to compute the second best *mode* (we use the term *mode* loosely to mean low-energy diverse solutions) we propose to solve the following general problem,

$$\mu^{(2)} = \underset{\mu \in \mathcal{L}(G), \mu_A(x_A) \in \{0,1\}}{\operatorname{argmin}} \sum_{A \in V \cup U} \theta_A \cdot \mu_A \quad (2.39a)$$

$$\text{s.t. } \Delta(\mu, \mu^{(1)}) \geq k, \quad (2.39b)$$

which we call $2\text{MODES}(\Delta, k)$. The constraint in (2.39b) ensures that the next solution is at least k -units away from $\mu^{(1)}$ according to $\Delta(\cdot, \cdot)$. The choice of Δ and k are design choices which we'll describe in greater detail later.

Since *DivMBEST* is an iterative greedy approach we can extend the $2\text{MODES}(\Delta, k)$ problem to the $M\text{MODES}(\Delta, \mathbf{k})$ problem ($\mathbf{k} = \{k_i \mid i \in [m-1]\}$) in a straightforward manner by searching for the lowest energy solution that is k_m -units away from each of the previous $m-1$ solutions,

$$\mu^{(m)} = \underset{\mu \in \mathcal{L}(G), \mu_A(x_A) \in \{0,1\}}{\operatorname{argmin}} \sum_{A \in V \cup U} \theta_A \cdot \mu_A \quad (2.40a)$$

$$\text{s.t. } \Delta(\mu, \mu^{(1)}) \geq k_1, \quad (2.40b)$$

$$\Delta(\mu, \mu^{(2)}) \geq k_2, \quad (2.40c)$$

$$\vdots \quad (2.40d)$$

$$\Delta(\mu, \mu^{(m-1)}) \geq k_{m-1} \quad (2.40e)$$

2.2.7 DivMBEST: Lagrangian Relaxation and the Lagrangian dual function

Given the extra inequality constraints of (2.40b)-(2.40e) it's not clear how this problem relates to common MAP inference approximations to the MAP IP in eqn. 2.38. The Lagrangian relaxation of $\text{MMODES}(\Delta, \mathbf{k})$ that we get by *dualizing* the constraints can be written as,

$$f(\boldsymbol{\lambda}) = \min_{\boldsymbol{\mu} \in \mathcal{L}(\mathcal{G}), \boldsymbol{\mu}_A(\mathbf{x}_A) \in \{0,1\}} \sum_{A \in \mathcal{VUE}} \boldsymbol{\theta}_A \cdot \boldsymbol{\mu}_A - \sum_{i=1}^{m-1} \lambda_i (\Delta(\boldsymbol{\mu}, \boldsymbol{\mu}^{(i)}) - k_i), \quad (2.41)$$

where $\boldsymbol{\lambda}$ are the dual variables, also referred to as Lagrangian multipliers. The Lagrange dual, $f(\boldsymbol{\lambda})$, minimizes a linear combination of the solution energy and similarity to the previous solutions. The Lagrange multipliers, $\boldsymbol{\lambda}$, are non-negative and control the amount of penalty incurred for violating the minimum dissimilarity constraints. The following theorem holds for the Lagrange dual,

Proposition 2.2.1. *The Lagrangian dual function, $f(\boldsymbol{\lambda})$, is a piece-wise linear function that is concave in $\boldsymbol{\lambda}$ and is a lower-bound on the optimal value $\boldsymbol{\mu}^{(m)*}$ of the primal problem, $\text{MMODES}(\Delta, \mathbf{k})$, for all values of $\boldsymbol{\lambda} \geq 0$.*

Proof. The proof can be found in [11], and is reproduced here for completeness.

- (i) The Lagrange dual can be written in the following form, $f(\boldsymbol{\lambda}) = \min_{\boldsymbol{\mu}} \boldsymbol{a}_{\boldsymbol{\mu}} \cdot \boldsymbol{\lambda} + b_{\boldsymbol{\mu}}$, which shows that $f(\boldsymbol{\lambda})$ is a piece-wise linear function. Assume only two different values of $\boldsymbol{\mu}$, namely $\boldsymbol{\mu}_1$ and $\boldsymbol{\mu}_2$, and corresponding linear functions, $f_{\boldsymbol{\mu}_1}$ and $f_{\boldsymbol{\mu}_2}$, where $f_{\boldsymbol{\mu}_j} = \boldsymbol{a}_{\boldsymbol{\mu}_j} \cdot \boldsymbol{\lambda} + b_{\boldsymbol{\mu}_j}$. We can then write the pointwise minimum f as,

$$f(\boldsymbol{\lambda}) = \min\{f_{\boldsymbol{\mu}_1}(\boldsymbol{\lambda}), f_{\boldsymbol{\mu}_2}(\boldsymbol{\lambda})\} \quad (2.42)$$

Let $0 \leq \theta \leq 1$ and consider $\boldsymbol{\lambda}_1, \boldsymbol{\lambda}_2 \in \text{dom } f$. Then we have,

$$\begin{aligned} f(\theta\boldsymbol{\lambda}_1 + (1-\theta)\boldsymbol{\lambda}_2) &= \min\{f_{\boldsymbol{\mu}_1}(\theta\boldsymbol{\lambda}_1 + (1-\theta)\boldsymbol{\lambda}_2), f_{\boldsymbol{\mu}_2}(\theta\boldsymbol{\lambda}_1 + (1-\theta)\boldsymbol{\lambda}_2)\} \\ &= \min\{\theta f_{\boldsymbol{\mu}_1}(\boldsymbol{\lambda}_1) + (1-\theta)f_{\boldsymbol{\mu}_2}(\boldsymbol{\lambda}_2), \theta f_{\boldsymbol{\mu}_2}(\boldsymbol{\lambda}_1) + (1-\theta)f_{\boldsymbol{\mu}_2}(\boldsymbol{\lambda}_2)\} \\ &\geq \theta \min\{f_{\boldsymbol{\mu}_1}(\boldsymbol{\lambda}_1), f_{\boldsymbol{\mu}_2}(\boldsymbol{\lambda}_1)\} + (1-\theta) \min\{f_{\boldsymbol{\mu}_1}(\boldsymbol{\lambda}_2), f_{\boldsymbol{\mu}_2}(\boldsymbol{\lambda}_2)\} \\ &= \theta f(\boldsymbol{\lambda}_1) + (1-\theta)f(\boldsymbol{\lambda}_2), \end{aligned} \quad (2.43)$$

which shows that $f(\boldsymbol{\lambda})$ is concave in $\boldsymbol{\lambda}$. We can easily extend this to k functions $f_{\boldsymbol{\mu}_1}, \dots, f_{\boldsymbol{\mu}_k}$, for k finite to show the general result.

- (ii) To see that $f(\boldsymbol{\lambda})$ is a lower-bound on the optimal value $\boldsymbol{\mu}^{(m)*}$ of the primal problem, $\text{MMODES}(\Delta, \mathbf{k})$, consider a feasible point $\tilde{\boldsymbol{\mu}}$ of the primal problem. Then $\Delta(\tilde{\boldsymbol{\mu}}, \boldsymbol{\mu}^{(i)}) - k_m \geq 0$ for all $i \in [m-1]$. This gives,

$$L(\tilde{\boldsymbol{\mu}}, \boldsymbol{\lambda}) \leq \sum_{A \in \mathcal{VUE}} \boldsymbol{\theta}_A \cdot \tilde{\boldsymbol{\mu}}_A, \quad (2.44)$$

where $L(\boldsymbol{\mu}, \boldsymbol{\lambda})$ is the Lagrangian,

$$L(\boldsymbol{\mu}, \boldsymbol{\lambda}) = \sum_{A \in VUE} \boldsymbol{\theta}_A \cdot \boldsymbol{\mu}_A - \sum_{i=1}^{m-1} \lambda_i (\Delta(\boldsymbol{\mu}, \boldsymbol{\mu}^{(i)}) - k_i). \quad (2.45)$$

Therefore we have,

$$f(\boldsymbol{\lambda}) = \min_{\boldsymbol{\mu} \in \mathcal{L}(G), \boldsymbol{\mu}_A(x_a) \in \{0,1\}} L(\boldsymbol{\mu}, \boldsymbol{\lambda}) \leq L(\tilde{\boldsymbol{\mu}}, \boldsymbol{\lambda}) \leq \sum_{A \in VUE} \boldsymbol{\theta}_A \cdot \tilde{\boldsymbol{\mu}}_A. \quad (2.46)$$

Since $f(\boldsymbol{\lambda}) \leq \sum_{A \in VUE} \boldsymbol{\theta}_A \cdot \tilde{\boldsymbol{\mu}}_A$ holds for *all* feasible points $\tilde{\boldsymbol{\mu}}$ it also holds for $\boldsymbol{\mu}^{(m)*}$.

□

2.2.8 Diversity Functions

The *DivMBEST* formulation in eqn. 2.40 relies on defining a dissimilarity function $\Delta(\cdot, \cdot)$ between two solutions. It turns out that the *DivMBEST* formulation is general enough to include other methods as special cases, through the right choice of dissimilarity function. Below are two such cases.

2.2.8.1 0-1 dissimilarity and M-Best MAP

If we let $\Delta(\boldsymbol{\mu}, \boldsymbol{\mu}^{(i)}) = [[\boldsymbol{\mu} \neq \boldsymbol{\mu}^{(i)}]]$, where $[[\cdot]]$ is an indicator function which is 1 if the predicate is true and 0 otherwise, and set $k_i = 1$, such that the constraints in (2.40b)-(2.40e) are of the form $\Delta(\boldsymbol{\mu}, \boldsymbol{\mu}^{(i)}) \geq 1$ for $i \in [m-1]$, then we recover the M-Best MAP problem. These constraints force the m -th solution to be different from each of the previous $(m-1)$ solutions in at least one location.

2.2.8.2 Local dissimilarity and N-Best Maximal Decoding of Park and Ramanan

If we let $\Delta(\boldsymbol{\mu}, \boldsymbol{\mu}^{(i)}) = \max_{s \in V} \Delta_n(\boldsymbol{\mu}_s, \boldsymbol{\mu}_s^{(i)})$, where there's potentially a different dissimilarity function, Δ_n , defined for each node in V , and set $k_i = 1$, then we recover the N-Best maximal decoding of Park and Ramanan [88]. In terms of the local measure of dissimilarity, Δ_n , setting $k_i = 1$ forces the m -th solution to be different from each of the previous $(m-1)$ solutions at least one node.

Some dissimilarity functions can be decomposed according to the structure of the graph which provide some nice properties. A specific class of decomposable dissimilar-

ity functions that are used extensively in the experiments are dot-product dissimilarity functions.

2.2.8.3 Dot-product dissimilarity

If we let $\Delta(\boldsymbol{\mu}, \boldsymbol{\mu}^{(i)}) = -\sum_{s \in V} \boldsymbol{\mu}_s^T W \boldsymbol{\mu}_s^{(i)}$ and if the solution vectors, $\boldsymbol{\mu}$ and $\boldsymbol{\mu}^{(i)}$ are discrete, then $\Delta(\boldsymbol{\mu}, \boldsymbol{\mu}^{(i)})$ encodes the weighted Hamming distance between the two solutions, where the weights W capture the importance of various pairwise labellings across the two solutions. If $W = I$ (*i.e.* W is set to the identity matrix) then Δ is the straight-forward Hamming distance between the two solutions. It's interesting to see the form of the Lagrangian when Δ is the general dot-product dissimilarity between two solutions,

$$\begin{aligned} \sum_{A \in VUE} \boldsymbol{\theta}_A \cdot \boldsymbol{\mu}_A - \sum_{i=1}^{m-1} \lambda_i (\Delta(\boldsymbol{\mu}, \boldsymbol{\mu}^{(i)}) - k_i) = \\ \sum_{s \in V} \left(\boldsymbol{\theta}_s + \sum_{i=1}^{m-1} \lambda_i W \boldsymbol{\mu}_s^{(i)} \right) \cdot \boldsymbol{\mu}_s + \sum_{(s,t) \in E} \boldsymbol{\theta}_{st} \cdot \boldsymbol{\mu}_{st} + \sum_{i=1}^{m-1} \lambda_i k_i. \end{aligned} \quad (2.47)$$

Note that $f(\boldsymbol{\lambda})$ is now comprised of the three terms in eqn. 2.47 where the first two terms are simply the MAP problem of eqn. 2.38, with modified unary energies, and the last term is independent of $\boldsymbol{\mu}$. When $W = I$ there is a cost paid, proportional to λ_i , for setting local parts of the current solution, $\boldsymbol{\mu}_s$, equal to $\boldsymbol{\mu}_s^{(i)}$ of each of the previous $i \in [m-1]$ solutions. When W is non-identity the cost is spread over larger parts of the assignment.

Thus in the case where the Δ -function is a Hamming distance, since the first two terms of $f(\boldsymbol{\lambda})$ are the same as for the MAP problem, and the last term is independent of the minimization variables, we can compute $f(\boldsymbol{\lambda})$ using any MAP inference machinery (exact or approximate) that was used to compute the first solution $\boldsymbol{\mu}^{(1)}$. Moreover, the edge energies are left *unchanged* which means that certain classes of efficient MAP inference — such graph-cut algorithms that require submodular edge potentials — remain viable options for computing subsequent solutions.

2.2.8.4 Higher-order dissimilarity

Consider higher order dissimilarity functions of the form $\Delta(\boldsymbol{\mu}, \boldsymbol{\mu}^{(i)}) = \sum_{C \in \mathcal{J}} \Delta_C(\boldsymbol{\mu}_C, \boldsymbol{\mu}_C^{(i)})$, where C are subsets of variables, \mathcal{J} is an index set on subsets of variables, and $\Delta_C(\cdot, \cdot)$ has some structure allowing for efficient message passing. Unlike dot-product dissimilarity the higher-order dissimilarity does not decompose over nodes in the graph. Examples include cardinality potentials [111], pattern-based sparse higher order potentials [63, 95], and lower linear-envelope potentials [54]. We'll describe how efficient

inference on the Δ -augmented energy of the Lagrangian dual function can be performed in the next section.

2.2.9 Supergradient Ascent on Lagrangian dual function

As previously mentioned the Lagrangian relaxation, $f(\lambda)$, is a lower-bound on the value of the primal *DivMBEST* problem. We would like to find the λ^* such that $f(\lambda^*)$ provides the tightest lower bound on the value of the primal problem. If there is no duality gap between the primal and dual problem values then *strong duality* holds and solving the primal problem is equivalent to solving the Lagrangian dual relaxation. To find the tightest lower bound on the primal problem we need to solve the following *Lagrange dual problem*,

$$\max_{\lambda} f(\lambda) \tag{2.48a}$$

$$\text{s.t. } \lambda \geq 0 \tag{2.48b}$$

Recall that $f(\lambda)$ is a piece-wise linear function that is concave in λ (prop. 2.2.1). We can solve problem 2.48 using a projected *supergradient ascent* algorithm (alg. 5) on λ [105].

Algorithm 5 Projected Supergradient Ascent (cf. [105])

```

1:  $t \leftarrow 1$ 
2:  $\{\alpha_t \mid \alpha_t \geq 0, \lim_{t \rightarrow \infty} \alpha_t = 0, \sum_{t=0}^{\infty} \alpha_t = \infty\}$ . ▷ define sequence of step-sizes
3: Initialize  $\lambda^{(0)}$ 
4:  $f_{\text{best}}^{(0)} \leftarrow f(\lambda^{(0)})$ 
5: repeat
6:    $\lambda^{(t)} \leftarrow \lambda^{(t-1)} + \alpha_t \nabla f(\lambda^{(t-1)})$ 
7:    $\lambda^{(t)} \leftarrow [\lambda^{(t)}]_+$  ▷ project onto positive orthant
8:    $f_{\text{best}}^{(t)} \leftarrow \min\{f_{\text{best}}^{(t-1)}, f(\lambda^{(t)})\}$  ▷ keep track of best point found thus far
9:    $t \leftarrow t + 1$ 
10: until  $\lim_{t \rightarrow \infty} |f_{\text{best}}^{(t)} - f^*| \leq \epsilon$  ▷ stopping criteria

```

In alg. 5 the supergradient of f at $\lambda^{(t)}$ is denoted by $\nabla f(\lambda^{(t)})$. In order to guarantee convergence of the algorithm a convergent sequence of non-negative step-sizes, $\{\alpha_t\}$, has to be chosen such that $\lim_{t \rightarrow \infty} \alpha_t = 0$, and $\sum_{t=0}^{\infty} \alpha_t = \infty$ (e.g. $\alpha_t = \Gamma/\sqrt{t}$, where $\Gamma > 0$). In practice the stopping criteria on the last line of alg. 5 is such that if the value of $f_{\text{best}}^{(t)}$ does not improve the algorithm terminates.

Recall that $f(\lambda)$ is a point-wise minimum of a set of linear functions,

$$f(\lambda) = \min_{\mu} \mathbf{a}_{\mu} \cdot \lambda + b_{\mu}, \tag{2.49}$$

where the supergradient of f is $\nabla f(\lambda) = \mathbf{a}_{\hat{\mu}(\lambda)}$, with $\hat{\mu}(\lambda) \doteq \operatorname{argmin}_{\mu} \mathbf{a}_{\mu} \cdot \lambda + b_{\mu}$.

Proof. To see this consider the definition of the supergradient, namely g is a supergradient of a concave function f at $x \in \mathbf{dom} f$ if

$$f(y) \leq f(x) + g^\top(y - x), \quad \forall y \in \mathbf{dom} f. \quad (2.50)$$

Consider $f(\lambda')$, for some $\lambda' \in \mathbf{dom} f$, which equals $\mathbf{a}_{\hat{\mu}(\lambda')} \cdot \lambda' + b_{\hat{\mu}(\lambda')}$, where $\hat{\mu}(\lambda') \doteq \operatorname{argmin}_{\mu} \mathbf{a}_{\mu} \cdot \lambda' + b_{\mu}$, by definition. Clearly the following inequality holds for all λ ,

$$f(\lambda') = \mathbf{a}_{\hat{\mu}(\lambda')} \cdot \lambda' + b_{\hat{\mu}(\lambda')} \leq \mathbf{a}_{\hat{\mu}(\lambda)} \cdot \lambda' + b_{\hat{\mu}(\lambda)}. \quad (2.51)$$

We can add and subtract the quantity $\mathbf{a}_{\hat{\mu}(\lambda)} \cdot \lambda$ to the RHS to get,

$$f(\lambda') = \mathbf{a}_{\hat{\mu}(\lambda')} \cdot \lambda' + b_{\hat{\mu}(\lambda')} \leq \mathbf{a}_{\hat{\mu}(\lambda)} \cdot \lambda' + b_{\hat{\mu}(\lambda)} + \mathbf{a}_{\hat{\mu}(\lambda)} \cdot \lambda - \mathbf{a}_{\hat{\mu}(\lambda)} \cdot \lambda \quad (2.52)$$

$$= f(\lambda) + \mathbf{a}_{\hat{\mu}(\lambda)}(\lambda' - \lambda), \quad (2.53)$$

thus $\nabla f(\lambda) \doteq \mathbf{a}_{\hat{\mu}(\lambda)}$ is a supergradient of f at λ . \square

The supergradient of the Lagrangian dual function at λ is thus,

$$\nabla f(\lambda) = - \begin{bmatrix} \Delta(\hat{\mu}(\lambda), \mu^{(1)}) - k_1 \\ \vdots \\ \Delta(\hat{\mu}(\lambda), \mu^{(m-1)}) - k_{m-1} \end{bmatrix}, \quad (2.54)$$

where $\hat{\mu}(\lambda)$ is optimal solution to problem 2.41 for the current setting of λ . The supergradient has an intuitive meaning in relation to the projected supergradient descent algorithm presented in alg. 5. If at time t , a constraint is violated, say, $\Delta(\hat{\mu}(\lambda^{(t)}), \mu^{(i)}) - k_i < 0$, for some i — then the supergradient vector with respect to $\lambda^{(t)}$ will be positive at index i and the update in alg. 5-line 6 will increase the cost, $\lambda_i^{(t+1)}$, for violating the i -th constraint. Conversely, $\nabla f(\lambda)$ is negative for constraints that are satisfied, thus reducing the corresponding costs, $\lambda_j^{(t+1)}$, for violating those constraints (because the constraints are probably not active) and thus allowing for lower energy solutions.

One nice property is that in each iteration of alg. 5, the inference problem that is needed to be solved for $\lambda^{(t)}$ is very similar to that used to solve $\lambda^{(t-1)}$. Thus warm-starting the solver for $\lambda^{(t)}$ with the solutions $\lambda^{(t-1)}$ can be beneficial (e.g. re-using search trees in graph-cuts [57], or reusing messages in dual-decomposition).

2.2.10 How tight is the Lagrange relaxation?

² As mentioned earlier we'd like to find the tightest lower bound on the primal problem, MMODES. We gave a Lagrange relaxation of MMODES(Δ, \mathbf{k}), termed $f(\lambda)$ which

² Results in this section are due to Dhruv Batra [7]

we showed to be a lower bound on the value of $\text{MMODES}(\Delta, \mathbf{k})$ for all feasible \mathbf{u} , and all $\lambda \geq 0$. We now state the following result on the Lagrangian dual problem, $\max_{\lambda \geq 0} f(\lambda)$, which is the tightest lower bound on $\text{MMODES}(\Delta, \mathbf{k})$.

Theorem 2.2.1. (i) *The Lagrangian dual problem, $\max_{\lambda \geq 0} f(\lambda)$ is equivalent to solving the following relaxation of $\text{MMODES}(\Delta, \mathbf{k})$,*

$$\min_{\boldsymbol{\mu}} \quad \sum_{A \in \mathcal{VUE}} \boldsymbol{\theta}_A \cdot \boldsymbol{\mu}_A \quad (2.55a)$$

$$\text{s.t.} \quad \boldsymbol{\mu} \in \text{co}\{\boldsymbol{\mu}_A(\mathbf{x}_A) \in \{0, 1\} \mid \boldsymbol{\mu} \in \mathcal{L}(G)\} \quad (2.55b)$$

$$\Delta(\boldsymbol{\mu}, \boldsymbol{\mu}^{(i)}) \geq k_i \quad \forall i \in [m-1] \quad (2.55c)$$

where $\text{co}\{\cdot\}$ is the convex hull of a set of discrete solutions.

(ii) *Generally the Lagrangian relaxation is not guaranteed to be tight, but, for some dissimilarity functions $\Delta(\cdot, \cdot)$, the convex hull can be replaced with the discrete solutions $\boldsymbol{\mu}_A(\mathbf{x}_A) \in \{0, 1\}$, $\boldsymbol{\mu} \in \mathcal{L}(G)$ themselves resulting in a tight Lagrangian relaxation.*

Proof. (i) The result follows directly from the following equivalent LP-dual problems shown by Geoffrion [36],

$$\text{(dual)} \quad \max_{\lambda \geq 0} \min_{\mathbf{x} \geq 0} \mathbf{c}^T \mathbf{x} - \lambda^T (\mathbf{A}\mathbf{x} - \mathbf{b}) \quad (2.56a)$$

$$\text{s.t.} \quad \mathbf{B}\mathbf{x} \geq \mathbf{d} \quad (2.56b)$$

$$\mathbf{x}_j \in \mathbb{I}, j \in \mathcal{J}, \quad (2.56c)$$

and,

$$\text{(primal)} \quad \min_{\mathbf{x}} \mathbf{c}^T \mathbf{x} \quad (2.57a)$$

$$\text{s.t.} \quad \mathbf{A}\mathbf{x} \geq \mathbf{b} \quad (2.57b)$$

$$\mathbf{x} \in \text{co}\{\mathbf{x} \geq 0, \mathbf{B}\mathbf{x} \geq \mathbf{d}, \mathbf{x}_j \in \mathbb{I}, j \in \mathcal{J}\}, \quad (2.57c)$$

where \mathcal{J} is an index set over variables. Making appropriate substitutions gives the desired result.

(ii) Recall from Chapter 1 that $\mathbb{M}(G)$ is the set of realizable marginal distributions over graph G . Moreover in § 1.2 we mentioned the result that $\mathbb{M}(G)$ is the convex hull of the overcomplete representation defined in eqn. 2.34 and eqn. 2.35 over the finite index set in eqn. 1.43, where the indicator functions take on $\{0, 1\}$ values and are the extreme points of the polytope. Therefore $\mathbb{M}(G)$ is exactly $\text{co}\{\boldsymbol{\mu}_A(\mathbf{x}_A) \in \{0, 1\} \mid \boldsymbol{\mu} \in \mathcal{L}(G)\}$.

It's also a well known fact that minimizing a linear objective over a convex hull has the optimal solution at some extreme point of the convex hull, therefore it's equivalent to minimizing over the discrete solutions (which are the extreme

points). However, we also have the diversity constraints. The set of feasible solutions for problem 2.55 are those in the set,

$$P \doteq \left\{ \boldsymbol{\mu} \mid \Delta(\boldsymbol{\mu}, \boldsymbol{\mu}^{(i)}) \geq k_i \forall i \cap \text{co}\{\boldsymbol{\mu}_A(x_A) \in \{0, 1\} \mid \boldsymbol{\mu} \in \mathcal{L}(G)\} \right\}. \quad (2.58)$$

Therefore when P is a polytope with integral vertices we can remove $\text{co}\{\cdot\}$ from the constraints. Since $\text{co}\cdot$ has integral vertices we need to check whether $\Delta(\boldsymbol{\mu}, \boldsymbol{\mu}^{(i)}) \geq k_i$ introduce fractional vertices. When we have the M-Best MAP dissimilarity function, Fromer and Globerson [34] presented spanning-tree inequalities that are guaranteed not to introduce fractional vertices when G is a tree.

In general, though, when no assumption on $\Delta(\cdot, \cdot)$ are made, the Lagrangian relaxation is not guaranteed to be tight. Consider the dot-product (Hamming distance) dissimilarity, $\Delta(\boldsymbol{\mu}, \boldsymbol{\mu}^{(i)}) = -\sum_{s \in V} \boldsymbol{\mu}_s^T \boldsymbol{\mu}_s^{(i)}$. This dissimilarity introduces fractional vertices which was described as a counter-example by Fromer and Globerson [34],

Counter-example: Suppose we have a graph consisting of two nodes with an edge between them, and each node takes on two labels. Let the node energies be $\boldsymbol{\theta}_1 = \boldsymbol{\theta}_2 = (0, 0)$, and the edge energy be $\boldsymbol{\theta}_{12} = (0, 10, 10, 10)$. The MAP solution (minimizing solution over this graph) is $(0, 0)$. To find the second best solution — which is constrained to be different from the MAP solution with $k = 1$ — we introduce the constraint, $-\boldsymbol{\mu}_1(0) - \boldsymbol{\mu}_2(0) \geq -1 \implies \boldsymbol{\mu}_1(0) + \boldsymbol{\mu}_2(0) \leq 1$. The solution minimizing the energy over the graph with this new constraint is $(0.5, 0.5)$ with energy value 5, whereas the other non-MAP solutions have energy value 10. Since the solution is fractional the Lagrangian relaxation is not tight.

□

2.2.11 Computing Supergradient under different diversity functions

Recall that for certain diversity functions such as the Hamming distance dissimilarity functions we can compute $f(\boldsymbol{\lambda})$ using the same MAP inference machinery (exact or provably approximate) that was used to compute the first solution $\boldsymbol{\mu}^{(1)}$ because imposing the dissimilarity function between solutions amounts to only modifying the node energies but leaving the edge energies unaffected.

Not all dissimilarity functions share this decomposability property, especially when dissimilarity is measured between subsets of variables, which we term higher-order dissimilarity functions. However, there are some higher-order dissimilarity functions where the individual terms over subset of variables, $\Delta_C(\cdot, \cdot)$ (where C is a subset of variables), have some structure that can be exploited in order to carry on efficient inference over the Δ -augmented energy. Here we mention how for such Δ -augmented energies, where the higher-order dissimilarities contain specific structure, efficient en-

energy minimization can be performed via dual-decomposition based message-passing algorithms.

For simplicity of exposition, consider the Lagrangian relaxation to the 2MMODES problem,

$$\min_{\mu \in \mathcal{L}(G), \mu_A(x_A) \in \{0,1\}} \sum_{A \in VUE} \theta_A \cdot \mu_A - \bar{\lambda}_1 \Delta(\mu, \mu^{(1)}) - \bar{\lambda}_1 k_1. \quad (2.59)$$

and suppose $\Delta(\mu, \mu^{(1)})$ is a higher-order dissimilarity function that does not decompose according to nodes in the graph. Assume $\bar{\lambda}_1$ to be a *fixed* variable and let $\theta_{\text{hop}}^{(1)}(\mu) \doteq -\bar{\lambda}_1 \Delta(\mu, \mu^{(1)})$. Since $\bar{\lambda}_1 k_1$ is independent of μ the problem is reduced to,

$$\min_{\mu \in \mathcal{L}(G), \mu_A(x_A) \in \{0,1\}} \sum_{A \in VUE} \theta_A \cdot \mu_A + \theta_{\text{hop}}^{(1)}(\mu). \quad (2.60)$$

In contrast to dissimilarity functions that do decompose over nodes, even if the MAP problem (eqn. 2.38) could be solved efficiently, this Δ -augmented energy function is difficult to solve because of the higher order potential, $\theta_{\text{hop}}^{(1)}$. However, for certain higher-order potentials with structure where messages can be efficiently computed dual-decomposition based message-passing algorithms can be used to approximate the supergradient.

2.2.12 Dual-Decomposition and the approximate supergradient for higher order potentials

In order to minimize energy in problem 2.60 we apply the dual-decomposition approach [8, 38, 64]. We introduce auxiliary variables for each of the optimization variables, μ_s in problem 2.60 and write the following *equivalent* problem,

$$\min_{\mu, \mu^{\text{hop}}} \sum_{A \in VUE} \theta_A \cdot \mu_A + \theta_{\text{hop}}^{(1)}(\mu^{\text{hop}}) \quad (2.61a)$$

$$\text{s.t. } \mu \in \mathcal{L}(G) \quad (2.61b)$$

$$\mu_s^{\text{hop}} = \mu_s \quad \forall s \in V, \quad (2.61c)$$

$$\mu_A, \mu_A^{\text{hop}} \in \{0, 1\} \quad (2.61d)$$

where we are now minimizing over two sets of variables μ , and μ^{hop} which are constrained to agree. Introducing Lagrange multipliers ν_s for each constraint in line 2.61c, we can write the Lagrangian relaxation of problem 2.61 as,

$$g(\nu) = \min_{\mu, \mu^{\text{hop}}} \sum_{A \in VUE} \theta_A \cdot \mu_A + \theta_{\text{hop}}^{(1)}(\mu^{\text{hop}}) - \sum_{s \in V} \nu_s (\mu_s^{\text{hop}} - \mu_s) \quad (2.62a)$$

$$\text{s.t. } \mu \in \mathcal{L}(G) \quad (2.62b)$$

$$\mu_A, \mu_A^{\text{hop}} \in \{0, 1\} \quad (2.62c)$$

We can rewrite the above objective as a sum of two separate minimizations, one over the variables μ and the other over μ^{hop} ,

$$g(\mathbf{v}) = \min_{\mu \in \mathcal{L}(G), \mu_s, \mu_{st} \in \{0,1\}} \sum_{s \in V} (\theta_s + \mathbf{v}_s) \mu_s + \sum_{(s,t) \in E} \theta_{st} \mu_{st} \quad (2.63a)$$

$$+ \min_{\mu_{\Lambda}^{\text{hop}} \in \{0,1\}} \theta_{\text{hop}}^{(1)}(\mu^{\text{hop}}) - \sum_{s \in V} \mathbf{v}_s \mu_s^{\text{hop}} \quad (2.63b)$$

To find the tightest Lagrangian relaxation we want to maximize $g(\mathbf{v})$,

$$\max_{\mathbf{v} \in \mathbb{R}^n} g(\mathbf{v}) \quad (2.64)$$

which we can do using the supergradient method of alg. 5. The term in line 2.63a is the original MAP problem with perturbed unary potentials, so the minimization over μ can be carried out using the same efficient inference machinery used to compute the MAP solution. The term in line 2.63b is a minimization over $\mu_{\Lambda}^{\text{hop}}$ which is efficiently computable for higher order potentials that have structure such as cardinality potentials [39, 111], lower linear-envelope potentials [54] or sparse higher-order potentials [63, 95]. For example, in the case of cardinality potentials Gupta et al. [39] and Tarlow et al. [111] message-passing algorithms to compute them.

2.2.13 Setting k : the amount of diversity

The Lagrangian relaxation to the $\text{MMODES}(\Delta, \mathbf{k})$ problem provides a trade-off between minimizing the energy and the amount of diversity between solutions. Choosing the value k relates to the minimum amount of diversity we want between solutions. Choosing the right value for k is important because if the value of k is too small then the next solution might not be outside the energy valley of one of the previous solutions. On the other hand, too large a value for k could mean that several valid modes would be ignored. Also note that for each value of k there is a different value of λ that minimizes the Lagrangian relaxation, $\hat{\lambda}(\mathbf{k}) = \operatorname{argmin}_{\lambda(\mathbf{k}) \geq 0} f(\lambda(\mathbf{k}))$. This means that we would have to search for the optimal value of k , where for each value we'd have to run the supergradient ascent algorithm, which is expensive. Alternatively we can directly do grid search over values of λ . This is analogous to tuning the regularization parameter in learning. Since directly tuning λ is more efficient in practice, the amount of diversity is tuned in the experiments found in later chapters using cross-validation on λ , instead of directly searching over k .

2.2.14 Summary

To summarize, this chapter has presented the *DivMBEST* problem which finds a diverse set of highly probable solutions under a discrete probabilistic model. The *DivMBEST*

problem is a generalization of the M-best MAP problem. The *DivMBEST* problem is formulated as a Lagrangian relaxation of an integer linear program that involves solving the Δ -augmented energy minimization problem which minimizes a linear combination of the energy and similarity to previous solutions. For certain classes of Δ -function, the *modes* of the underlying distribution can be computed using the same inference algorithms that are used to compute the MAP solution.

The *DivMBEST* method provides an alternative approach to image segmentation — instead of devising complex models with higher-order terms that are hard to optimize over one can use simpler models in which exact or approximate MAP inference is tractable. With proper choice of Δ -function the same inference machinery can be used by the *DivMBEST* algorithm to obtain a set of diverse solutions. This small set of segmentations can then simply be evaluated by a more complex model in order to rank them. We introduce the ranking mechanism in chapter 3.

The *DivMBEST* approach is a greedy approximate strategy to finding a set of highly probable and yet diverse solutions under the model. In contrast Kirillov *et al.* [50] present the joint *DivMBEST* problem which simultaneously finds all M segmentations using an approximate solver that minimizes a single joint energy. In contrast to the *DivMBEST* formulation in this chapter their approach gives better quality results at the cost of significantly slower run time. For submodular energies Kirillov *et al.* [51] later propose an exact solver which is efficient albeit slower than the sequential approach. This is extended in [52], specific to binary submodular energies, to give a solver that is faster than the sequential approach presented in this chapter.

DIVMBEST+RERANK

There are many confounding factors that make semantic segmentation an inherently difficult task — from inter and intra object occlusion to lighting and varying appearance and pose. A segmentation algorithm will confront all these sources of uncertainty. However, devising fully probabilistic models that can incorporate all confounding factors in order to reason about the distribution over all possible segmentations jointly is usually intractable. This leads to two separate approaches to devising segmentation models. We can either build

1. *Restrictive Probabilistic Models* that can make efficient joint predictions over a posterior distribution of all variables of interest at the cost of limited prediction capacity due to simplifying independence assumptions, or
2. *Expressive Feed-Forward Models* that can incorporate more complex interaction of variables by using simple feed-forward predictions but propagate uncertainty by not modelling all the variables in a probabilistic joint-prediction framework.

Semantic segmentation models that fall into the first approach include Conditional Random Field (CRF) models such as [9, 60, 68]. To make joint prediction on all variables in a CRF tractable simplifying independence assumptions are usually made such as only local variable interactions that are associative or attractive [68]. The second approach includes feed-forward pipelines like [4, 15, 37] that find regions that are scored and then combined into a segmentation. The feed-forward approach can incorporate rich dependencies between regions that are difficult to capture in a tractable CRF, but errors propagate and accumulate in the pipeline.

This chapter introduces a two-stage hybrid approach called *DivMBEST+RERANK* that leverages both approaches. The first stage consists of a tractable probabilistic model that reasons about an exponentially large output state-space and makes joint predictions — but crucially outputs a diverse set of plausible segmentations not just a single one. The second stage of the approach is a discriminative re-ranker that is free to use arbitrarily complex features, and attempts to pick out the best segmentation from this set. Figure 3.1 gives an illustration of this approach.

DivMBEST+RERANK approach to semantic segmentation has several key advantages:

- *Global optimization over a simple model.* The first stage of this approach is able to perform global optimization over all the variables of interest, in a tractable

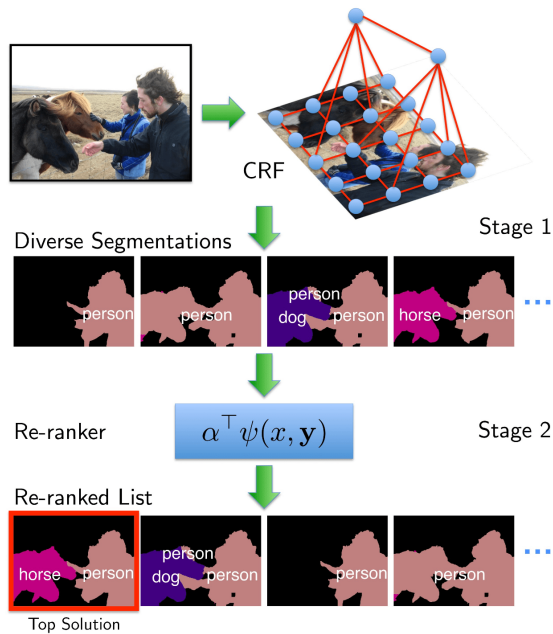


Figure 3.1: An overview of the *DivMBEST+RE-RANK* approach. In *Stage 1* diverse segmentations are computed from a tractable probabilistic model. These are fed to a large-margin re-ranker in *Stage 2*. The top re-ranked segmentation is returned as the final solution. Even though the most probable segmentation from *Stage 1* is incorrect, the set of segmentations does contain an accurate solution, which the re-ranker is able to score to the top.

albeit imperfect model to find a small set ($\approx 10 - 30$) of plausible hypotheses. Experimentally we find that typically at least one of these solutions is highly accurate.

- *Rich (higher-order) features in re-ranker.* Since the number of segmentations that the re-ranker needs to consider is small we do not have to worry about tractability issues when designing re-ranker features. The re-ranker is free to use arbitrarily complex features that would be intractable to add to the probabilistic model in the first stage. This is because the re-ranker does not need to *optimize* over all possible segmentations but merely *evaluate* these features on a small set of solutions.
- *Discrimination only within the set.* The re-ranker features need not be *globally* discriminative over all possible segmentations, rather only *locally* discriminative within the set returned by the first stage. Specifically, for the re-ranker the goal is not to identify generic good segmentations but use features that can help it discriminate good solutions from bad ones *within* a small set.

3.0.1 Contributions

The main contribution presented in this chapter is a discriminative re-ranking formulation for semantic segmentation. Our algorithm takes as input a set of labellings $\{\mathbf{y}^{(1)}, \dots, \mathbf{y}^{(m)}\}$ for an image and predicts the most accurate labelling from this list.

note the change of notation from $\mathbf{x}^{(i)}$ to $\mathbf{y}^{(i)}$.

The learning task is formulated as a Structured SVM (SSVM) [114], where the task loss penalizes the re-ranker for deviating from the most accurate solution in this set.

3.1 RELATED WORK

The *DivMBEST+ReRANK* approach to segmentation that is presented in this chapter is similar in spirit to the Constrained Parametric Min-Cuts (CPMC) approach of Carreira *et al.* [16], that was reviewed in § 1.1.1. CPMC produces a small set of high quality object segmentation proposals over an image that are scored according to how likely they are to be of an object. In the first stage of CPMC a large set of overlapping candidate figure-ground segmentation proposals are generated (using a bottom-up segmentation method) that are further pruned to remove redundant segmentations and finally ranked and culled in the second stage. The ranking is done by a regressor that is trained to map mid-level features, computed over the image and the figure-ground segment proposal, to the largest overlap the segment has with an object in the image (measured against ground-truth), quantifying the "objectness" of the proposal. Key to the approach is the concept of reducing the solution space (space of generated figure-ground regions) in the first stage. As opposed to building a model of object segmentation that includes both local and global interaction terms to capture the large scope of dependencies between regions in the image, the approach uses simple models in the first stage that incorporate only local interactions. This avoids the intractable nature of complex models with high-order terms and serves as a filter that reduces the state space to a much smaller set. The elements of this set have good alignment with image contours — a feature that can be captured using local interactions alone. In this restricted solution space the ranker in stage two can use features that capture more global properties that would potentially be intractable or at best inefficient to compute over the original exponential state space — global "objectness" features such as convexity and smoothness of region boundaries, eccentricity, and other gestalt features. An important property of the filtering stage is that it maintains high-recall, preserving high-quality segmentations, but reduces the state-space enough (*i.e.* reduces false-positive rates) so that higher-order processing is tractable on the remaining solutions.

Given that adjacent ranked segments tend to be very similar to each other a diversifying model is also incorporated in the second stage of [16] using Maximal Marginal Relevance (MMR) [14]. MMR is a sequential procedure — starting with the top-scoring segment the next segment is chosen by MMR that maximizes the original ranking score minus a score for having a redundant segment that is based on amount of overlap with the previously selected segments.

3.1.1 Relation to cascade approaches

Related to the *DivMBEST+ReRANK* approach are cascade models that consist of multiple stages of successively more complex inference models. Starting with a relatively simple model the stages progressively prune the output state-space in order to speed up inference and increase prediction accuracy. Cascade models accomplish this by leveraging the computational efficiency of simple models in the initial stages to filter out the majority of examples that are easy to discriminate. In further stages the cascades benefit from the predictive power of much more complex models, that though expensive to compute on the original state space, become tractable for a small set of solutions. The learnable model in each cascade stage is trained on the filtered output from the previous stage. Therefore negative examples that reach later stages (*i.e.* examples that pass the filtering of all the earlier stages) tend to be harder, and training the complex models in further stages to focus on discriminating these examples can lead to lower false-positive rates and improved performance. Key to any cascade approach is the balance between the following two criteria,

1. *Accuracy*: Minimize the number of errors made by each stage of the cascade to ensure accurate inference in subsequent models. This is so that the errors propagated to later stages is minimized.
2. *Efficiency*: Reduce the output state space of each stage so that inference in subsequent models can be done more efficiently.

This section reviews a number of relevant cascade models for vision tasks that are learned to balance these two criteria.

3.1.1.1 Face detection cascade

One of the early works to show effective use of cascade models was Viola and Jones' face detector [117]. There a classifier cascade consisting of multiple consecutive stages of simple to more complex classifiers is used to increase the efficiency of the detector (compared to using a single complex classifier) while simultaneously increasing the performance. Each classifier in the cascade takes as input features computed within a sub-window of the image, and predicts whether or not the sub-window contains a face. The dictionary of features can be very large and so too can the number of features computed within any sub-window. In each stage the classifier is a combination of a set of weak classifiers that has been trained using AdaBoost [32]. In [117] they restrict the weak learners to be classifiers that each depend on a single feature. Thus boosting amounts to a selection mechanism over the dictionary of features, retaining only the most informative features for classification.

Although using boosted classifiers itself reduces classification time compared to classifiers that depend on many more features the detection performance tends not to be as good. To improve on this Viola and Jones introduce the face detection cascade (*i.e.* classifier cascade) which is a simple approach to improve detection performance while giving low run-time complexity. The idea is to construct a cascade of progressively more complex classifiers, where complexity is in terms of number of features used by the classifier. The simpler classifiers at the early stages of the cascade are trained to detect all positive sub-windows while rejecting as many negative sub-windows as possible. In this way the early stage classifiers, that are more efficient to run, filter out the majority of the state space (the state space is all possible sub-windows in the image) so that the more complex classifiers in later stages, which are more computationally expensive, can focus on the task of classifying a much smaller set of sub-windows. The classifier in each stage of the cascade is trained with Adaboost, on training data constructed from sub-windows that have passed the previous stages. Since the sub-windows that pass earlier stages are harder to classify than the typical instance the classifiers further along the cascade have a more difficult task. As a result they give higher false-positive rate for a fixed value of recall (*i.e.* true-positive rate). To train the detector each stage in the cascade is trained by progressively increasing the number of features the classifier in a stage uses until the desired minimum false-positive rate and maximum true-positive rate are achieved on a held out set. To illustrate, Viola and Jones train a cascade with an initial stage consisting of a two feature classifier that remove 50% of the non-face sub-windows while retaining 99% of the sub-windows containing faces, at a 50% false-positive rate. The next stage classifier uses ten features and filters 80% of the non-face sub-windows while retaining 100% of the faces. Further stages use more and more features until the false-positive rate is virtually zero while maintaining a high true-positive rate. The result is a high performance face detector that is efficient to run at multiple-scales over the image.

3.1.1.2 Structured prediction cascades

The Structured Prediction Cascades of Weiss *et al.* [121, 122] provide a general framework for tractable and efficient MAP inference in structured output models (*e.g.* graphical models) with either high tree-width or large output state space. The idea is to reduce the state space by removing clique assignments that do not correspond to the MAP assignment. The Structured Prediction Cascade consists of sequential stages that take as input a set of possible assignments to cliques in the model and prune some of the clique assignments before passing the remaining to the next stage. Subsequent stages consist of increasingly more complex models. Model complexity can be achieved either by considering higher-order cliques, using more complex features, or starting with a coarsened state space and successively refining it in subsequent stages. In each stage pruning is done by running inference on the stage's model and identifying states that will be pruned. Pruning occurs based on the max-marginals of the

model. Recall that the max-marginal on a clique c of a model capturing some joint distribution $f(\cdot)$ (alternatively an energy or score) is defined as,

$$f^*(\mathbf{x}_c) \doteq \max_{\mathbf{x}' \in \mathcal{X}^n} \{f(\mathbf{x}') : \mathbf{x}'_c = \mathbf{x}_c\} \quad (3.1)$$

where \mathbf{x}_c is the portion of complete assignment \mathbf{x} that is associated with variables in clique c . The max-marginal is the maximum probability/score of any assignment that agrees on the clique assignment \mathbf{x}_c . The cascade stages filter out any clique assignment \mathbf{x}_c for which $f^*(\mathbf{x}_c) \leq t_\alpha$ for some tuned stage specific threshold t_α . Consider the score, $f(\mathbf{x})$, of a joint assignment \mathbf{x} . Note that if $f(\mathbf{x}) > f^*(\mathbf{x}'_c)$ then $\mathbf{x} \neq \mathbf{x}'_c$, which follows from the definition of $f^*(\mathbf{x}'_c)$. This implies a *safe filtering property* [122]: if $f(\mathbf{x}) > t_\alpha$ for some t_α , then for all \mathbf{x}_c , $f^*(\mathbf{x}_c) > t_\alpha$ (since $f^*(\mathbf{x}_c) \geq f(\mathbf{x}) > t_\alpha$). Therefore as long as $f(\mathbf{x}) > t_\alpha$ pruning clique assignments for which $f^*(\mathbf{x}_c) < t_\alpha$ will not remove the optimal clique assignments. Threshold t_α is defined as a convex combination of the MAP assignment score and the mean of the max-marginal score with combination weight α ($0 \leq \alpha \leq 1$), set to minimize the filtering error (number of correct clique states pruned by a stage). The threshold is similar to a quantile of the max-marginal values. Adjusting α is a trade-off between efficiency (*i.e.* aggressive pruning) and accuracy. Each stage is learned independently and sequentially using stochastic sub-gradient descent on the model parameters θ (recall $f(\mathbf{x}) = \langle \theta, \phi(\mathbf{x}) \rangle$) in order to minimize the filtering error. The threshold for each stage is set via cross-validation on α .

If inference over the models in each stage is intractable an ensemble method [122] is proposed that breaks the model into a collection of sub-models (*e.g.* graph reduced to sub-graphs collectively covering all nodes and edges) for which exact inference is tractable. A similar analysis to the case of a single model leads to an equivalent approach for filtering by thresholding the *sum* of max-marginals computed over the individual sub-models (cf. [122]), and analogous *joint safe filtering property*. Significant performance improvement on a number of vision tasks where the structured output has very high state-space, such as articulated pose estimation [101], show the performance benefits of the cascade approach.

3.1.2 Relation to proposal-generation methods

Similar to the *DivMBEST+RERANK* pipeline are a number of segmentation methods which produce an initial pool of segmentations of the image that are subsequently ranked according to how well they segment the objects in the scene. We mention a few noteworthy methods.

The category-independent object proposal and diverse ranking method of Endres *et al.* [27] that was review in § 1.1.1 produces a diverse set of object segmentations which align well with object boundaries. The final region proposal can be used to automatically localize object in the image for further processing for recognition, or can alterna-

tively be used to provide improved spatial support, compared to bounding boxes, for detection tasks.

Russell *et al.* [97] use a pool of global segmentations of images to learn object categories and their segmentations. Their approach can be viewed as a two-stage strategy of producing a diverse set of segments in the first stage followed by ranking the segments according to how well they match each of the discovered categories. More specifically, the approach (cf. [97]) uses the normalized-cut segmentation algorithm (cf. § 1.1.1) to produce a pool of candidate global segmentations of the image. For each segment in the pool of segmentations a histogram of visual words is computed. To concisely represent the segments a dictionary of visual words is constructed by computing SIFT [76] descriptors over the images of a held-out dataset which are clustered using k-means clustering. Each cluster center represent a visual word. Visual words can be used to represent an image or a region in an image. By using the dictionary to quantize the SIFT descriptors over an image into visual words a representation for a segment is built by computing the histogram of visual words contained in the segment. Given this *bag of visual words* representation for each segment statistical text analysis models are used to learn *topics* (*i.e.* object categories) from the pool of segments. A topic is thus a visual word histogram as well. Thus a segment can then be represented by a mixture of the discovered topics. For each of the discovered object categories the segments are subsequently ranked by how well a segment matches the visual word (KL-divergence between corresponding visual word histograms).

Another related approach is used to perform object segmentation with category-independent shape priors [49]. Multiple segmentations of an image are considered since an image might contain multiple objects, coupled with the fact that shape priors are imperfect so multiple competing hypotheses might exist. The shape priors are constructed by aggregating multiple learned category-independent shape priors. Each segmentation problem is initialized with one of the aggregated shape priors and a binary-labeling of the image is inferred (via graph-cut inference). Producing a pool of object segmentations increases the chance that at least one of the shape priors is useful in producing a high-quality object segmentation. Similar to CPMC (cf. § 1.1.1) classifiers can be trained to rank the object proposals.

3.1.3 Discriminative re-ranking in other domains.

Discriminative re-ranking of multiple solutions is also a common approach found in domains such as speech [22, 26] and natural language processing [21, 90, 103].

3.2 DIVMBEST + RE-RANK

¹ In § 2.2.6 we presented the *DivMBEST* algorithm for producing a diverse set of m highly probable segmentations from a discrete probabilistic graphical model, such as a CRF. Often we would like to return the single best segmentation of the image from this diverse set — that is we’d like an algorithm that can perform a 1-out-of- m inference task. This section presents a novel two-stage approach to ranking the diverse segmentations produced by the *DivMBEST* algorithm presented in chapter 1, called *DivMBEST+RE-RANK*. In the first stage a probabilistic model generates a set of diverse plausible segmentations. In the second stage, a discriminatively trained re-ranking model selects the best segmentation from this set. The re-ranking stage can use much more complex features than what could be tractably used in the probabilistic model, allowing a better exploration of the solution space than possible by simply producing the most probable solution from the probabilistic model.

3.2.1 Notation

In chapter 2 we denoted a segmentation (equivalently an assignment of labels to n (super)pixels or regions) by a vector \mathbf{x} where $\mathbf{x} = \{x_1, \dots, x_n\} \in \mathcal{X}^n$, $\mathcal{X}^n \doteq \times_{s \in [n]} \mathcal{X}_s$ — where \mathcal{X}_s is the set of labels for region s .

In this chapter we will make a change of variable for the assignment vectors. For the first stage (which produces *DivMBEST* candidate segmentations) let $\mathbf{y} = \{y_1, \dots, y_n\} \in \mathcal{Y}^n$ be a segmentation of the image, where the space of labellings is $\mathcal{Y}^n \doteq \times_{s \in [n]} \mathcal{Y}_s$, and \mathcal{Y}_s is the set of labels for region s . Recall the *DivMBEST* formulation for finding the m -th best diverse segmentation (*i.e.* MMODES problem),

$$\boldsymbol{\mu}^{(m)} = \underset{\boldsymbol{\mu} \in \mathbf{L}(\mathcal{G}), \boldsymbol{\mu}_A(\mathbf{y}_A) \in \{0,1\}}{\operatorname{argmin}} \sum_{A \in \mathbf{VUE}} \theta_A \cdot \boldsymbol{\mu}_A \quad (3.2a)$$

$$\text{s.t. } \Delta(\boldsymbol{\mu}, \boldsymbol{\mu}^{(i)}) \geq k_i \quad \forall i \in [m-1]. \quad (3.2b)$$

Note that the indicator vectors, $\boldsymbol{\mu}$, encode the label assignment to vectors \mathbf{y} , *i.e.* $(\boldsymbol{\mu}_j(\ell) = 1) \implies (\mathbf{y}_j = \ell)$. Therefore we can define a mapping $v : \{0,1\}^d \rightarrow \mathcal{Y}^n$ from d -dimensional indicator vector $\boldsymbol{\mu}$ to labelling \mathbf{y} : $\mathbf{y} = v(\boldsymbol{\mu})$. Given $\boldsymbol{\mu}^{(m)}$ the corresponding segmentation is $\mathbf{y}^{(m)} = v(\boldsymbol{\mu}^{(m)})$. Let $\mathbf{Y}_i = \{\mathbf{y}_i^{(1)}, \dots, \mathbf{y}_i^{(m)}\}$ denote the set of m diverse segmentations of the i -th image. At training time, the input to the second stage is a set of (image, ground-truth, segmentation-set) triples — $\{x_i, \mathbf{y}_i^{\text{gt}}, \mathbf{Y}_i \mid i \in [N]\}$, where x_i is the i -th image and \mathbf{y}_i^{gt} is the corresponding ground-truth segmentation. The quality of a segmentation is measured by a loss function, $\ell(\mathbf{y}_i^{\text{gt}}, \hat{\mathbf{y}})$, that returns the cost of predicting $\hat{\mathbf{y}}$ when the ground-truth is \mathbf{y}_i^{gt} .

¹ The contributions to the thesis presented in this section are found in [125], and are in collaboration with Gregory Shakhnarovich and Dhruv Batra.

Let $\mathbf{y}_i^{(*)}$ denote the most accurate segmentation in the set Y_i — that is,

$$\mathbf{y}_i^{(*)} = \operatorname{argmin}_{\mathbf{y} \in Y_i} \ell(\mathbf{y}_i^{\text{gt}}, \mathbf{y}). \quad (3.3)$$

The re-ranker uses features $\boldsymbol{\psi}(x, \mathbf{y}) : \mathbb{R}^{3 \times w \times h} \times \mathcal{Y}^n \rightarrow \mathbb{R}^p$ that are computed on the image x , and corresponding segmentation \mathbf{y} . The score of the re-ranker on segmentation \mathbf{y}_i of image x_i is denoted by,

$$S_r(\mathbf{y}_i) = \boldsymbol{\alpha}^\top \boldsymbol{\psi}(x_i, \mathbf{y}_i), \quad (3.4)$$

where $\boldsymbol{\alpha}$ are the p -dimensional re-ranker parameters.

3.2.2 Re-ranker model

As mentioned above the re-ranker is modelled as a linear combination of features, $\boldsymbol{\psi}(x, \mathbf{y})$ computed on the image x and corresponding segmentation \mathbf{y} , which assigns a score to each segmentation: $S_r(\mathbf{y}) = \boldsymbol{\alpha}^\top \boldsymbol{\psi}(x, \mathbf{y})$. Inferring the best segmentation under the re-ranker corresponds to computing the highest score,

$$\hat{\mathbf{y}}_i = \operatorname{argmax}_{\mathbf{y} \in Y_i} S_r(\mathbf{y}). \quad (3.5)$$

Re-scoring the segmentations using a ranker has a couple of benefits,

1. *Can use more complex features than segmentation model:* The re-ranker features $\boldsymbol{\psi}$ can be different from the features used in the model that generated the segmentations. In fact they can be quite complex and expensive to compute. The reason for this is that the re-ranker only needs to compute features on a relatively small set of candidate segmentations in contrast to the exponential number of segmentations that have been pruned by the first stage. Inference in the second stage is simply taking a dot product of the features with the re-ranker parameters $\boldsymbol{\alpha}$ and sorting the resulting scores. Hence we can afford to compute computationally expensive re-ranker features.
2. *Can incorporate features that are intractable to include in the segmentation model:* In the first stage the segmentation model can only compute features on the image or segmentation that are tractable. Incorporating higher-order interactions between regions into the model would result in potentials that could make inference over the model intractable. Hence incorporating performance limiting dependencies between variables are typically avoided in segmentation models. In contrast, the re-ranker features are a function of both the image x_i and segmentation \mathbf{y}_i . That means we can compute features like size of various categories, connectivity of the label masks, relative location of the label masks, and other such quantities that are functions of global statistics of the segmentation and thus intractable to include in the first stage.

3.2.3 Re-ranker loss

To train the re-ranker we need a measure of performance. Let $\mathcal{L}(\mathbf{y}_i^{\text{gt}}, \mathbf{y})$ be the re-ranker loss. Earlier we mentioned that the quality of a segmentation $\hat{\mathbf{y}}$ predicted by the re-ranker as being captured by the task loss $\ell(\mathbf{y}_i^{\text{gt}}, \hat{\mathbf{y}})$. Thus we could use the task loss as the re-ranker loss, *i.e.* $\mathcal{L}(\mathbf{y}_i^{\text{gt}}, \hat{\mathbf{y}}) \doteq \ell(\mathbf{y}_i^{\text{gt}}, \hat{\mathbf{y}})$. However, using $\ell(\mathbf{y}_i^{\text{gt}}, \hat{\mathbf{y}})$ has a drawback. Consider the following case: we are given two images i, j with two segmentations each, and corresponding accuracies $\text{Acc}(\mathbf{Y}_i) = \{95\%, 75\%\}$ and $\text{Acc}(\mathbf{Y}_j) = \{40\%, 35\%\}$. When the re-ranker loss is set to the task loss, for \mathbf{Y}_i we have that the loss on the two segmentations are $\{100 - 95\%, 100 - 75\%\} = \{5\%, 25\%\}$ whereas for \mathbf{Y}_j the re-ranker incurs much higher losses $\{100 - 40\%, 100 - 35\%\} = \{60\%, 65\%\}$. This means that the re-ranker will focus on picking the best segmentation in set j and ignore how well it does on set i . This is undesirable because set j segmentations are all of relatively the same (albeit poor) quality. Given that we are committed to the set, if the re-ranker makes a poor selection for the best segmentation in the set the cost incurred is only 5% compared to if the re-ranker had made the correct choice. On the other hand set i contains segmentations that are of very different qualities — the re-ranker will incur a 20% cost if it makes the wrong choice. Clearly it would be better for the re-ranker to focus attention on making the correct choice on set i instead of set j .

In order to shift the re-ranker to focus its effort on training instances where it is under performing relative to the set the following relative re-ranker loss is proposed,

$$\mathcal{L}(\mathbf{y}_i^{\text{gt}}, \hat{\mathbf{y}}_i) = \ell(\mathbf{y}_i^{\text{gt}}, \hat{\mathbf{y}}_i) - \ell(\mathbf{y}_i^{\text{gt}}, \mathbf{y}_i^{(*)}). \quad (3.6)$$

Using the relative loss in eqn. 3.6 gives losses: $\{5 - 5\%, 25 - 5\%\} = \{0\%, 20\%\}$ for set i and $\{60 - 60\%, 65 - 60\%\} = \{0\%, 5\%\}$ for set j — this shifts the focus to set i because an incorrect choice in that set is much costlier (difference of 20%) than an incorrect choice in set j (difference of 5%). Using the relative loss compared to the task loss was found empirically to play an important role in the performance of the re-ranker.

3.2.3.1 Re-ranker Training

Note that it is not necessary for the re-ranker to produce a scoring that induces a total ordering of the segmentations in set \mathbf{Y}_i . We only desire the re-ranker to assign the best segmentation in \mathbf{Y}_i a higher score than the other segmentations in the set, *i.e.* we desire $\text{Acc}(\hat{\mathbf{y}}) > \text{Acc}(\mathbf{y})$ for all $\mathbf{y} \in \mathbf{Y}_i \setminus \hat{\mathbf{y}}$, where $\hat{\mathbf{y}}$ is defined in eqn. 3.5. Thus we want to learn parsimonious re-ranker parameters α such that for image i ,

$$\alpha^\top \psi(x_i, \mathbf{y}_i^{(*)}) - \alpha^\top \psi(x_i, \mathbf{y}) > \gamma \quad \forall \mathbf{y} \in \mathbf{Y}_i \setminus \mathbf{y}_i^{(*)}, \quad (3.7)$$

where $\mathbf{y}_i^{(*)}$ is the best segmentation in the set \mathbf{Y}_i , and $\gamma \geq 0$ is some margin.

Then object in eqn. 3.7 coincides with the following quadratic program (QP),

$$\max_{\alpha \in \mathbb{R}} C \cdot \sum_{i \in [N]} \sum_{\mathbf{y} \in \mathbf{Y}_i \setminus \mathbf{y}_i^{(*)}} \left[\alpha^\top (\boldsymbol{\psi}(x_i, \mathbf{y}_i^{(*)}) - \boldsymbol{\psi}(x_i, \mathbf{y})) - \gamma \right] - \|\alpha\|_1, \quad (3.8)$$

where the first term encourages the best segmentations to be scored higher than the other segmentations for each image, and the ℓ_1 -penalty term is a regularization on α in order to reduce over-fitting on the training set by producing a parsimonious (*i.e.* sparse) representation of the features. The scalar value C balances the importance of the two terms. Introducing scalar *slack variables* for each image in the first term in the objective of problem 3.8 we can write it as,

$$\max_{\alpha, \xi_i} C \cdot \sum_{i \in [N]} \xi_i - \|\alpha\|_1 \quad (3.9a)$$

$$\text{s.t. } \alpha^\top (\boldsymbol{\psi}(x_i, \mathbf{y}_i^{(*)}) - \boldsymbol{\psi}(x_i, \mathbf{y})) \geq \gamma + \xi_i \quad \forall i \in [N], \forall \mathbf{y} \in \mathbf{Y}_i \setminus \mathbf{y}_i^{(*)}, \quad (3.9b)$$

$$\xi_i \geq 0 \quad \forall i \in [N]. \quad (3.9c)$$

Re-writing problem 3.9 as a minimization and replacing the ℓ_1 -loss (because it's not differentiable) with the ℓ_2 -loss we get,

$$\min_{\alpha, \xi_i} \frac{1}{2} \|\alpha\|_2^2 + C \cdot \sum_{i \in [N]} \xi_i \quad (3.10a)$$

$$\text{s.t. } \alpha^\top (\boldsymbol{\psi}(x_i, \mathbf{y}_i^{(*)}) - \boldsymbol{\psi}(x_i, \mathbf{y})) \geq \gamma - \xi_i \quad \forall i \in [N], \forall \mathbf{y} \in \mathbf{Y}_i \setminus \mathbf{y}_i^{(*)}, \quad (3.10b)$$

$$\xi_i \geq 0 \quad \forall i \in [N]. \quad (3.10c)$$

If we let $\gamma = 1$ (any choice of $\gamma \neq 0$ can be incorporated by the magnitude of α) and rescaling the slack variables by $\mathcal{L}(\mathbf{y}_i^{\text{gt}}, \mathbf{y})$ gives the familiar *Structured SVM QP* [48],

$$\min_{\alpha, \xi_i} \frac{1}{2} \|\alpha\|_2^2 + C \cdot \sum_{i \in [N]} \xi_i \quad (3.11a)$$

$$\text{s.t. } \alpha^\top (\boldsymbol{\psi}(x_i, \mathbf{y}_i^{(*)}) - \boldsymbol{\psi}(x_i, \mathbf{y})) \geq 1 - \frac{\xi_i}{\mathcal{L}(\mathbf{y}_i^{\text{gt}}, \mathbf{y})} \quad \forall i \in [N], \forall \mathbf{y} \in \mathbf{Y}_i \setminus \mathbf{y}_i^{(*)}, \quad (3.11b)$$

$$\xi_i \geq 0 \quad \forall i \in [N]. \quad (3.11c)$$

Intuitively we can see that constraint 3.11b tries to maximize the (soft)margin between the score of the oracle solution and all other solutions in the set. Importantly, the slack (or violation in the margin) is scaled by the loss of the solution. Thus if in addition to $\mathbf{y}_i^{(*)}$ there are other good solutions in the set, the margin for such solutions will not be tightly enforced. On the other hand, the margin between $\mathbf{y}_i^{(*)}$ and bad solutions will be very strictly enforced. We solve problem 3.11 via the 1-slack cutting-plane algorithm of Joachims [48] which we re-produce in alg 6 for reference. In each iteration the cutting-plane algorithm finds the segmentation that most violates the margin constraint on each image, *i.e.* lines 5- 7 of alg. 6 and add it to the working set (line 8). In the 1-slack

Algorithm 6 τ -slack cutting-plane algorithm for training Structural SVM with slack-rescaling [48]

1: Input: $D = \{(x_i, \mathbf{y}_i^{\text{gt}}, \mathbf{Y}_i) \mid i \in [N]\}$, C , ϵ

2: $\mathcal{W} \leftarrow \emptyset$

▷ initialize working set of constraints

3: **repeat**

4: $(\boldsymbol{\alpha}, \xi) \leftarrow \underset{\boldsymbol{\alpha}, \xi \geq 0}{\operatorname{argmin}} \frac{1}{2} \boldsymbol{\alpha}^\top \boldsymbol{\alpha} + C\xi$ (3.12a)

s.t. $\forall (\bar{\mathbf{y}}_1, \dots, \bar{\mathbf{y}}_N) \in \mathcal{W} :$ (3.12b)

$$\frac{1}{N} \boldsymbol{\alpha}^\top \sum_{i \in [N]} \mathcal{L}(\mathbf{y}_i^{\text{gt}}, \bar{\mathbf{y}}_i) (\boldsymbol{\psi}(x_i, \mathbf{y}_i^{(*)}) - \boldsymbol{\psi}(x_i, \bar{\mathbf{y}}_i)) \geq \frac{1}{N} \sum_{i \in [N]} \mathcal{L}(\mathbf{y}_i^{\text{gt}}, \bar{\mathbf{y}}_i) - \xi$$
(3.12c)

5: **for** $i = 1, \dots, N$ **do** ▷ find most violated constraints

6: $\hat{\mathbf{y}}_i \leftarrow \underset{\hat{\mathbf{y}} \in \mathbf{Y}_i}{\operatorname{argmax}} \left\{ \mathcal{L}(\mathbf{y}_i^{\text{gt}}, \hat{\mathbf{y}}_i) \left(1 - \boldsymbol{\alpha}^\top \left[\boldsymbol{\psi}(x_i, \mathbf{y}_i^{(*)}) - \boldsymbol{\psi}(x_i, \hat{\mathbf{y}}_i) \right] \right) \right\}$

7: **end for**

8: $\mathcal{W} \leftarrow \mathcal{W} \cup \{\hat{\mathbf{y}}_1, \dots, \hat{\mathbf{y}}_N\}$ ▷ add corresponding segmentations to constraint set

9: **until** $\frac{1}{N} \boldsymbol{\alpha}^\top \sum_{i \in [N]} \mathcal{L}(\mathbf{y}_i^{\text{gt}}, \bar{\mathbf{y}}_i) (\boldsymbol{\psi}(x_i, \mathbf{y}_i^{(*)}) - \boldsymbol{\psi}(x_i, \bar{\mathbf{y}}_i)) - \frac{1}{N} \sum_{i \in [N]} \mathcal{L}(\mathbf{y}_i^{\text{gt}}, \bar{\mathbf{y}}_i) \leq \xi + \epsilon$

10: **return** $(\boldsymbol{\alpha}, \xi)$

formulation we add a single constraint in each iteration (constraint 3.12c) consisting of the average loss re-weighted margin constraints. Notice that in problem 3.12 of line 4 in alg.6 there is a single slack variable ξ instead of an ξ_i for each image as in the original SSVM QP (*i.e.* problem 3.11).

At test time we compute stage-1 features Φ on an image and segmentation model potential functions θ_A , which we use to run the *DivMBEST* algorithm to produce a set of diverse segmentations \mathbf{Y} . We compute re-ranker features ψ on this set and score each segmentation using 3.4, returning the highest scoring solution (*i.e.* perform re-ranker inference in eqn. 3.5).

3.2.4 Summary

This chapter has presented a two-stage approach to segmentation: produce a set of diverse segmentations from a discrete probabilistic model, then re-rank them using a discriminative re-ranker formulated as a structural SVM. The re-ranking stage can use arbitrarily complex features, such as global features that are computed over the entire image or solution, in order to evaluate the best segmentation in the set. The first-stage filters the exponential space of possible segmentations to a small set of highly plausible solutions that are not merely minor perturbations of each other. The second-

stage can focus on the best-out-of- m inference task on a much reduced space, and thus only needs to compute features that are relevant in discrimination within the set. In chapter 5 we evaluate the performance of this approach on a number of semantic segmentation tasks.

DIVMBEST EXPERIMENTS

4.1 EVALUATING DIVMBEST SEGMENTATIONS

We look at a number segmentation tasks and investigate the quality of the *DivMBEST* segmentations against the MAP solution produced by the respective underlying segmentation models.

4.1.1 Baselines

We evaluate the *DivMBEST* segmentations against a number of baselines:

- **M-Best MAP** — The method of Yanover and Weiss [127] is used to produce a set of low energy (*i.e.* high probability) solutions, where the solutions are only constrained to be different on at least a *single* label assignment. There is no additional characterization of diversity between solutions.
- **Random** — Multiple solutions can be generated without any optimization as well. A new solution is created by taking a subset of the nodes in the MAP solution at *random* and changing their label assignment to the next best label according to the node min-marginals. Repeating this process produces a set of segmentations.
- **Confidence** — Similar to how the random segmentations were produced except the nodes are selected based on a *confidence* measure. A subset of the nodes with highest entropy (according to their min-marginals) are selected and their label set to the next best value.

For each solution μ of the *DivMBEST* algorithm, let $d(\mu, \mu^{(1)})$ denote the number of places that μ differs from the MAP solution $\mu^{(1)}$. In order to have a fair comparison between the perturbation based baselines and the *DivMBEST* solutions, for each solution μ produced by *DivMBEST* we generate a perturbation based solution that differs from the MAP solution in exactly $d(\mu, \mu^{(1)})$ locations. This ensures that the solutions generated using *random* or *confidence* perturbations have an equal measure of diversity compared to the *DivMBEST* solutions.

4.1.2 Oracle Solution

In order to evaluate the upper-bound on the quality of the segmentations in the *DivMBEST* set we can compute the *oracle* solution. Given a set of segmentations for the i^{th} image, $\{\mathbf{x}_i^{(1)}, \mathbf{x}_i^{(2)}, \dots, \mathbf{x}_i^{(m)}\}$, and corresponding ground-truth segmentation \mathbf{x}_i^{gt} , let the segmentation accuracy w.r.t ground-truth be denoted as $\text{Acc}(\mathbf{x}_i^{(k)}, \mathbf{x}_i^{\text{gt}})$ ¹. The *oracle* segmentation, $\mathbf{x}_i^{(*)}$, is defined to be the segmentation *within the set* that achieves maximum segmentation accuracy, *i.e.*,

$$\mathbf{x}_i^{(*)} = \underset{\mathbf{x}_i \in \{\mathbf{x}_i^{(1)}, \dots, \mathbf{x}_i^{(m)}\}}{\text{argmin}} \quad \text{Acc}(\mathbf{x}_i, \mathbf{y}_i). \quad (4.1)$$

¹ $\text{Acc}(\cdot, \cdot)$ can be intersection-over-union score between two segmentations or any relevant measure on accuracy of a predicted segmentation with respect to ground-truth.

4.2 INTERACTIVE SEGMENTATION

¹ Recall from § 1.1 that in interactive segmentation the user is interested in cutting out the foreground object from the rest of the image via annotations like scribbles [12] or bounding boxes [93]. The problem is typically formulated as a figure-ground segmentation task where some model variables are fixed according to the user annotations. In each round the MAP solution is computed and presented to the user, at which point the user provides additional supervision and the MAP solution is updated. This process is repeated until the MAP solution is acceptable. Instead of showing a single cutout each round the number of user interactions could be minimized by having the interface show a set of possible cutouts for the user to pick from. Ideally we'd like an algorithm that can *efficiently* produce a *small* set of *diverse* solutions.

4.2.1 CRF Model

Consider the image-scribble pair (X, \mathcal{S}) , where each image is a collection of n superpixels $X \doteq \{X_s \mid s \in [n]\}$. Let $\mathbf{x} = \{x_s \mid s \in [n]\}$ be a corresponding label assignment to all the superpixels in the image, where each superpixel takes on either foreground or background label, *i.e.* $x_s \in \{\text{fg}, \text{bg}\}$. A subset $\mathcal{S} \subset [n]$ of the superpixels have known label according to the scribbles, *i.e.* the superpixel labels $\{x_s \mid s \in \mathcal{S}\}$ are assigned according to the manually provided scribbles. Alternatively pixels could have been used but superpixels were preferred for computational efficiency reasons, and better alignment of segmentations to internal image boundaries. We chose the SLIC algorithm [1] to generate superpixels, with the desired number of superpixels in an image set to

¹ The contributions to the thesis presented in this section are found in [7], and are in collaboration with Gregory Shakhnarovich and Dhruv Batra.

Features
Color [44] C1: RGB mean values C2: C1 in HSV colorspace C3: Hue histogram and entropy C4: Saturation histogram and entropy
Texture T1: Histogram of gradients (HOG) [24]
Local L1: Histogram of SIFT [76] codewords

Table 4.1: Superpixel features used to learn the appearance model for the interactive segmentation figure-ground cutout model.

3000. The average image in our dataset contains $\simeq 150\text{K} - 200\text{K}$ pixels. To model the figure-ground segmentation problem we build a graph $G = (V, E)$ over the superpixels and define a pairwise CRF with the following energy,

$$E(\mathbf{x}; \mathcal{A}) \doteq \sum_{s \in V} \left[\theta_s(x_s; \mathcal{A}) + \lambda \cdot \sum_{t \in \mathcal{N}(s)} \theta_{st}(x_s, x_t) \right], \quad (4.2)$$

where $\mathcal{N}(s)$ are the superpixels adjacent to superpixel s in the image. The *data term* is the cost of assigning a superpixel to foreground or background, and it depends on the appearance model \mathcal{A} that's learned from the user scribbles \mathcal{S} . The pairwise *smoothness term* penalizes neighboring superpixels being assigned different labels.

4.2.1.1 Data term

The data term depends on an appearance model \mathcal{A} that is based on the output of a *Transductive SVM* (TSVM). The appearance model is learned by extracting features $\phi(X_s)$ from labelled and unlabelled superpixels and training a TSVM [109] to predict if a superpixel belongs to foreground or background. The features include the low level color, texture, and local cues listed in table 4.1. Let the superpixel *score* for belonging to foreground be $\text{score}(X_s) = \mathbf{w}^T \phi(X_s)$, where \mathbf{w} is the learnt weight vector of the TSVM. We define the foreground data term energy as,

$$\theta(x_s = \text{fg}) \doteq \begin{cases} \eta & \text{if } \text{score}(X_s) \geq 0, \\ \eta - 1 & \text{otherwise} \end{cases} \quad (4.3)$$

where $\eta = 0.5e^{\frac{-|\text{score}(X_s)|^2}{\alpha\sigma^2}}$, $\sigma^2 = \text{Var}(\{\text{score}(X_s) \mid s \in \mathcal{S}\})$, and α is a constant that is set via cross-validation on a held out set that is kept the same for all images. The background energy is then simply,

$$\theta(x_s = \text{bg}) \doteq 1 - \theta_s(x_s = \text{fg}). \quad (4.4)$$

4.2.1.2 Smoothness term

The smoothness term is a contrast sensitive Potts energy [12] that penalizes adjacent labels taking different labels. The penalty is proportional to how similar the two superpixels are in feature space. The more similar the features are the more penalty is paid,

$$\theta_{st}(x_s, x_t) \doteq \delta_{x_s \neq x_t} \cdot \beta_1 \cdot e^{-\beta_2 d_{st}} \quad (4.5)$$

where d_{st} is the distance between the feature vectors of superpixels s and t , and the scale parameters are set to, $\beta_1 = 2$, $\beta_2 = \sqrt{\frac{\max\{d_{st}\}}{20}}$.

4.2.1.3 Inference

The figure-ground interactive segmentation problem amounts to finding the assignment to unlabelled superpixels that minimizes the energy in eqn. 4.2. Note that this is a binary (*i.e.* two-label) contrast sensitive Potts model with submodular pairwise energy terms, for which efficient graph-cut algorithms exist to compute the *exact* MAP solution in polynomial time [13, 57].

4.2.1.4 Data + training

To evaluate the interactive segmentation model, and its *DivMBEST* extension described next, evaluation was performed on 100 images from Pascal VOC2010. For each image scribbles marking foreground objects and background regions were manually provided. Fifty of the images were used for tuning the parameters and the rest were used for reporting test accuracy. The weight on the smoothness term (λ) was tuned by doing grid search in the range [0, 1]. The best setting on training images was achieved with $\lambda = .18$, and used on the test set experiments.

4.2.2 Interactive segmentation + *DivMBEST*

Using the *DivMBEST* framework the underlying interactive segmentation model can be extended to generate a set of plausible segmentations each round, instead of just a

single MAP solution. The *DivMBEST* formulation will encourage high quality segmentations under the model that are diverse. Experimental results are provided for the dissimilarity functions described below.

4.2.2.1 Hamming dissimilarity

The negative dot-product distance function $\Delta(\boldsymbol{\mu}, \boldsymbol{\mu}^{(i)}) \doteq - \sum_{s \in V} \boldsymbol{\mu}_s^\top \boldsymbol{\mu}_s^{(i)}$ captures the Hamming dissimilarity between two solutions (see § 2.2.7). Recall that since the dot-product function decomposes over nodes in the graph, the *DivMBEST* formulation under Hamming dissimilarity is equivalent to a Δ -augmented energy minimization problem were the unary terms in the energy have been perturbed in a certain way (cf. § 2.2.7). The pairwise interaction terms remain unaffected, so if the smoothness term is submodular in the original problem then it remains submodular. This means that the m-modes can be computed using the same efficient inference algorithm used to compute the MAP solution. In the case of our binary pairwise energy in eqn. 4.2, we can compute the m-modes using the same efficient graph-cuts algorithm that was used to optimally compute the MAP solution.

4.2.2.2 Higher-order potential (HOP) dissimilarity

Let $\#\boldsymbol{\mu} \doteq \sum_{s \in V} \boldsymbol{\mu}_s(1)$ denote the number of nodes in the solution that are set to the foreground label. The value $\#\boldsymbol{\mu}$ represents the size of the foreground region. The HOP dissimilarity is defined as,

$$\Delta(\boldsymbol{\mu}, \boldsymbol{\mu}^{(1)}) = \begin{cases} (\#\boldsymbol{\mu} - \#\boldsymbol{\mu}^{(1)})^2 & \text{if } \#\boldsymbol{\mu} \geq \#\boldsymbol{\mu}^{(1)}, \\ 0 & \text{otherwise} \end{cases} \quad (4.6)$$

Intuitively the HOP dissimilarity is zero if the foreground size of the current segmentation is smaller than the foreground size of the MAP solution. Otherwise the dissimilarity grows quadratically. Since the *2MODES* constraint on the MAP solution is $\Delta(\boldsymbol{\mu}, \boldsymbol{\mu}^{(1)}) \geq k$, for some $k > 0$, the HOP dissimilarity encourages foreground size of the current solution to be larger than the MAP. By changing the sign on Δ we can alternatively encourage smaller solutions. Note that $\#\boldsymbol{\mu}$ is a global measure of the solution so it cannot be decomposed over subsets of variables. However, the Δ -augmented energy minimization problem that we get from the Lagrange relaxation of the *DivMBEST* problem, under HOP dissimilarity, results in a *cardinality potential* [39, 111] for which efficient approximate solutions exist. To solve this Δ -augmented energy minimization problem we can use the HOPMAP algorithm of Tarlow *et al.* [111].

Figure 4.1 shows a few *DivMBEST modes* using HOP dissimilarity on the interactive segmentation problem.

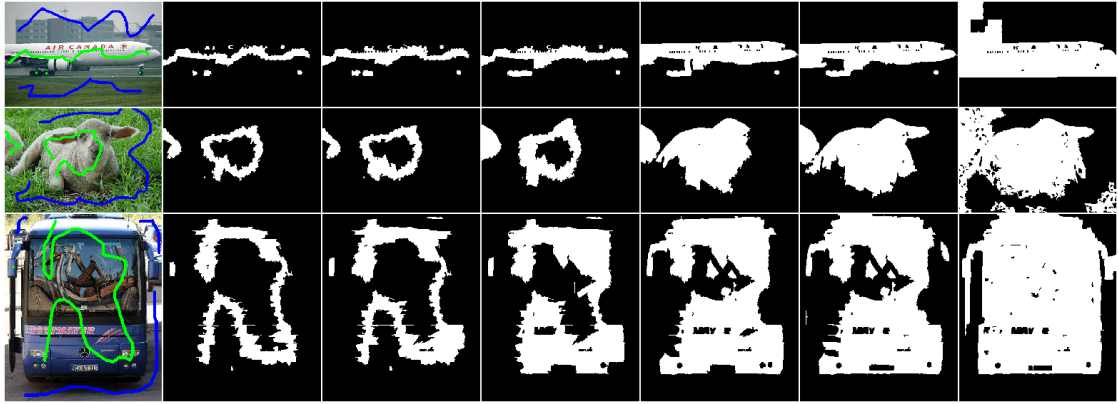


Figure 4.1: *DivMBEST* modes under cardinality-based HOP. From left-to-right: image-scribble pair (X, S) , MAP solution, 2nd-mode, ..., 6th-mode. The modes are ordered in increasing size of foreground object.

4.2.3 Experiments

In this section we evaluate the quality of the object cutouts generated in the first round of interactive segmentation. Specifically we compare the MAP segmentation against the alternative approach of generating a set of *DivMBEST* solutions. We also evaluate some other baseline approaches, which we describe next.

4.2.3.1 Baselines

Since eqn. 4.2 is a binary contrast sensitive Potts energy [12] that is submodular its exact MAP solution can be computed using the graph-cut implementation of [62]. The *DivMBEST* solutions under the Hamming dissimilarity can also be computed using the same graph-cut implementation. We also evaluate the *DivMBEST* solutions under HOP dissimilarity generated using HOPMAP [111].

The first baseline is the M -best MAP algorithm [127] which we reviewed in § 2.1.3. We also compare against the *random* and *confidence* baselines (see § 4.1.1) where the exact min-marginals are computed using dynamic graph-cuts [58].

4.2.3.2 Results

For each of the 50 test images in PascalVOC₁₀ the MAP segmentation cutout plus five additional modes was generated using the approaches described above. Table 4.2 shows the best-out-of-6 cutout accuracies averaged over 50 images for the different methods. Note that the *DivMBEST* cutouts (column two) achieves the best results. Some

	MAP	MModes-dot prod.	MModes-HOP	M-Best	Random	Confidence
Acc.(%)	91.542	95.16	93.82	91.59	91.68	93.17

Table 4.2: Interactive segmentation: pixel accuracies averaged over 50 test images.

example cutouts are shown in figure 2.2. Notice how Yanover and Weiss’ [127] 2nd-best MAP cutout is almost identical to the MAP cutout. In contrast the 2nd-mode of *DivMBEST* is qualitatively different and more likely the cutout the user intended. The 2nd-mode corrects where the MAP solution has likely made a mistake, for example the arm of the person in the first image is completed and a second instance of an object category is found in other image. The MAP solution suggests that the interactive segmentation model (TSVM + contrast sensitive Potts) does not perfectly capture the most probable cutout the user intended and yet we see that other modes of the underlying model distribution correspond to good segmentations. With *DivMBEST* we have a framework that provides a principled way of extracting these other segmentations.

4.3 FIGURE-GROUND SEGMENTATION

² This section presents the application of the *DivMBEST* framework to the figure-ground image segmentation task. Instead of relying on a complex model for foreground and background, the approach uses a simple binary pairwise CRF which relies on features computed over superpixels. The CRF can be learned efficiently using Structured SVM formulation.

Figure-ground segmentation can be used as input to multi-category segmentation models, or used in feed-forward approaches as a way to generate a set of candidate masks that are processed further [16, 92]. As such generating high-quality figure-ground segmentations of an image is an important task.

A common approach to category-level image segmentation relies on building structured probabilistic models with low-order interactions (such as pairwise CRFs). Such models are appealing because inference over them tends to be tractable and is often guaranteed to be optimal. On the other hand the simplifying independence assumptions of these models lead to exact MAP assignments that are highly inaccurate. In contrast, more complex models have been introduced that incorporate different types of higher-order interactions over the image such as cardinality and co-occurrence potentials [60, 70, 111] and hierarchical CRFs [68]. However, even though these models may better capture complex statistics of natural scenes they can be inefficient and

² The contributions to the thesis presented in this section are found in [126], and are in collaboration with Gregory Shakhnarovich.

slow to train. Therefore approximate inference algorithms are often needed to make inference tractable.

In contrast, this section presents a fairly simple probabilistic model for figure-ground segmentation where inference is efficient. While the inferred MAP solution is often not good enough, the set of solutions generated from this model using the *DivMBEST* method tend to contain highly accurate segmentations. This suggests that even though the model does not accurately model the most likely figure-ground segmentation, the underlying CRF distribution tends to have high quality solutions as one of its *modes*. The next section introduces our simple figure-ground CRF model.

4.3.1 CRF Model

We represent the image, I , as a set of n disjoint superpixels, $I = \{X_1, \dots, X_n\}$, and $\mathcal{V} = [n]$. We define a graph $G = (V, E)$ where the vertices correspond to superpixels and edges connect adjacent superpixels in the image. A segmentation corresponds to an assignment $\mathbf{x} = \{x_1, \dots, x_n\} \in \{0, 1\}^n$, where $x_s = 1$ indicates assignment of X_s to foreground. The binary CRF energy is defined to be,

$$E(\mathbf{x}; \mathbf{u}) = \mathbf{u}_1^T \sum_{s \in V} \theta_1(x_s) + \mathbf{u}_2^T \sum_{(s,t) \in E} \theta_2(x_s, x_t) + \mathbf{u}_c \sum_{s \in V} \theta_c(x_s) + \sum_{(s,t) \in E} \theta_e(x_s, x_t). \quad (4.7)$$

The unary and pairwise potentials are $\theta_1(\cdot)$ and $\theta_2(\cdot)$ respectively. Potential functions $\theta_c(\cdot)$ and $\theta_e(\cdot)$ are cardinality potentials on the nodes and edges respectively.

Intuitively, the unary θ_1 captures characteristic properties of superpixels in figure vs. background classes, while the pairwise θ_2 captures the likelihood of neighboring regions to be assigned the same class.

4.3.2 CRF potentials

The details of each type of potential are described below.

UNARY: The unary potential consists of p -channels, $\theta_1 = (\theta_{11}, \dots, \theta_{1p})$. The j^{th} channel is defined to be,

$$\theta_{1j}(X_s = x_s) \doteq P(X_s = x_s \mid \boldsymbol{\phi}_{1j}(X_s); \mathbf{w}_{1j}). \quad (4.8)$$

The channel captures the likelihood that superpixel s belongs to a foreground/background object, given the j^{th} unary features computed on the superpixel, $\boldsymbol{\phi}_{1j}(X_s)$, and

learned parameters \mathbf{w}_{1j} . The background score is simply $\theta_{1j}(X_s = 0) = 1 - \theta_{1j}(X_s = 1)$. The foreground probability of a superpixel is modelled as a logistic regression classifier,

$$P(X_s = 1 \mid \Phi_{1j}(X_s); \mathbf{w}_{1j}) \doteq \sigma(\langle \mathbf{w}_{1j}, \Phi_{1j}(X_s) \rangle), \quad (4.9)$$

where $\sigma(z) = 1/(1 + e^{-z})$. Since foreground is less common than background, we use asymmetric logistic loss, tuned to provide 90% recall for foreground on training data.

PAIRWISE: The pairwise potential consist of q -channels, $\theta_2 = (\theta_{21}, \dots, \theta_{2q})$. The k^{th} pairwise channel is defined as,

$$\theta_{2k}(X_s = x_s, X_t = x_t) \doteq P(x_s \neq x_t \mid \Phi_{2k}(X_s, X_t); \mathbf{w}_{2k}), \quad (4.10)$$

and captures the likelihood that adjacent superpixels X_s and X_t should have consistent labels, according to the k^{th} pairwise features $\Phi_{2k}(X_s, X_t)$ and learned parameters \mathbf{w}_{2k} . The pairwise potentials are modelled as a logistic regression classifiers similar to the unary case, and trained with asymmetric logistic loss tuned to achieve 90% recall for neighboring regions with different labels.

HIGHER ORDER: The third and fourth terms in the CRF energy of eqn. 4.7 are unary and pairwise *cardinality* potentials [113] respectively. They are a function of the global solution and not local image evidence. The unary potentials are defined as,

$$\theta_c(x_s) \doteq \llbracket x_s = 1 \rrbracket, \quad (4.11)$$

and count the number of superpixels labelled foreground, capturing what portion of the image is assigned to foreground.

The pairwise cardinality potentials are,

$$\theta_e(x_s) \doteq \llbracket x_s = x_t \rrbracket, \quad (4.12)$$

and measure the length of the boundary between foreground and background regions in the solution.

4.3.3 Features

4.3.3.1 Superpixel (unary) features

The segmentation model relies on basic appearance features described below.

INTENSITY HISTOGRAMS We bin the intensity into n_c equally spaced bins. Since color/intensity distribution within an image may be skewed, this may be an inefficient binning scheme, and so we also use adaptive binning according to $1/n_c$ quantiles of the intensity in the given image. For graylevel images this produces four histograms: fixed and adaptive binning schemes, each with $n_c = 8$ and with $n_c = 32$ bins. For color images there are twelve histograms, four per each dimension in the L*a*b space.

TEXTON HISTOGRAM We compute a dictionary of 32 textons [78] on all training images, using a bank of 12 filters. Histogram of texton assignments within a region forms a single 32-dimensional histogram.

GRADIENT FEATURES We compute the histogram of oriented gradient [24] within the region, binned into four directional bins. Furthermore, we compute the statistics of the gradient magnitude: sum of L_2 and of L_1 norms of the gradients within region, as well as the ratio of the two sums, known as blur index [53].

ENTROPY FEATURES Finally, we set up one-dimensional features computed as measures of entropy of histogram-based features. This is intended to capture how homogeneous a region is. There is one entropy value for each intensity, texton and gradient histogram; total of 6 for graylevel and 14 for color images.

Note that in contrast to many other models, we do not employ HoG/SIFT descriptors or shape features in this model. This is because at the level of small superpixels we do not expect such features to be informative.

4.3.3.2 *Boundary (pairwise) features*

HISTOGRAM DIFFERENCES For each of the histogram-based unary features we compute the χ^2 difference between the two regions. We also compute the earth mover's distance (EMD) between the histograms. High values of these features here indicate different color/intensity content between the two regions.

ENTROPY DIFFERENCES For each entropy feature, we compute the absolute value of the difference in entropies. High value here indicates one region is more homogeneous than the other in the respective feature.

BOUNDARY STRENGTH We compute the integral of the boundary probability according to gPb [77] along the boundary between the two regions. High value corresponds to pronounced boundary evidence according to gPb.

MSEER CORRELATION We extract a set of maximally stable extremal regions (MSERs, [80]), and for each MSER compute the percentage of the superpixel covered by that MSER. With M MSERs, this produces an M -dimensional vector for each superpixels. The cor-

relation coefficient of these vectors is a pairwise feature; high value indicates that the two superpixels tend to belong to the same MSERs. This and the next feature were inspired by ideas in [81].

MSER OVERLAP Another pairwise feature is the largest overlap of any of the MSERs and the union of the two superpixels. Higher value of this feature indicates that “merging” the two superpixels in the same mask is better supported by MSERs.

All of these features could be used directly in the model (eqn. 4.7). However, this would lead to a fairly high-dimensional parameterization making learning more challenging. Instead we proceed in two stages. First we train for each unary feature group $\Phi_{1j}(X_s)$ (each histogram, each entropy value, etc.) a logistic regression classifier $\sigma(\langle \mathbf{w}_{1j}, \Phi_{1j}(X_s) \rangle)$ predicting FG/BG label. Similarly, for each pairwise feature group $\Phi_{2k}(X_s, X_t)$ we train a classifier predicting whether the two superpixels are in the same class or not.

4.3.4 CRF learning

Instead of using max-likelihood training to learn the CRF weights $\mathbf{u} = (\mathbf{u}_1, \mathbf{u}_2, \mathbf{u}_c, \mathbf{u}_e)$ in eqn. 4.7 we optimize the following Structured SVM [114] objective,

$$\mathbf{u} = \underset{\mathbf{u}, \xi \geq 0}{\operatorname{argmin}} \frac{1}{2} \|\mathbf{u}\|_2^2 + C \cdot \xi \quad (4.13a)$$

$$\text{s.t.} \quad \frac{1}{N} \sum_{i \in [N]} \max_{\bar{\mathbf{x}}_i \in \mathcal{X}} [\mathcal{L}(\mathbf{x}_i, \bar{\mathbf{x}}_i) - \langle \mathbf{u}, \boldsymbol{\psi}(I_i, \bar{\mathbf{x}}_i) \rangle + \langle \mathbf{u}, \boldsymbol{\psi}(I_i, \mathbf{x}_i^*) \rangle] \leq \xi, \quad (4.13b)$$

where I_i represents the i^{th} image and \mathbf{x}_i^* is the best segmentation achievable given a particular superpixel partitioning of image I_i . For an image with n superpixels the potential values are pooled across all nodes and edges,

$$\boldsymbol{\psi}(I^i, \bar{\mathbf{x}}_i) = \begin{bmatrix} \sum_{s \in [n]} \theta_1(\mathbf{x}_{is}) \\ \sum_{(s,t) \in E} \theta_2(\mathbf{x}_{is}, \mathbf{x}_{it}) \\ \sum_{s \in [n]} \theta_c(\mathbf{x}_{is}) \\ \sum_{(s,t) \in E} \theta_e(\mathbf{x}_{is}, \mathbf{x}_{it}) \end{bmatrix}, \quad (4.14)$$

and the task loss $\mathcal{L}(\mathbf{x}_i, \bar{\mathbf{x}}_i)$ is discussed in the next section. The quadratic program in eqn. 4.13 is a one-slack, margin-rescaled, structural SVM [48].

4.3.5 Task loss

The task loss we use for the binary segmentation problem is the intersection-over-union score (IoU) for predicting segmentation \bar{x}_i with respect to the ground-truth for image I_i . It can be written as,

$$\text{IoU}(\bar{x}) = \frac{1}{2} \sum_{\ell \in \{0,1\}} \frac{\sum_j \llbracket \bar{p}_j = \ell \wedge p_j^* = \ell \rrbracket}{\sum_j \llbracket \bar{p}_j = \ell \vee p_j^* = \ell \rrbracket} \quad , \quad (4.15)$$

where $\bar{p}_j \doteq g(\bar{x})$, $g(\cdot)$ is a function mapping a figure-ground segmentation over superpixels to the label assignment of the underlying pixels in the image, $g : \mathcal{X} \rightarrow \{0, 1\}^{w \times h}$, and $j \in \{1, \dots, wh\}$. The ground-truth label pixel label assignment is p_j^* .

Since superpixels are the underlying image elements used in the model it is unlikely that a perfect image segmentation can be achieved, *i.e.* $\text{IoU}(\mathbf{x}^*) < 1$. This is because the superpixels may not have perfect alignment with foreground objects. Instead, we use a task loss that measures performance *relative* to the best achievable segmentation when committed to a specific set of superpixels,

$$\mathcal{L}(\mathbf{x}^*, \bar{x}) \doteq \text{IoU}(\mathbf{x}^*) - \text{IoU}(\bar{x}). \quad (4.16)$$

where \mathbf{x}^* is the best segmentation achievable and $\mathcal{L}(\cdot, \cdot) \in [0, 1]$.

4.3.6 Loss-augmented inference

The MAP solution to the binary CRF in eqn 4.7 given parameters \mathbf{u} , as well as the loss-augmented inference in eqn 4.13b were solved using graph-cuts [62]. The pairwise smoothness term in eqn 4.7 is not submodular so the graph-cut algorithm is not guaranteed to return an optimal solution, however we consistently attained good performance using this approach.

The constraint in eqn 4.13b uses the relative task loss defined in eqn 4.16. Since the intersection-over-union score doesn't decompose over image elements, the loss-augmented inference problem is more difficult to solve. We can approximately solve it by solving the simpler problem,

$$\min_{\bar{x}_i \in \mathcal{X}} \langle \mathbf{u}, \psi(I^i, \bar{x}_i) \rangle, \quad (4.17)$$

using graph-cuts and applying a greedy hill climbing procedure that sequentially flips the label of each superpixel in image i , x_{ij} , in order to maximize the loss adjusted score of the predicted solution relative to the ground-truth, until no more improvement can be attained. Alternatively a message-passing inference algorithm designed to handle high-order potentials [112] could have been used to approximately solve the loss-augmented inference problem.

4.3.7 *DivMBEST inference with Hamming dissimilarity*

Given a fixed C and model parameters \mathbf{u} from training the CRF (§ 4.3.4), we can generate a diverse set of plausible segmentations using the *DivMBEST* framework. In order to compute *DivMBEST* solutions (§ 2.2.7) we use Hamming dissimilarity for the Δ -function. The m^{th} -mode is generated by solving the following minimization problem,

$$\mathbf{x}_i^{(m)} = \operatorname{argmin}_{\bar{\mathbf{x}}_i \in \mathcal{X}} \sum_{j \in [n]} \left[\mathbf{u}_1^T \boldsymbol{\theta}_1(\bar{\mathbf{x}}_{ij}) + \sum_{k \in [m-1]} \lambda \cdot \llbracket \bar{\mathbf{x}}_{ij} = \mathbf{x}_{ij}^{(k)} \rrbracket \right] + \sum_{(s,t) \in E} \mathbf{u}_2^T \boldsymbol{\theta}_2(\bar{\mathbf{x}}_{is}, \bar{\mathbf{x}}_{it}) + \sum_{j \in [n]} \mathbf{u}_c \boldsymbol{\theta}_c(\bar{\mathbf{x}}_{ij}) + \sum_{(s,t) \in E} \boldsymbol{\theta}_e(\bar{\mathbf{x}}_{is}, \bar{\mathbf{x}}_{it}). \quad (4.18)$$

We use the same s - t graph-cut implementation [62] to solve this problem as we use to compute the MAP solution. The value of λ is set using cross-validation on the training set.

4.3.8 *Superpixels*

In order to have a computationally efficient model that produces segmentations with good alignment to internal image boundaries superpixels are used as opposed to the image pixels. To produce the superpixels the SLIC superpixel segmentation algorithm [1] is employed. For each image the desired number of superpixels is set to 400.

4.3.9 *Experiments*

The purpose of the experiments in this section is to evaluate the quality of the segmentations from our figure-ground model produced by the *DivMBEST* method.

4.3.9.1 *Data sets*

We experimented with four benchmark data sets of natural images designed for evaluation of figure ground segmentation, and an additional data set of radiological images.

WEIZMANN HORSES [10] 328 color images of horses. This is the easiest of the five data sets, with large prominent foreground (horses in a variety of scenes).

GRAZ BIKES, CARS, PEOPLE [79] Each set contains 300 color images, generally harder than horses: bikes and cars in a variety of orientations and locations, some partially occluded, and people in a variety of locations/poses and with varying degree of occlusion.

ULTRASOUND This medical dataset contains 416 ultrasound (graylevel) images collected from five hospitals with different acquisition devices, varying image quality, noise levels and resolutions. Each image in the set contains a single lesion with validated pathology diagnosis. The ground truth segmentation for each image was created manually by a radiologist, who marked the boundary of lesions. We include this data set to evaluate the performance of the proposed, very general, segmentation approach on images very different from the natural scenes in the other sets. We plan to make the data set including annotations public.

4.3.9.2 Evaluation

The Weizmann horses and the three Graz data sets are split into a single train/test split with $1/3$ of the horses and $1/2$ of the Graz data sets used as test sets [66] on which we report performance. For cross-validation purposes the ultrasound data set is split into five equal folds. The average of the five evaluations is reported, where one of the five folds is used as the test set and the remaining four folds used for training. In all the experiments the CRF learnable parameters and diversity weight λ were tuned using cross-validation on the training set.

The goal of the evaluation in this section is to determine whether generating a diverse set of plausible segmentations for the figure-ground problem can be beneficial. Therefore we evaluate the *oracle* performance (*i.e.* best segmentation in the *DivMBEST* set) against the MAP solutions.

The model MAP and *oracle* performance is evaluated in the context of state-of-the-art among the published work at the time of these experiments. For this purpose we compare our results to those in [66], which were shown to be competitive for the state-of-the-art title.

PERFORMANCE MEASURES Performance is measured by intersection-over-union (IoU) score which is most common measure used in semantic segmentation. IoU is also the task loss that is used in learning the CRF. For each experiment the results are reported in terms of *average IoU* over the images in the test set(s).

RUNNING TIME For a typical image the CRF model has approximately 400 variables. Once the bottom-up segmentation CRF is trained, producing a diverse set of

	MAP	Oracle	%gap	[66]
Weizman horses	75.4	83.0	51.3%	79.1
Graz bikes	53.1	61.4	36.1%	45.0
Graz cars	50.0	66.3	59.5%	58.8
Graz people	44.1	57.0	26.4%	47.5
Ultrasound	39.7	57.3	58.0%	26.6

Table 4.3: Segmentation performance on all data sets, in IoU values $\times 100$. MAP: single solution from the bottom-up CRF model. *Oracle*: (hindsight) best of 10 diverse solutions from the CRF. Third column: percentage of gap (oracle-MAP) recovered by the ranking. Last column: Figure-ground segmentation model of Kuettel *et al.* [66].

segmentations for a new images involves the following stages. SLIC superpixels are extracted and the CRF features are computed (≈ 15 sec/image on a 6-core machine). Bottom-up inference of 10 diverse solutions using graph cuts takes approximately 5 seconds.

4.3.9.3 Results

The oracle performance of the *DivMBEST* segmentations for all data sets is summarized in table 4.3. A single MAP segmentation gives reasonable accuracy compared to results from a state-of-the-art figure-ground segmentation model [66] at the time of these experiments. But the MAP solution is inferior to the of the oracle performance over just a small set of 10 *DivMBEST* solutions. The oracle is in fact superior to a state-of-the-art method that does not generate multiple segmentations. In later chapter we'll explore the 1-out-of-10 inference problem using the *DivMBEST+ReRANK* framework to automatically pick the likely best segmentation from the set.

Examples of the MAP vs. *DivMBEST oracle* figure-ground segmentations using the proposed CRF are shown in figures 4.2 and 4.3 along with the ground-truth segmentations. Note how the MAP foreground regions often "bleed" into the surrounding regions whereas the *oracle* results show that there is typically a *mode* of the solution space distribution that can accurately recover the foreground boundaries.

Samples of the *DivMBEST* foreground segmentations for the Horses and Graz datasets can be found in Appendix A.1.

4.4 MULTI-CATEGORY SEGMENTATION

³ So far we have seen that the *DivMBEST* framework can generate sets which often contain segmentations better than the MAP solution for a number of segmentation tasks. In this section we further apply the *DivMBEST* algorithm to the multi-category segmentation problem. The *DivMBEST* solutions are evaluated against the MAP segmentation produced by three different discrete probabilistic models.

4.4.1 Hierarchical model

The first model we consider is the Associative Hierarchical CRF of Ladicky *et al.* [68] (see § 1.1.1). At the time of evaluation this model gave competitive performance on the multi-category segmentation task. Experiments use the Automatic Labeling Environment (ALE) [67] which is an implementation of the hierarchical CRF model by the authors. The model incorporates a number of potentials including unary potentials that look at local texture (based on textonboost features [106, 107]), low-level pairwise P^n Potts potentials [55] between pixels and similar mid-level potentials between superpixels, as well as a global co-occurrence potential[69].

The graph-cut inference algorithm of Ladicky *et al.* [68, 69] is used to compute the MAP solution over this hierarchical model. Assuming a Hamming dissimilarity function $\Delta(\cdot, \cdot)$, we can compute the subsequent *modes* (*i.e.* *DivMBEST* segmentations) by appropriately modifying the unary potentials according to the *DivMBEST* formulation and rerunning the same inference algorithm.

4.4.1.1 Baselines

The same baselines as in the figure-ground experiments are used (see § 4.3). The *random* baseline averaged over ten runs as well as the *confidence* baseline are reported. The M-Best MAP algorithm [127] (cf. § 2.1.3) is infeasibly slow to run for this model. Since the energy is not sub-modular computing min-marginals cannot be done efficiently. Even with an implementation that re-uses search trees and caches α -expansion graphs it would take 10 years to compute each additional solution for each image. Computing *DivMBEST* solutions, however, takes the same amount of time as computing the MAP solution.

³ Part of the contributions to the thesis presented in this section are found in [7], and are in collaboration with Gregory Shakhnarovich and Dhruv Batra.

	Backgr.	Plane	Bicycle	Bird	Boat	Bottle	Bus	Car	Cat	Chair	Cow	D.Table	Dog	Horse	M.bike	Person	Plant	Sheep	Sofa	Train	TV.Mo.	Average
MAP	78.5	35.1	5.2	20.3	20.8	11.8	39.4	38.2	25.8	8.9	14.1	30.2	10.0	12.3	37.6	33.5	10.3	24.2	16.2	28.7	20.5	24.8
Confidence	78.5	35.1	5.3	20.1	20.7	12.6	39.4	37.9	26.8	8.9	14.1	30.2	10.3	12.2	39.5	33.4	10.6	24.2	17.3	28.4	20.5	25.1
Random	74.9	32.4	6.4	16.1	14.7	12.3	34.3	32.6	22.6	8.0	13.2	21.1	8.7	10.4	32.9	28.9	7.8	20.6	10.8	23.5	17.3	21.4
10MODES	85.6	53.9	14.6	36.9	33.6	33.2	64.2	56.3	47.7	16.1	30.3	46.8	29.1	28.7	59.0	50.0	32.5	46.7	31.2	52.9	39.0	42.3

Table 4.4: Pascal VOC 2010 val set accuracies for ALE model.

	Backgr.	Plane	Bicycle	Bird	Boat	Bottle	Bus	Car	Cat	Chair	Cow	D.Table	Dog	Horse	M.bike	Person	Plant	Sheep	Sofa	Train	TV.Mo.	Average
MAP	73.7	44.0	14.2	15.3	21.0	23.2	41.3	37.0	27.6	6.1	23.9	25.2	12.8	24.3	51.0	27.8	20.0	28.2	17.1	36.5	23.9	28.3
10MODES	83.4	54.4	19.6	22.4	34.5	22.2	60.8	55.5	45.8	14.0	45.5	35.1	34.8	40.1	53.6	48.7	28.0	48.7	31.2	50.5	33.9	41.1

Table 4.5: Pascal VOC 2010 test set accuracies for ALE model.

4.4.1.2 Dataset

Multi-category level experiments were carried out on the PASCAL Visual Object Classes (VOC) 2010 segmentation benchmark [29]. PASCAL VOC 2010 contains 21 semantic categories (20 object categories ($\{aeroplane, bicycle, bird, bottle, car, \dots\} + background$), and the task is to label every pixel in the image with one of the 20 object categories or the background. This task is part of the PASCAL VOC challenge. The dataset contains train, val, and test splits that contain 964 images each. The object categories appear in natural scenes under varying appearance, lighting, and pose. Many images contain multiple instances of the same category and more than one category can appear in the same image.

Segmentation accuracy is scored using the standard PASCAL VOC intersection-over-union (IoU) measure (*i.e.* pixelwise $\frac{\text{intersection}}{\text{union}}$ measure averaged over masks of all categories). The relevant parameters, such as the multiplier on the diversity term (λ) in the *DivMBEST* formulation, are tuned on the val set, after the model has been trained on train. Ground-truth segmentations are not provided for test but test set accuracies can be obtained by submitting a single segmentation prediction per image to the VOC evaluation server.

4.4.1.3 Results

To measure the upper-bound on segmentation accuracy achievable with the *DivMBEST* solutions we evaluate on the val set for which we have ground-truth. *Oracle* accuracy is computed as follows: for each image the segmentation in the *DivMBEST* set that has highest pixel-wise IoU w.r.t ground-truth (averaged over all category masks) is

selected. The results on `val` for 10 *DivMBEST* *modes* for ALE are reported in table 4.4 along with the MAP accuracy and baselines that generate multiple solutions using different perturbation strategies on the MAP segmentation. The result on `test` using 10-*modes* is summarized in table 4.5. To illustrate how the upper-bound on segmentation accuracy grows as the number of solutions increases, figure 4.4a shows a plot of *oracle* accuracy versus number of *DivMBEST* solutions. The MAP accuracy is shown as the dashed horizontal line, and the accuracy of the *confidence* based solution is only slightly better than MAP. With $m = 30$ solutions the *oracle* accuracy reaches 48% on `val`. Though `val` and `test` set performance aren't directly comparable the *oracle* performance on `test` is likely better — by a significant margin — than state-of-the-art methods at the time of experiments.² Sample *DivMBEST* segmentations on PASCAL VOC 2010 `val` set images are shown in Appendix A.2.

² the winning entry of VOC2010 comp5 challenge achieved 40.1% on test

4.4.1.4 Evaluating *DivMBEST* modes

Figure 4.4b shows a plot of the distance of the *DivMBEST* solutions (aka *modes*) to the MAP solution and previous modes. The normalized (w.r.t image size) Hamming distance between solutions monotonically increases with each additional solution. This show that the *DivMBEST* Hamming dissimilarity constraints (i.e. $\Delta(\mu, \mu^{(i)}) \geq k$) are encouraging diversity between solutions. The energy of the modes as a percentage of the MAP energy is shown in figures 4.4c and 4.4d. A majority of *modes* have higher energy than the MAP solution³. A small proportion of *modes* have less energy than MAP due to the fact that the model uses *approximate* inference.

³ guaranteed if using exact inference

4.4.2 Feed-forward model

In ALE complex interactions between image elements is captured by the hierarchical structure of the graph and the higher-order graph cliques. An alternative approach is presented by the Second-Order Pooling (O_2P) approach of Carreira *et al.* [17]. In O_2P , complex interactions between regions in the image are captured by global region descriptors that are constructed by second-order pooling of local descriptors such as SIFT and local binary patterns (LBP) [85, 86]. Carreira *et al.* present a simple inference algorithm for the O_2P model, which can be applied directly to generating the diverse segmentations of the *DivMBEST* algorithm with Hamming dissimilarity. The details of the model and evaluation are deferred to Chapter 5 where we also evaluate an approach to re-ranking the *DivMBEST* solutions.

4.4.3 Convolutional neural network + dense CRF model

Current state-of-the-art semantic segmentation is done by combining very deep convolutional neural networks (CNNs) or residual neural networks (RNNs) with fully connected dense pairwise CRFs [18] [43]. Deep networks are superior at building local features that capture information at multiple spatial scales of the image, however the output suffers from a decrease in resolution compared to the input image. Dense pairwise CRFs can introduce low-order dependencies between image elements, that are not constrained to be local. Additionally local pairwise potentials can provide spatial smoothness constraints on the solution and improve alignment with image boundaries. Piggy-backing dense CRFs on top of deep segmentation networks combines the benefits of both approaches - efficient computation of complex features that incorporate both local and global interactions in the image along with constraints on local smoothness. We can view the CNN + dense CRF pipeline as a discrete probabilistic model on a dense pairwise graph where the unary potentials are defined by the output of the CNN at each image element (superpixel or pixel).

The *DivMBEST* framework is agnostic to the underlying discrete probabilistic model so we can apply it to this model in a similar manner as previous models. Given a CNN trained on the semantic segmentation task, the above deep network approaches use the features from the last layer of the network to initialize the unary potentials of a fully-connected CRF. For a fully-connected CRF where the pairwise edge potentials are defined by a linear combination of Gaussian kernels an efficient approximate inference algorithm exists [65] for computing the MAP solution. Approximate inference is based on an iterative message passing algorithm where messages are computed using efficient Gaussian filtering in feature space. Assuming pixel-wise Hamming diversity constraints between solutions the *DivMBEST* algorithm amounts to modifying the unary potentials and rerunning the message passing algorithm to compute successive solutions.

We investigate the benefit of applying *DivMBEST* to one such deep neural network + dense CRF pipeline – we use the Zoom-out network [82] with the DeepLab dense CRF implementation [18][65]. The Zoom-out network (cf. § 1.1.1) is first pre-trained to perform multi-category image classification on the ImageNet dataset [96]. Subsequently the final fully-connected layer of the CNN is modified to a fully-convolutional layer with output feature map depth set to 21^4 and spatial extents up-sampled to be the same size as the input image. The CNN is then fine-tuned in a end-to-end manner for the semantic segmentation task using the PASCAL VOC 2012 train set + 11.3K annotated PASCAL VOC 2011 images from the Semantic Boundaries Dataset [41]. Given a trained network, the dense CRF unary potentials are initialized with the features from the last fully-convolutional layer of the network, and the CRF hyper-parameters are fixed to the defaults set by the implementation of Chen *et al.* [18]. On the PASCAL VOC 2012 val set this pipeline achieves 72% MAP accuracy⁵ (IoU accuracy averaged

⁴ corresponding to the 21 PASCAL VOC categories

⁵ current state-of-the-art methods [124, 129] that use additional training data currently achieve ~ 85% accuracy on PASCAL VOC 2012

over all categories/images).

4.4.3.1 Dataset

The segmentation results in this section are reported on images from the PASCAL VOC 2012 benchmark [29]. It contains 4,369 images split into `train` (1,464 images), `val` (1,449 images), and `test` (1,456 images) sets. The CNN is pre-trained for the 1000-category classification task from the ImageNet Large Scale Visual Recognition Challenge (ILSVRC) [96], using $\simeq 1.2\text{M}$ ILSVRC2014 images. An additional 11.3K images from the Semantic Boundaries Dataset [41] are used along with PASCAL VOC 2012 `train` set to fine-tune the CNN to the 21-category PASCAL VOC segmentation task.

4.4.3.2 Results

We can explore the maximum accuracy achievable when using the *DivMBEST* algorithm to generate segmentations with the CNN + dense CRF model. To this end we evaluate two approaches to producing oracle segmentations for each image, (1) selecting the best-out-of- m segmentations based on accuracy relative to ground-truth and, (2) constructing full image labellings from connected components found in the m segmentations using a greedy inference approach.

The oracle accuracy versus MAP for the first approach can be seen in figure 4.5a. This suggest that if we pick the best-out-of-40 solutions we can achieve more than 5%-point improvement over MAP in overall segmentation accuracy. The second approach relies on a greedy inference algorithm over connected components (*i.e.* contiguous image regions taking the same label) found across the m segmentations. We first compute a bag containing tuples, (R_j, ℓ_j) of connected components R_j extracted from the m segmentations with corresponding category labels ℓ_j . Note that duplicate tuples can exist if a contiguous region with corresponding label is found in more than one image segmentations. We assign each connected component in the bag a score defined to be its highest IoU with all connected components taking the same label in the ground-truth segmentation. Starting with an empty labeling, the full image labeling for the image is constructed using a greedy strategy of *pasting* the connected components in order of decreasing IoU score until a prescribed score threshold is reached, at which point the algorithm stops. During the pasting procedure if the current connected component overlaps with a region in the image that has already been assigned a label then the previous label for pixels in that region is retained. A non-maxima suppression step is applied at each iteration: after pasting a connected component from the bag we cull the bag of all connected components that have intersection greater than a fixed threshold. The result of this greedy construction, as m varies from 1 to 40 solutions, is shown in figure 4.5b. Notice that the accuracy of greedy inference on connected components from the first solution (*i.e.* MAP) is higher than the accuracy of original MAP solution

computed on the model. This is because greedy inference on connected components culls from the final image labeling those connected components that do not align well with the ground truth segmentation. With this approach we get a significant increase in oracle accuracy compared to the best-out-of-m results – an almost 13% point increase over MAP. An example result of composing the oracle segmentation from the *DivMBEST* segmentations is shown in figure 4.6.

The MAP solution from current state-of-the-art models, that combine deep neural networks with dense CRFs, achieve comparable accuracy⁶ to this greedy-inference approach on the less accurate Zoom-out CNN + dense CRF model. The *oracle* results illustrate that it's plausible to leverage the *DivMBEST* algorithm to generate a set of diverse segmentations that often contain highly accurate solutions even when the MAP solution from the underlying segmentation model is inaccurate. This suggests that near state-of-the-art results can be had in the multi-category image segmentation problem⁷ by devising methods with the goal of picking the best solution from the *DivMBEST* set. We explore one such method in Chapter 3 that is learned with the goal of re-ranking the segmentations in set so that the best segmentation is top ranking.

⁶ ~ 85% on PASCAL VOC 2012 comp6 challenge [124, 129]

⁷ as well as the segmentation tasks presented earlier

4.4.4 Summary

The results on a number of semantic segmentation datasets show the utility of using the *DivMBEST* formulation to produce a diverse set of highly plausible segmentations. Specifically, the *oracle* accuracies show that across the segmentation tasks the *DivMBEST* set often contains much higher quality segmentations than MAP. This validates the alternative approach of leveraging models, in which exact or provable approximate inference is tractable, by efficiently producing a diverse set of segmentations as opposed to devising more complex models where inference becomes intractable. The *oracle* results highlight the importance of being able to pick the best segmentation from the *DivMBEST* set via ranking and we investigate this in chapter 5.

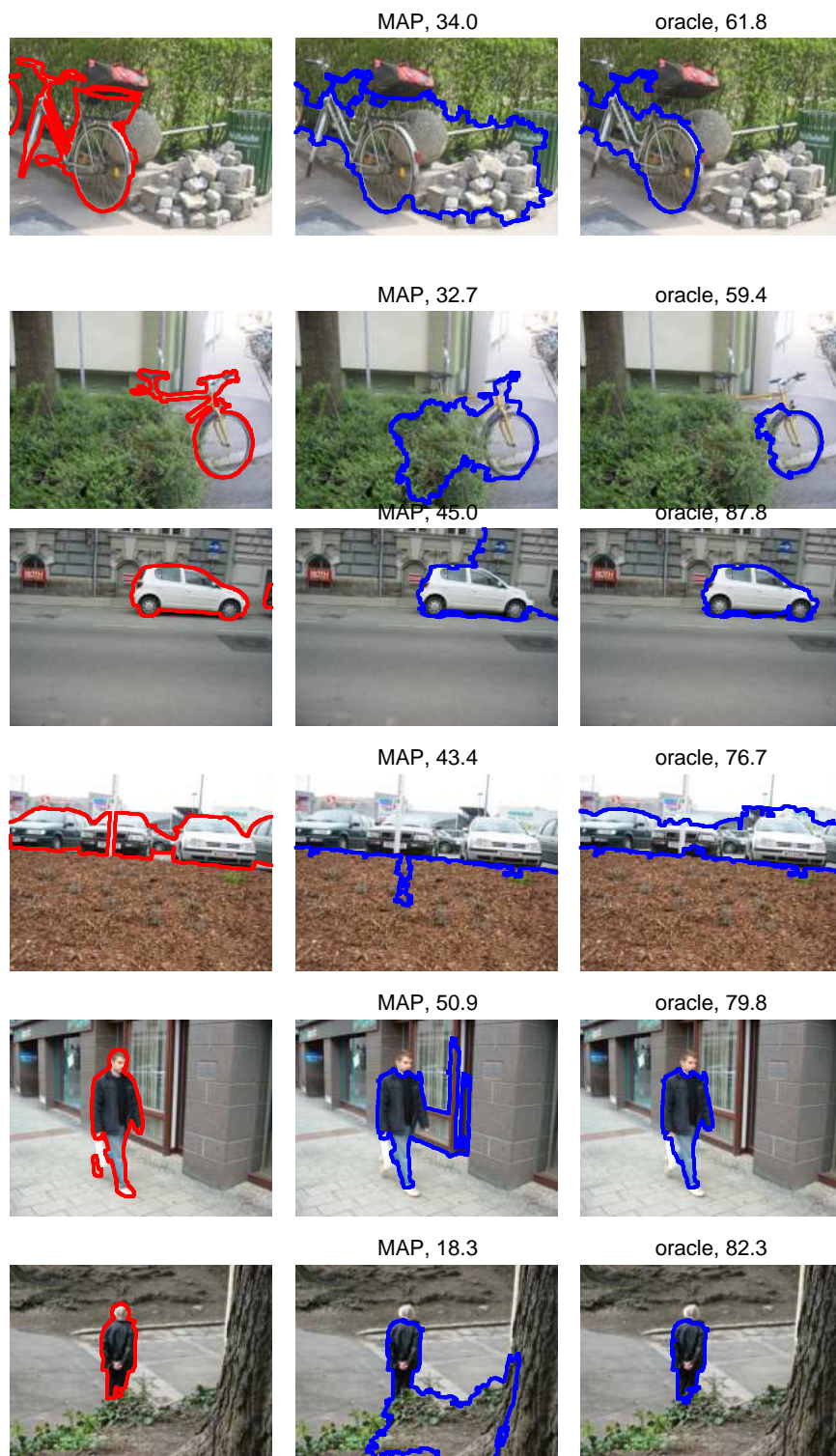


Figure 4.2: Examples of (left to right) input image with ground truth, MAP from the bottom-up CRF model, *oracle* out of 10 diverse solutions. All examples are from the test portions of Graz data sets.

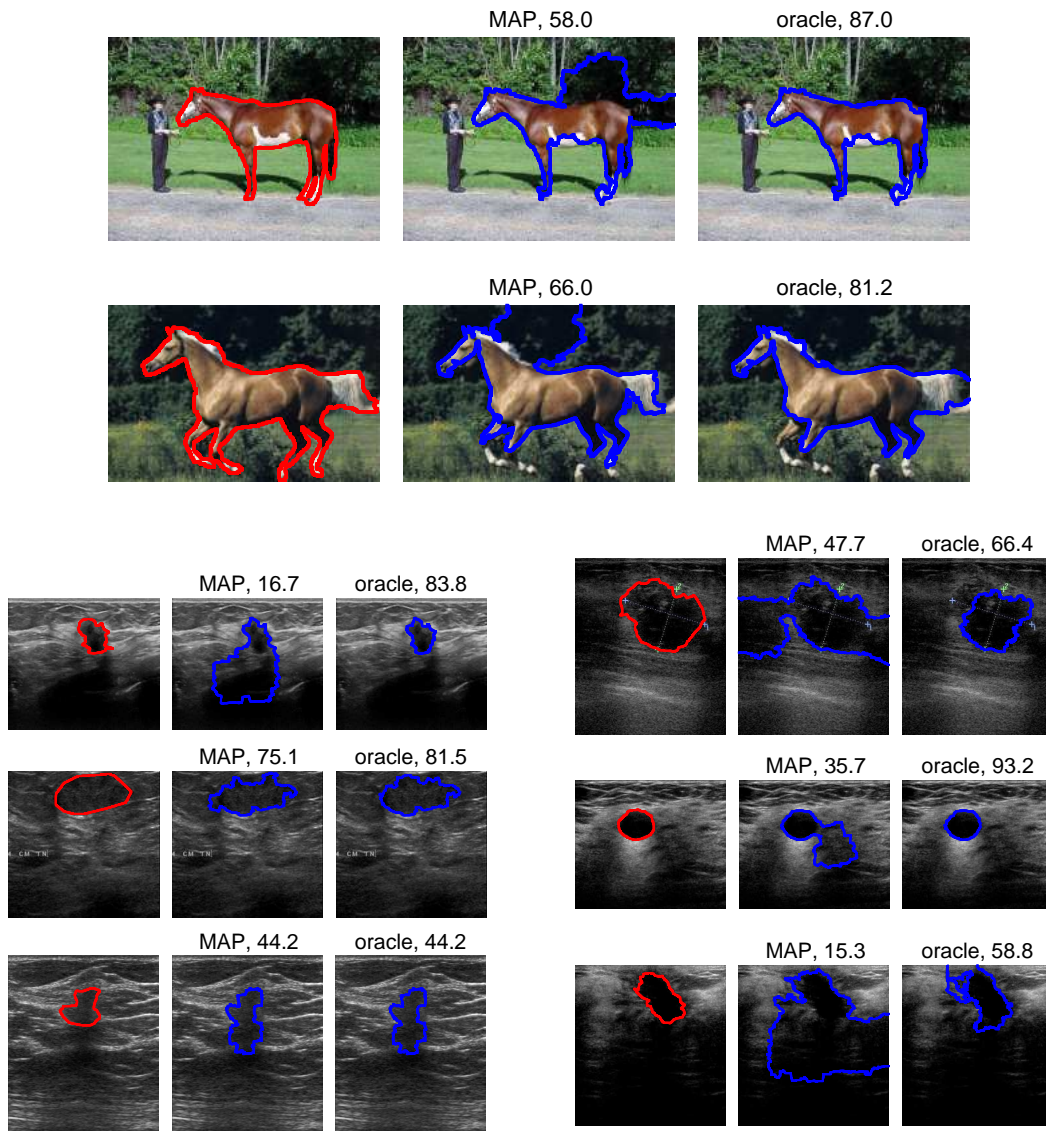


Figure 4.3: Examples of (left to right) input image with ground truth, MAP from the bottom-up CRF model, *oracle* out of 10 diverse solutions. Examples are from the test portion of Weizmann horses data set, and from one of the test folds of the Ultrasound data set. Last row shows some failures.

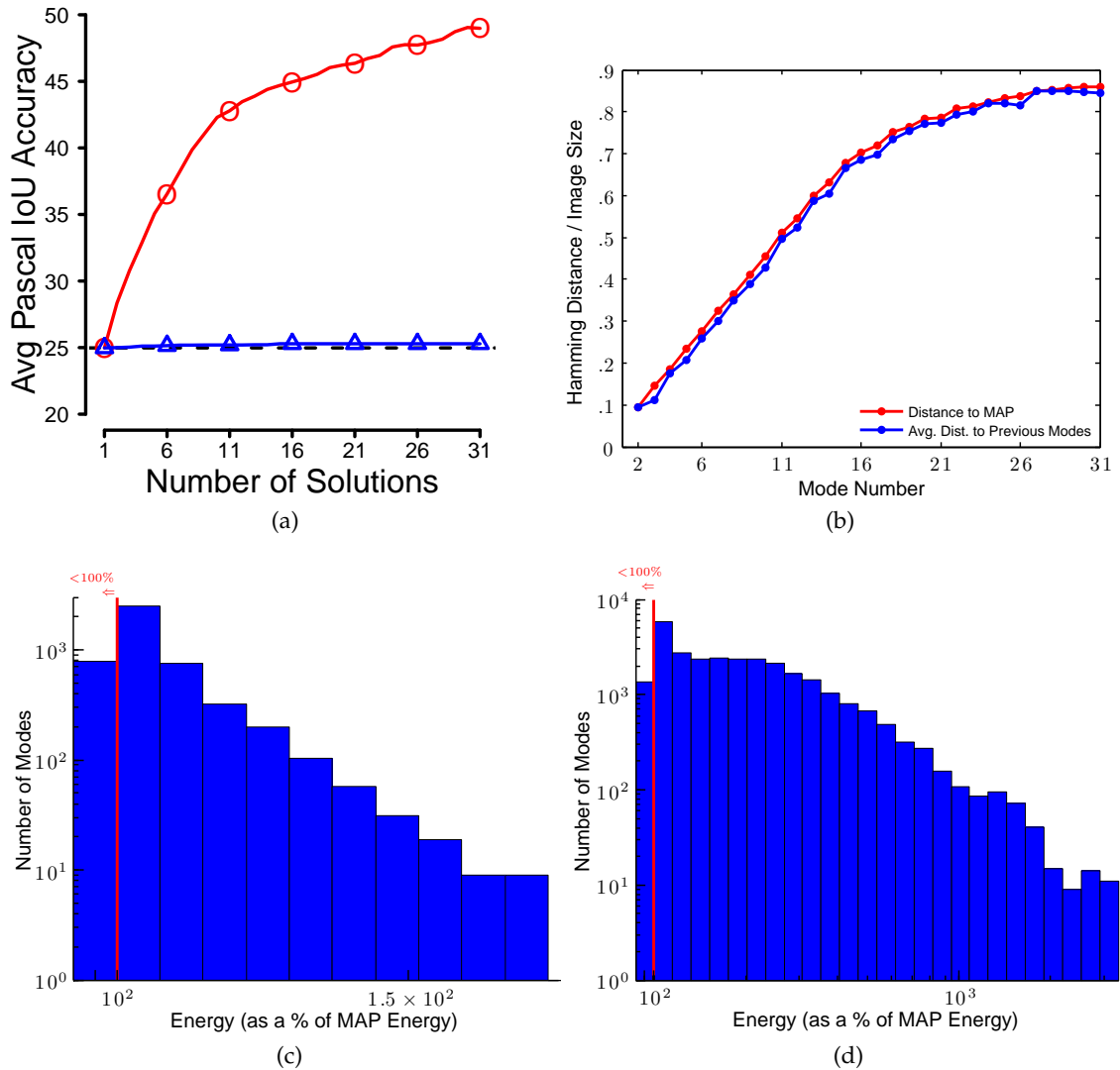


Figure 4.4: (a) Oracle accuracy vs. number solutions on VOC2010 val for DivMBEST (red) and confidence based perturbations (blue), along with MAP performance (black dashed). (b) Mean hamming distances between each mode (DivMBEST solution) and the MAP solution (red), and average to previous modes (blue), normalized by image size on PASCAL VOC 2010 val set. Also show, histogram of energies (as % of MAP) over (c) 6 modes, (d) 31 modes, on validation set. The bar to the left of red vertical lines indicate number of modes with energy less than or equal to MAP.

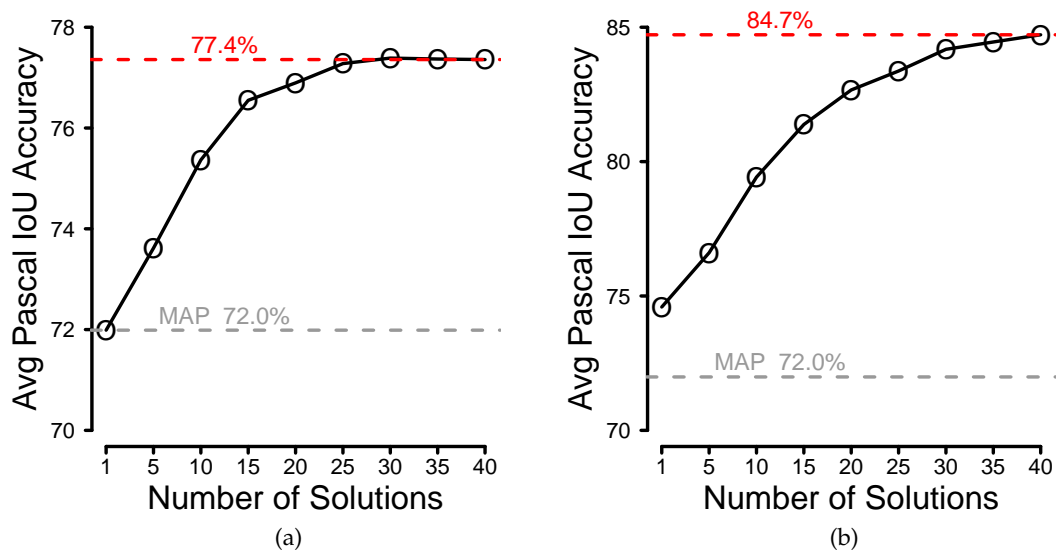


Figure 4.5: Oracle performance (IoU accuracy against ground-truth) on PASCAL VOC 2012 val, when (a) selecting best-out-of-m solutions, and (b) composing full image labellings from connected components found among m solutions.



Figure 4.6: Result of composing solutions from *DivMBEST* segments. Second and third row show a subset of 40 *DivMBEST* segmentations generated from the CNN+CRF model of § 4.4.3. First row shows in order the image, ground-truth segmentation, and composed segmentation oracle using the second approach of § 4.4.3.2. Note how the composed segmentation oracle is a much better segmentation of the image than the MAP solution (first segmentation in the second row).

DIVMBEST+RERANK EXPERIMENTS

5.1 EVALUATING DIVMBEST+RERERANK PIPELINE

To evaluate how well the proposed method in Chapter 3 re-ranks the *DivMBEST* solutions the following experiments are carried out,

1. Re-ranking of the object cut-outs generated from applying the *DivMBEST* algorithm to the figure-ground model in § 4.3.
2. Evaluate joint recognition and segmentation performance using the *DivMBEST+REERANK* pipeline on two multi-category segmentation models: the O_2P model by Carreira *et al.* [17], and the hierarchical ALE model by Ladicky *et al.* [67, 68].

5.2 FIGURE-GROUND SEGMENTATION

Recall that in § 4.3 we presented a model for figure-ground segmentation and evaluated *oracle* accuracy of *DivMBEST* solutions against MAP. We now evaluate the proposed *DivMBEST+REERANK* (cf. chapter 3) approach to segmentation where we take the *DivMBEST* segmentations from chapter 2 and rank them, returning the highest ranking segmentation in the set as the final solution.

5.2.1 Re-ranking segmentations

¹ Using the notation from § 3.2.1, let the i^{th} image be denoted as x_i and $\mathbf{Y}_i = \{\mathbf{y}_i^{(1)}, \dots, \mathbf{y}_i^{(m)}\}$ be the set of predicted foreground masks. A foreground mask, \mathbf{y}_i , is a labelling of all the n (super)pixels in the image where (super)pixel i can take labels from the set $\{0, 1\}$, *i.e.* $\mathbf{y}_i \in \{0, 1\}^n$. Given a feature-function that computes a p -length feature vector on an image/foreground mask pair, $\psi(x_i, \mathbf{y}_i^{(j)}) : \mathbb{R}^{3 \times w \times h} \times \{0, 1\}^n \rightarrow \mathbb{R}^p$, we learn a linear re-ranker model⁸,

⁸ refer to § 3.2.2

¹ The contributions to the thesis presented in this section are found in [126], and are in collaboration with Gregory Shakhnarovich.

$$S_r(\mathbf{y}_i) = \boldsymbol{\alpha}^T \boldsymbol{\Psi}(x_i, \mathbf{y}_i^{(j)}). \quad (5.1)$$

5.2.2 Ranking features

There are a few considerations that guide the design of region ranking features for our approach. These features need to be evaluated only on a small number of segmentations, hence we can afford fairly complex/expensive computation. Furthermore, these features will be deployed to evaluate entire hypothesized foreground masks, assumed to include high-quality ones. Therefore we can use image features that would be hard to incorporate into the bottom-up model, in particular, shape properties of the mask and its position in the image. In addition, we can incorporate properties of the hypothesized regions that are less meaningful for the small, regular superpixels; for instance, measurements of homogeneity of the regions. These considerations led us to design the following features.

SHAPE AND POSITION We extract the following properties of the hypothesized foreground mask: area; perimeter; location of centroid; minor/major axis length, eccentricity and orientation for an ellipse fit to the region; area of the convex hull of the region and its ratio to the area; Euler number (number of holes); diameter of the disk with area equal to that of the region; extent (fraction of the bounding box occupied by the mask); and finally size and location of the bounding box. All of these quantities are normalized per image (e.g., area is expressed in percentage of image area).

COLOR We compute histogram with 32 fixed bins for each color channel; we do not use adaptive binning as in the bottom-up model, since color distribution for entire objects is more stable than for small parts (superpixels).

TEXTURE We compute histogram of assignment to 32 textons [106], computed for the entire training set and not per image as in the bottom-up model.

ENTROPY For each histogram feature (color and texton) we compute its entropy. This measures the homogeneity of hypothesized object.

5.2.3 Re-ranker training

For each of the five experiments re-ranking parameters were learned on the training set of each dataset. The parameters were tuned by cross-validation on the training set.

	[66]	MAP	Oracle	Ranking	%gap
weizman horses	79.1	75.4	83.0	79.3	51.3%
graz bikes	45.0	53.1	61.4	56.1	36.1%
graz cars	58.8	50.0	66.3	59.7	59.5%
graz people	47.5	44.1	57.0	47.5	26.4%
ultrasound	26.6	39.7	57.3	49.9	58.0%

Table 5.1: Segmentation performance on all data sets, in IoU values $\times 100$. MAP: single solution from the bottom-up CRF model. *Oracle*: (hindsight) best of 10 diverse solutions from the CRF. Ranking: full ranking model (all features). last column: percentage of gap (oracle-map) recovered by the ranking.

Method	horses	bikes	cars	people	ultrasound
[66]	79.1	45.0	58.8	47.5	26.6
ours(full)	79.3	55.4	59.7	47.5	49.9
shape	73.7	54.8	58.6	44.7	48.2
textons	74.0	53.4	54.3	45.6	48.1
color	69.5	53.2	53.1	43.5	44.1
full-entropy	76.9	54.4	57.6	44.7	47.3

Table 5.2: Comparative results between methods and feature sets for region ranking. All numbers are $\text{IoU} \times 100$. Shape: only shape and position. Textons: only textons. Color: only color histograms. full-entropy: shape, color and textons, but not their entropies.

5.2.4 Results

Table 5.1 summarizes the results of re-ranking the *DivMBEST* solutions. In four out of five benchmarks region ranking closes the gap between *oracle* and MAP performance by up to or more than 50%. On Graz people $\sim 30\%$ of the gap is closed.

In all the datasets the *DivMBEST+RE-RANK* approach to figure-ground segmentation achieves accuracy equal to or better than [66].

The contribution of each of the re-ranking features to the re-ranker performance is summarized in Table 5.2. All the features contribute to the overall performance of the re-ranker across all datasets, however the amount of contribution per feature differs between datasets. For example, removing color features from the re-ranker drastically reduces performance on the Horses dataset, probably because the color distribution of background — which is often grass or foliage — is very different from foreground in these images. On Ultrasound dataset the color intensity is important because lesions

usually appear dark on the ultrasound but the importance of color features is less important than on Horses.

5.3 MULTI-CATEGORY SEGMENTATION

² We revisit the two multi-category segmentation models that we introduced in the *DivMBEST* experiments (cf. § 4.4), and evaluate segmentation performance of these models when predicting the best solution in the *DivMBEST* set for each image. To do this we use the *DivMBEST+RERANK* pipeline introduced in § 3.2.2.

5.3.1 Dataset

Evaluation of the *DivMBEST+RERANK* pipeline applied to the models below is carried out on the PASCAL VOC 2012 dataset [29], which contains the same 20 categories as VOC 2010 but with additional images for each category. There's a total of 4,369 images, split into train (1,464), val (1,449), and test (1,456 images) subsets.

5.3.2 Hierarchical model

We reviewed the Associative Hierarchical CRF of Ladicky *et al.* [68] in § 1.1.1 and corresponding ALE implementation, and showed that the *oracle* performance on *DivMBEST* segmentations improved by more than 20% over MAP on the val subset of PASCAL VOC 2010. To evaluate how good the *DivMBEST+RERANK* implementation is at returning a high quality segmentation of the image we produce diverse segmentations and rank them on images from the PASCAL VOC 2012 dataset.

5.3.3 Feed-forward model

We also compare against the Second-Order Pooling (O_2P) implementation of Carreira *et al.* [17] contrast with the Hierarchical CRF model above, in the way higher-order dependencies are incorporated in the model. Whereas is ALE the higher-order interactions are due to the hierarchical structure of the graph and high-order cliques, O_2P incorporates high-order dependencies using second-order pooling of local descriptors over regions in the image.

² Part of the contributions to the thesis presented in this section are found in [7], and are in collaboration with Gregory Shakhnarovich and Dhruv Batra.

In O_2P , for each image location local descriptors such as SIFT and local binary patterns (LBP) [85, 86] as well as color and location are densely computed. Given an initial set of ~ 150 candidate figure-ground masks for the image — produced using the bottom-up CPMC segmentation algorithm [16] — the second-order statistics (*i.e.* vector outer-products) of local descriptors that fall within each region are pooled (*e.g.* average/max) to give *global* features capturing higher-order interactions between image elements. These *region-level* features are fed to support-vector regressors (SVR) for each category, that are trained to predict how well the region overlaps objects of that category.

The implementation uses a simple and efficient greedy inference strategy to produce the final multi-category segmentation. Starting with an initial background threshold, in decreasing order, the segment and category with highest score above the threshold is pasted in the image. Segments with higher score are laid on top of segments with lower score. Each time a segment is pasted the background threshold is increased, and the process stops when there are no more segments with category score above the threshold. The initial background threshold is set such that the average number of segments with score above the threshold is roughly the same as the number of objects per image in the training set. Note that we can reformulate this approach as a CRF constructed on overlapping CPMC segments in the image with unary potentials defined by the SVR category scores of each segment.

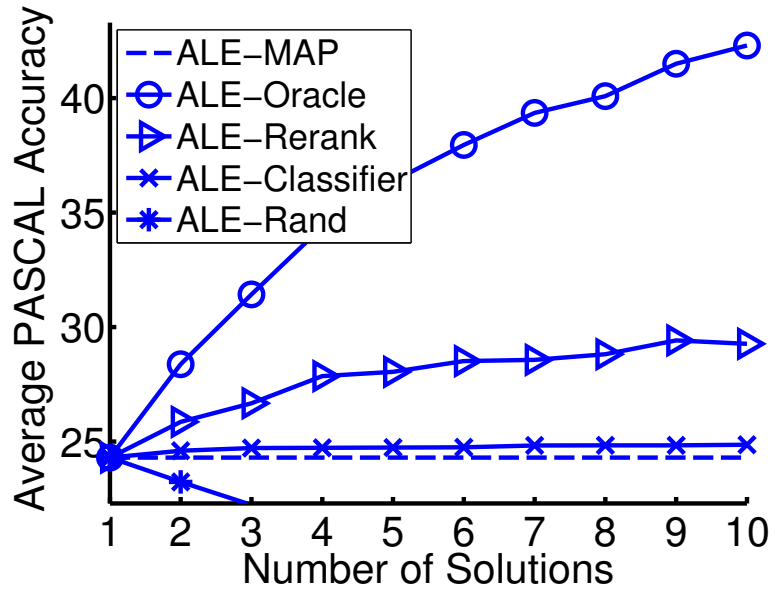
Through the use of a number of tricks to speedup computation, like caching pooling results and dimensionality reduction on features (*cf.* [17]), the O_2P implementation is faster to train and run inference over than the ALE model.

5.3.4 Diversity and Oracles

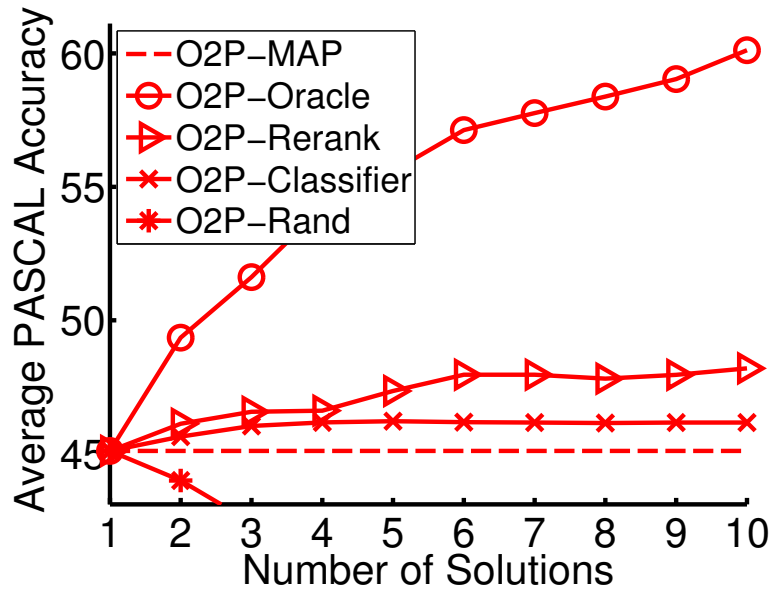
For the analysis reported in this subsection, we used the VOC 2012 train and val sets. ALE and O_2P models were trained on VOC 2012 train, and the models were used to produce 10 segmentations for each image in val. The Lagrangian multiplier in the *DivMBEST* formulation (*cf.* § 2.2.6) was tuned via cross-val ($\lambda_{ALE} = 1.25$ and $\lambda_{O_2P} = 0.08$).

Oracle Accuracies. Since ground-truth is known for VOC val images, we can find the *oracle* accuracy, *i.e.* the accuracy of the best solution in the set, as described in § 4.1.2. This accuracy is shown in figure 5.1 (lines with circles): with 10 solutions on O_2P , it reaches 60.12%, which is 15%-points higher the accuracy of MAP. *Oracle* accuracy with ALE solutions show a similar increase w.r.t. ALE’s MAP.

To put these *oracle* numbers in context, we can try to find what is the best segmentation accuracy achievable using the 150 CPMC segments for each image. To find a good approximation of the best segmentation we can achieve, we can consider a greedy algorithm that tries to find the subset of CPMC segments that best cover ground-truth



(a)



(b)

Figure 5.1: *DivMBEST+ReRANK* performance on PASCAL VOC 2012 val using (a) ALE and (b) O₂P models vs. the number of solutions.

segments and then simply copies labels over from the ground-truth. This achieves an accuracy of 80.78%. Notice that this procedure takes the supremum of accuracy of *exponentially* many solutions, whereas *DivMBEST* with 10 solutions reaches 60.12%, closing the gap to within 21% points.

Diversity of solutions. We now turn to empirical analysis that quantifies the amount of diversity in these solutions, and how that affects the oracle performance.

The first question to address is: how much diversity do the DivMBEST solutions contain over MAP? To answer this, we can look at the solution in the set that is most different from MAP, as measured by average region overlap.

Let $\{s_{i,1}^{(m)}, \dots, s_{i,K}^{(m)}\}$ denote the set of K segments in the m^{th} solution for image i and $\{s_{i,1}^{(1)}, \dots, s_{i,K}^{(1)}\}$ denote the set of segments in MAP. We can define a category-independent *covering measure*, which for a given image i captures how much of the MAP segmentation is covered by one of the subsequent solutions,

$$D_1(\mathbf{y}_i^{(j)}) = \frac{1}{\sum_{k'} |s_{i,k'}^{(1)}|} \sum_{k'=1}^{K'} |s_{i,k'}^{(1)}| \max_{k \in [K]} O(s_{i,k'}, s_{i,k}^{(j)}), \quad (5.2)$$

where $|s_{i,k}^{(m)}|$ denotes the size of the segment and $O(\cdot, \cdot)$ is the intersection-over-union measure of the two segments. For O_2P these segments correspond to CPMC segments [16], while in ALE the segments are connected components in the segmentation.

To get an idea of how different the *most* diverse solution is, we can define the minimum cover of the MAP solution by the M segmentations for image i as:

$$D_1^{(i,m)} \doteq \min_{j=1, \dots, m} \{D_1(\mathbf{y}_i^{(j)})\}. \quad (5.3)$$

A plot of average minimum diversity in the dataset, *i.e.* $\sum_i D_1^{(i,m)} / n$ for $m = 1, \dots, 10$ is shown in figure 5.2a. We can see that both models produce at least one solution that is significantly different from the MAP. With 10 solutions, the minimum covering of MAP drops to about 0.3 for O_2P and 0.1 for ALE. Thus, on average at least one out of 10 *DivMBEST* solutions for O_2P overlaps MAP by only 10%.

Diversity of Oracle. Of course, diversity is useful only if it brings improved quality. The previous measure simply captures diversity and can be easily affected by poor quality solutions that are different from MAP. We can also try to characterize the diversity in the oracle solutions. This measure tells us how different the oracle solution is from the MAP solution on average. Analogous to eqn. 5.2 we can compute $D_1(\mathbf{y}_i^{(*)})$ to measure by how much the segments in the oracle segmentation cover the MAP segments. We can also use a category-specific covering measure which takes into account label agreement to get a measure of how much the MAP segments are covered with same labelled segments in the oracle solution,

$$D_2(\mathbf{y}_i^{(*)}) = \frac{1}{\sum_{k'} |s_{i,k'}^{(1)}|} \sum_{k'=1}^{K'} |s_{i,k'}^{(1)}| \max_{\substack{k \in [K]: \\ \mathbf{y}_{i,k}^{(*)} = \mathbf{y}_{i,k}^{(1)}}} O(s_{i,k'}, s_{i,k}^*), \quad (5.4)$$

	D_1 Oracle Covering	D_2 Oracle Covering
ALE	0.55	0.45
O ₂ P	0.61	0.58

Table 5.3: Average covering score between oracle solutions and MAP: (*left*) show the category-independent measure and (*right*) shows the category-specific measure.

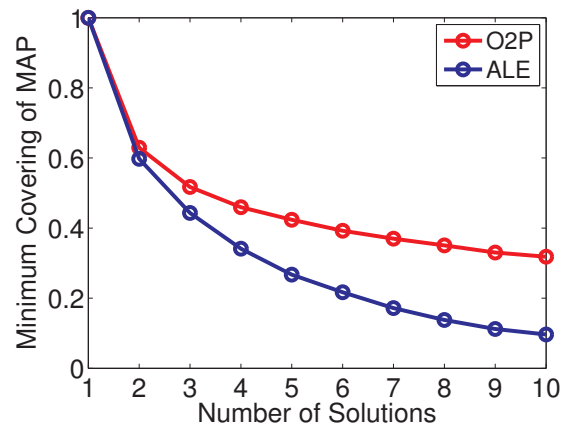
where $y_{i,k}^{(*)}$ and $y_{i,k'}^{(1)}$ are the labels of the oracle and MAP segments respectively. Table 5.3 summarizes these results which show that the oracle segmentations are not simply minor perturbations of the MAP segmentations. On average the MAP covering by oracle irrespective of segment label is less than 61% for O₂P and 55% for ALE. If we constrain the covering to be category-consistent, these numbers drop to 58% and 45% respectively. Thus, we can conclude that the oracle segmentations are not simply minor perturbations of the MAP.

Gain from diversity.

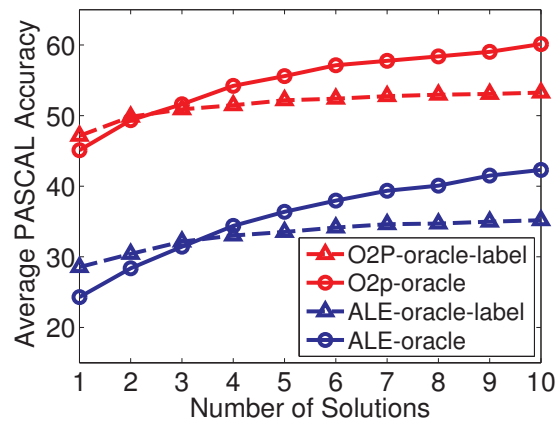
The previous measure tells us that the oracle solution is indeed quite different from the MAP. We now try to study *how* it is different – do the additional solutions introduce new categories or new masks or both? In order to answer this question, we measure the performance of a restricted *oracle* that chooses in each additional solution the best label possible for all segments, albeit restricted to the set of labels found in MAP. Specifically, if a segment $s_{i,k}^{(j)}$ overlaps with the ground-truth background by more than 50%, then we set its label to background. Otherwise if there is a segment $g_{i,l} \in \mathbf{y}_i^{\text{gt}}$, where $y(g_{i,l}) \in \mathbf{y}_{\text{MAP}}$ (where $\mathbf{y}_{\text{MAP}} \doteq \{y(s_{i,k}^{(1)}) | k \in [K]\}$), with $s_{i,k}^{(j)} \cap g_{i,l} \neq \emptyset$, we set $y(s_{i,k}^{(j)}) = y(g_{i,l})$. If there is no such $g_{i,l}$ then $y(s_{i,k}^{(j)})$ is assigned a random label from \mathbf{y}_{MAP} . Figure 5.2b shows that such a restricted oracle (O₂P-oracle-label and ALE-oracle-label) performs worse than the unrestricted oracle, indicating that the additional solutions do in fact introduce categories present in ground-truth but not in MAP.

Similarly, we can restrict the oracle to only take segment masks found in MAP and assign to them the best possible labels found in $\mathbf{y}_i^{(m)}$. Again figure 5.2c shows that such a restricted oracle significantly under-performs, indicating the MAP masks are not ideal and that the additional solutions do in fact introduce useful masks.

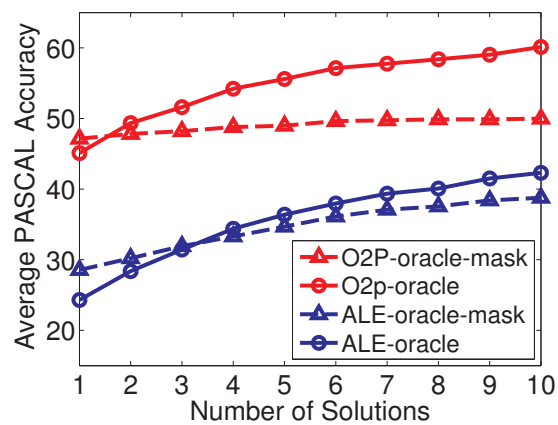
Thus, we can conclude that there are clear differences in both the labels and segments of the oracle segmentations compared to the MAP.



(a)



(b)



(c)

Figure 5.2: (a) Average minimum-covering (5.3) of MAP in the first $j \leq 10$ solutions vs. j . (b) Accuracy of an oracle restricted to labels present in the MAP, or (c) restricted to masks present in MAP. See text for details.

	Backgr.	Plane	Bicycle	Bird	Boat	Bottle	Bus	Car	Cat	Chair	Cow	D.Table	Dog	Horse	M.bike	Person	Plant	Sheep	Sofa	Train	TV.Mo.	Average
O ₂ P-MAP	84.8	63.7	23.4	44.9	40.8	45.1	58.0	58.8	57.6	12.1	43.8	31.0	44.8	56.2	56.8	52.3	37.1	44.0	29.5	48.6	42.9	46.5
DivMBEST+ReRANK	85.7	62.7	25.6	46.9	43.0	54.8	58.4	58.6	55.6	14.6	47.5	31.2	44.7	51.0	60.9	53.5	36.6	50.9	30.1	50.2	46.8	48.1

Table 5.4: PASCAL VOC 2012 test set accuracies.

5.3.5 Re-ranker features

Our re-ranker uses a number of features that we separate into a few groups. In the discussion, below we say a label c is present in \mathbf{y} if at least one pixel in \mathbf{y} is labeled c .

Model features rely on properties derived from the model that produced segmentation \mathbf{y} – model score of \mathbf{y} , average pixel score, number of CPMC masks used to construct foreground, the final background threshold at the end of the greedy foreground assembly, and the rank of \mathbf{y} among the m diverse hypotheses for the given input image. (5 dimensions)

Diversity features measure average per pixel agreement of \mathbf{y} with the majority vote by the diverse set (weighted or unweighted by the model scores). (2 dimensions)

Recognition features. We use outputs of object detectors from [83] to get detector-based segmentations $\mathcal{D}_1, \mathcal{D}_2$, where each pixel is assigned by majority vote on detection scores (thresholded & un-thresholded). Then we compute the agreement matrix: for every c_1, c_2 we count pixels assigned to c_1 by \mathbf{y} and to c_2 by \mathcal{D}_1 , yielding a 441-dimensional feature. We compute max/median/min of the detection score (with and without thresholding) for every category in \mathbf{y} (120 dims); the average overlap between category masks in $\mathcal{D}_1, \mathcal{D}_2$ and in \mathbf{y} (2 dims); and pixelwise average detector scores for categories in \mathbf{y} (2 dims). We also use the the estimated posterior for each category present in \mathbf{y} , using the classifier from [115] (20 dimensions).

Segment features measure the geometric properties of the segments in \mathbf{y} : perimeter, area, and the ratio of the two; computed separately for segments in every class and for the entire foreground (63 dimensions). Relative location of the centroids of masks for each category pair (420 dimensions).

Label features rely on information regarding the labels assigned to masks in \mathbf{y} , but not the geometry of these masks. For every pair of labels c_1, c_2 we compute the binary co-occurrence (1 if both categories are present in \mathbf{y}) and the percentage of pixels assigned to c_1 & c_2 . (420 dimensions)

All the features above are independent of the image x ; the following features rely on image measurements as well as properties of the solution \mathbf{y} .

Boundary features. We compute the total globalPb probability of boundary response [3] in a band along the category boundaries; for 3 widths of the band, this produces a 3-dimensional feature (with 3 more for normalized versions). We also compute recall by the globalPb map of the category boundaries in the \mathbf{y} ; this produces a 10 dimensional feature for ten equally spaced precision values. Finally, we compute the histogram (6 bins) of Chamfer distance between the boundaries in \mathbf{y} and the thresholded globalPb, and vice versa; with 10 thresholds this produces a 120 dimensional feature. For each category, we also computed normalized histogram of globalPb responses in the non-boundary regions (210 dims).

Entropy features. For every category (and the combined foreground) we measure the entropy of color histograms, computed per color channel with two binning resolutions, yielding 126 dimensions. We do the same for textons [106, 107], with a single binning, for another 21 features.

We stress that most of these features rely on higher-order information that would be intractable to incorporate into the CRF model used in stage 1. For instance, using features that refer to segment boundaries is hard in CRF. However, evaluating these features on m segmentations is easy, which allows us to use them at the re-ranking stage.

5.3.6 Re-ranker training

The combined feature vector per solution \mathbf{y} has 1988 dimensions. The only hyperparameter for the re-ranker is the regularization parameter C (3.11), which is chosen via cross-validation on the val set⁹.

One important practical question is how many diverse solutions to use. While we have seen above that the oracle accuracy increases through $M = 30$ solutions, it is possible that too many solutions make it hard to train an effective re-ranker. Indeed, we found that the best results in cross-validation are obtained when training on 10 solutions per image; we use the same number of diverse solutions per image when re-ranking the test segmentations.

5.3.7 Re-ranker results

The performance of the *DivMBEST+RERANK* pipeline on the O_2P and ALE models (Rerank), as the size of the *DivMBEST* set grows, is reported in figure 5.1 along with MAP and *oracle* accuracies. The plot also shows results of a binary classifier baseline (Classifier) that is trained to discriminate between the best and worst segmentations

⁹ We also used cross-validation to evaluate the feature set, rejecting some additional features not listed here that did not contribute to re-ranking accuracy.

	Binary Task Accuracies			Pascal VOC Avg. Acc.			
	B-vs-W	M-vs-W	B-vs-M	<i>Best</i>	MAP	<i>Worst</i>	HR
ALE	71.9	64.4	61.7	38.0	19.1	3.2	20.5
O ₂ P	73.9	73.1	56.3	62.8	43.6	24.5	49.0

Table 5.5: (left) Human accuracy in predicting (*B*)est-vs-(*W*)orst, (M)AP-vs-(*W*)orst, and (*B*)est-vs-(M)AP solutions. (right) Pascal VOC accuracies over 150 images for best, MAP, worst, and human response (HR) solutions.

in the set, and used at test time to re-rank according to classification score. As a second baseline, we compare against randomly picking one out of the $j \leq m$ segmentations (Rand).

On PASCAL VOC 2012 val, the MAP segmentation IoU accuracy is 24.3% on ALE and 45.1% on O₂P. In contrast *Div*MBEST+REERANK achieves 29.27% on ALE and 48.2% on O₂P, an increase of > 5% and > 3%-points respectively. Table 5.4 shows VOC 2012 test set performance of the O₂P ranker when trained on the val set. O₂P-*Div*MBEST+REERANK achieves a 1.6%-point performance improvement over O₂P-MAP¹⁰. A few examples where O₂P-*Div*MBEST+REERANK beats O₂P-MAP are shown in figure 5.4. More examples can be found in Appendix B.2.

¹⁰ this was state-of-the-art results on PASCAL VOC 2012 comp6 challenge at time of experiments

5.3.8 Re-ranker Analysis

We can consider how the re-ranker behaves in picking a solution from the *Div*MBEST set. In the original ranking of *Div*MBEST solutions (*i.e.* order in which they were generated) figure 5.3a shows the number of images in which the *oracle* solution is at rank j , for $j \in \{1, \dots, 10\}$. The *oracle* distribution has a heavy tail, indicating that high-quality solutions are often found at the bottom of the list. Figure 5.3b shows the number of images where the top re-ranked solution was originally at rank j . The re-ranked distribution has a much lighter tail which suggest that the re-ranker "plays it safe" and often predicts MAP. The correlation between segmentation quality and re-ranker score is shown in figure 5.3c, which indicates that the re-ranker score is well correlated with solution quality.

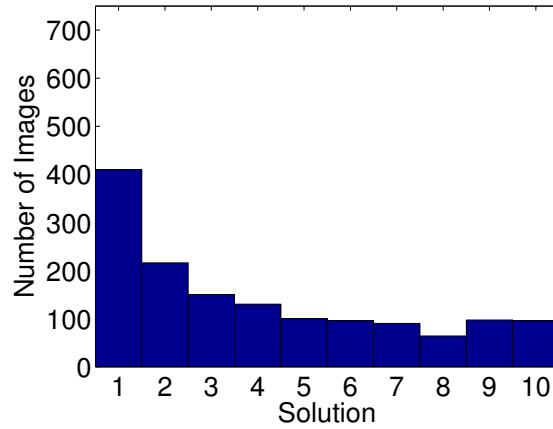
5.3.9 Human Ranking Experiments

To evaluate and characterize the difficulty of the re-ranking problem we can investigate how well people perform the task of picking a good segmentation — which symbolizes the gold standard. 150 images were chosen from PASCAL VOC 2012 val set where

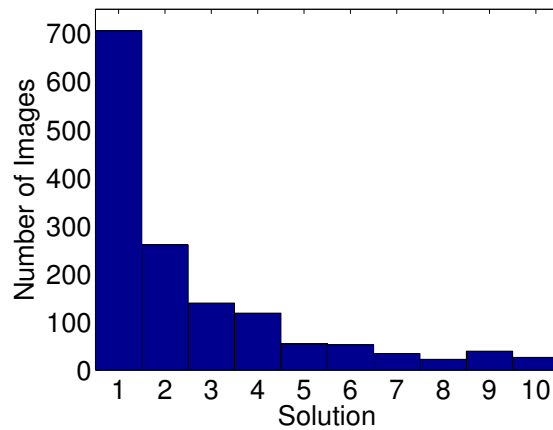
the MAP segmentation was neither the worst nor best segmentation. On Amazon Mechanical Turk (AMT), subjects were presented with three different types of binary comparison tasks for each image: comparing *Best-vs-MAP*, *Best-vs-Worst*, and *MAP-vs-Worst* segmentations in the *DivMBEST* set. The subjects had to make the choice using only the labellings (with category names annotated) and *not* the image. The subjects were also presented with the option to provide feedback on reasons for their choice. Figure 5.5 shows the interface with actual examples of results from AMT workers. The workers' comments illustrate that people are very good at discriminating good versus bad segmentations using cues such as category co-occurrence (figure 5.5a), category shape (figure 5.5b), and part-vs-whole relationships (figure 5.5c). These cues provide evidence for our choice of re-ranker features. A summary of how well subjects did on the three tasks is shown in Table 5.5. The most difficult binary task for subjects was choosing between *Best* and MAP segmentations. In the case of the O_2P model picking between MAP and *Best* is even more difficult than for ALE because the MAP solutions are better for the O_2P model. Note that the segmentations picked by humans (HR) achieve substantial improvement over MAP, which is significant given that the choice is made without seeing the original image.

5.3.10 Summary

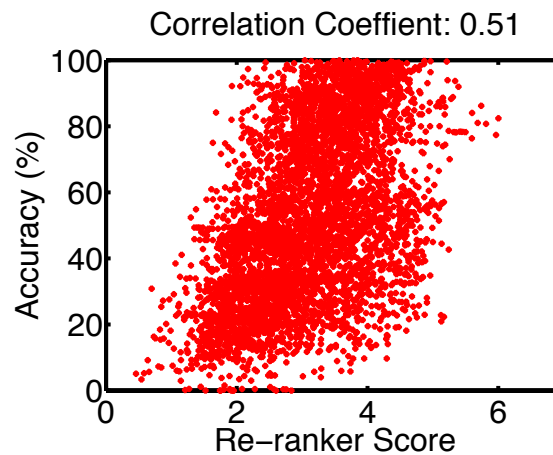
The analysis in this section on a number of segmentation tasks shows that the set of solutions obtained from the *DivMBEST* stage are of significantly higher quality than the MAP solutions. The source of diversity between solutions is also non-trivial. Re-ranking the *DivMBEST* set results in significant performance improvement over MAP. The results also highlight the importance of choosing re-ranking features that can discriminate good versus bad solutions within the *DivMBEST* set. Learning rich features for the within set discrimination task is an area for future research.



(a) Oracle Solution Rank Histogram.



(b) Predicted Solution Rank Histogram.

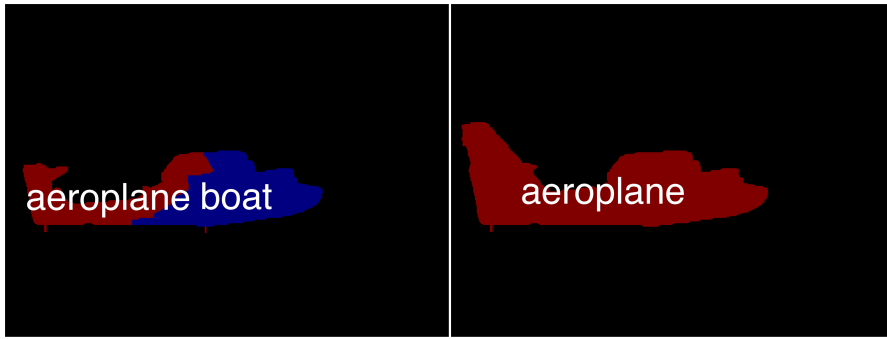


(c) Re-ranker Score vs Solution Accuracy.

Figure 5.3: Statistics on PASCAL VOC 2012 val with O_2P model: (a),(b) show the number of images in which the *oracle* / top-re-ranked solution was originally at rank $j \leq 10$. We can see that there is a heavy tail in the oracle distribution, but a much lighter tail in the re-ranker, suggesting that the re-ranker “plays it safe” and predicts MAP very frequently; (c) shows a scatter plot of re-ranker score vs solution accuracy.



Figure 5.4: Cases where O_2P -*DivMBEST*+*ReRANK* outperforms O_2P -*MAP*. In each group of images, the first column shows the original image followed by the ground-truth, *MAP*, and top re-ranked solution returned by *DivMBEST*+*ReRANK*. PASCAL intersection-over-union accuracy is shown below the segmentations.

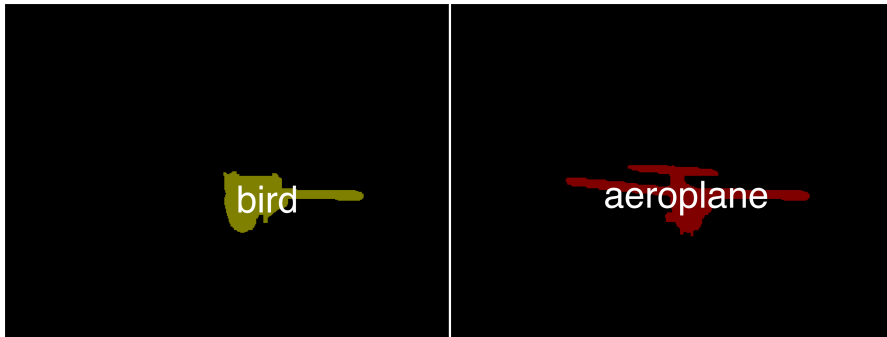


Which labeling is better?

Left Right

The image on the right makes more sense as a boat would hardly be next to a plane.

(a)



Which labeling is better?

Left Right

The image on the right is clearly shaped like a plane.

(b)



Which labeling is better?

Left Right

The image on the left seems like its clearer as you can see the wheels of the bike.

(c)

Figure 5.5: Example MTurk tasks along with user-provided responses which were instructive in the creation of segmentation-specific features.

CONCLUSION

In summary, this thesis presents an approach to obtaining performance gains from a semantic segmentation model. Instead of achieving gains by opting for a more complex model which would be more expensive or possibly intractable to optimize over the gains are achieved through a careful redesign of the inference procedure that leverages diversity between output labellings. The thesis also outlines an approach to ranking these *DivMBEST* segmentations to automatically pick the best from the set. It contains the following contributions:

- A framework (*DivMBEST*) for inferring multiple highly probable yet diverse segmentations from a probabilistic structured output model. It is motivated and derived from the integer programming problem for solving inference on probabilistic graphical models with discrete output space. The *DivMBEST* framework is generally applicable in any setting where you have an inference model over a structured output label distribution. What results is an elegant and practical iterative algorithm for inference that is more akin to finding *modes* of the output space distribution. It reuses the inference procedure from the original model, providing means for improved prediction without incurring any cost in tractability.
- The *DivMBEST* formulation can accept different measures of diversity between “modes”, such as Hamming and cardinality distance. Finding *modes* of a CRF under Hamming dissimilarity amounts to only modifying the unary energy terms and reusing the same MAP inference machinery to compute subsequent solutions, yielding an approach that is as efficient as the underlying MAP inference algorithm.
- A discriminative large margin approach to ranking the *DivMBEST* segmentations (*DivMBEST+ReRANK*) is introduced that allows for arbitrarily complex features to evaluate each segmentation.
- Evaluation of the *DivMBEST* and *DivMBEST+ReRANK* algorithms on a number of semantic image labelling problems including interactive, figure-ground, and multi-category segmentation. The results provide evidence of the benefits these approaches offer for the segmentation task.

- Oracle experiments on semantic segmentation show that the *DivMBEST* approach has the potential to achieve results comparable or better than even existing state-of-the-art CNN models for segmentation.
- Application of the *DivMBEST* framework to present CNN+dense CRF models for segmentation which shows that the *DivMBEST* and *DivMBEST+RE-RANK* algorithms are very much relevant to the current trends in semantic segmentation.

BIBLIOGRAPHY

- [1] Radhakrishna Achanta, Appu Shaji, Kevin Smith, Aurelien Lucchi, Pascal Fua, and Sabine Süsstrunk. *Slic superpixels*. Tech. rep. 2010.
- [2] Andrew Adams, Jongmin Baek, and Myers Abraham Davis. "Fast High-Dimensional Filtering Using the Permutohedral Lattice." In: *Computer Graphics Forum*. Vol. 29. 2. Wiley Online Library. 2010, pp. 753–762.
- [3] Pablo Arbelaez, Michael Maire, Charless Fowlkes, and Jitendra Malik. "Contour detection and hierarchical image segmentation." In: *IEEE transactions on pattern analysis and machine intelligence* 33.5 (2011), pp. 898–916.
- [4] Pablo Arbeláez, Bharath Hariharan, Chunhui Gu, Saurabh Gupta, Lubomir Bourdev, and Jitendra Malik. "Semantic segmentation using regions and parts." In: *Computer Vision and Pattern Recognition (CVPR), 2012 IEEE Conference on*. IEEE. 2012, pp. 3378–3385.
- [5] Adrian Barbu and Song-Chun Zhu. "Generalizing Swendsen-Wang to sampling arbitrary posterior probabilities." In: *IEEE Transactions on Pattern Analysis and Machine Intelligence* 27.8 (2005), pp. 1239–1253.
- [6] Dhruv Batra, Adarsh Kowdle, Devi Parikh, Jiebo Luo, and Tsuhan Chen. "icoseg: Interactive co-segmentation with intelligent scribble guidance." In: *Computer Vision and Pattern Recognition (CVPR), 2010 IEEE Conference on*. IEEE. 2010, pp. 3169–3176.
- [7] Dhruv Batra, Payman Yadollahpour, Abner Guzman-Rivera, and Gregory Shakhnarovich. "Diverse m-best solutions in markov random fields." In: *European Conference on Computer Vision*. Springer. 2012, pp. 1–16.
- [8] Dimitri P Bertsekas. *Nonlinear programming*. Athena scientific Belmont, 1999.
- [9] Xavier Boix, Josep M Gonfaus, Joost Van de Weijer, Andrew D Bagdanov, Joan Serrat, and Jordi González. "Harmony potentials." In: *International journal of computer vision* 96.1 (2012), pp. 83–102.
- [10] Eran Borenstein and Shimon Ullman. "Combined top-down/bottom-up segmentation." In: *IEEE Transactions on pattern analysis and machine intelligence* 30.12 (2008), pp. 2109–2125.
- [11] Stephen Boyd and Lieven Vandenberghe. *Convex optimization*. Cambridge university press, 2004.

- [12] Yuri Y Boykov and M-P Jolly. "Interactive graph cuts for optimal boundary & region segmentation of objects in ND images." In: *Computer Vision, 2001. ICCV 2001. Proceedings. Eighth IEEE International Conference on*. Vol. 1. IEEE. 2001, pp. 105–112.
- [13] Yuri Boykov and Vladimir Kolmogorov. "An experimental comparison of min-cut/max-flow algorithms for energy minimization in vision." In: *IEEE transactions on pattern analysis and machine intelligence* 26.9 (2004), pp. 1124–1137.
- [14] Jaime Carbonell and Jade Goldstein. "The use of MMR, diversity-based reranking for reordering documents and producing summaries." In: *Proceedings of the 21st annual international ACM SIGIR conference on Research and development in information retrieval*. ACM. 1998, pp. 335–336.
- [15] João Carreira, Fuxin Li, and Cristian Sminchisescu. "Object recognition by sequential figure-ground ranking." In: *International journal of computer vision* 98.3 (2012), pp. 243–262.
- [16] Joao Carreira and Cristian Sminchisescu. "Constrained parametric min-cuts for automatic object segmentation." In: *Computer Vision and Pattern Recognition (CVPR), 2010 IEEE Conference on*. IEEE. 2010, pp. 3241–3248.
- [17] Joao Carreira, Rui Caseiro, Jorge Batista, and Cristian Sminchisescu. "Semantic segmentation with second-order pooling." In: *European Conference on Computer Vision*. Springer. 2012, pp. 430–443.
- [18] Liang-Chieh Chen, George Papandreou, Iasonas Kokkinos, Kevin Murphy, and Alan L Yuille. "Semantic image segmentation with deep convolutional nets and fully connected crfs." In: *arXiv preprint arXiv:1412.7062* (2014).
- [19] Liang-Chieh Chen, George Papandreou, Iasonas Kokkinos, Kevin Murphy, and Alan L Yuille. "Deeplab: Semantic image segmentation with deep convolutional nets, atrous convolution, and fully connected crfs." In: *arXiv preprint arXiv:1606.00915* (2016).
- [20] Yizong Cheng. "Mean shift, mode seeking, and clustering." In: *IEEE transactions on pattern analysis and machine intelligence* 17.8 (1995), pp. 790–799.
- [21] Michael Collins and Terry Koo. "Discriminative reranking for natural language parsing." In: *Computational Linguistics* 31.1 (2005), pp. 25–70.
- [22] Michael Collins, Brian Roark, and Murat Saraclar. "Discriminative syntactic language modeling for speech recognition." In: *Proceedings of the 43rd Annual Meeting on Association for Computational Linguistics*. Association for Computational Linguistics. 2005, pp. 507–514.
- [23] Dorin Comaniciu and Peter Meer. "Mean shift: A robust approach toward feature space analysis." In: *IEEE Transactions on pattern analysis and machine intelligence* 24.5 (2002), pp. 603–619.

- [24] Navneet Dalal and Bill Triggs. "Histograms of oriented gradients for human detection." In: *Computer Vision and Pattern Recognition, 2005. CVPR 2005. IEEE Computer Society Conference on*. Vol. 1. IEEE. 2005, pp. 886–893.
- [25] A Philip Dawid. "Applications of a general propagation algorithm for probabilistic expert systems." In: *Statistics and computing* 2.1 (1992), pp. 25–36.
- [26] Marco Dinarelli, Alessandro Moschitti, and Giuseppe Riccardi. "Discriminative reranking for spoken language understanding." In: *IEEE Transactions on Audio, Speech, and Language Processing* 20.2 (2012), pp. 526–539.
- [27] Ian Endres and Derek Hoiem. "Category independent object proposals." In: *European Conference on Computer Vision*. Springer. 2010, pp. 575–588.
- [28] Ian Endres and Derek Hoiem. "Category-independent object proposals with diverse ranking." In: *IEEE transactions on pattern analysis and machine intelligence* 36.2 (2014), pp. 222–234.
- [29] Mark Everingham, Luc Van Gool, Christopher KI Williams, John Winn, and Andrew Zisserman. "The pascal visual object classes (voc) challenge." In: *International journal of computer vision* 88.2 (2010), pp. 303–338.
- [30] Pedro F Felzenszwalb and Daniel P Huttenlocher. "Efficient graph-based image segmentation." In: *International journal of computer vision* 59.2 (2004), pp. 167–181.
- [31] Pedro F Felzenszwalb, Ross B Girshick, David McAllester, and Deva Ramanan. "Object detection with discriminatively trained part-based models." In: *IEEE transactions on pattern analysis and machine intelligence* 32.9 (2010), pp. 1627–1645.
- [32] Yoav Freund and Robert E Schapire. "A decision-theoretic generalization of on-line learning and an application to boosting." In: *European conference on computational learning theory*. Springer. 1995, pp. 23–37.
- [33] Yoav Freund, Robert Schapire, and Naoki Abe. "A short introduction to boosting." In: *Journal-Japanese Society For Artificial Intelligence* 14.771-780 (1999), p. 1612.
- [34] Menachem Fromer and Amir Globerson. "An LP View of the M-best MAP problem." In: *Advances in Neural Information Processing Systems*. 2009, pp. 567–575.
- [35] Keinosuke Fukunaga and Larry Hostetler. "The estimation of the gradient of a density function, with applications in pattern recognition." In: *IEEE Transactions on information theory* 21.1 (1975), pp. 32–40.
- [36] Arthur M Geoffrion. "Lagrangian relaxation for integer programming." In: *Approaches to integer programming*. Springer, 1974, pp. 82–114.
- [37] Chunhui Gu, Joseph J Lim, Pablo Arbeláez, and Jitendra Malik. "Recognition using regions." In: *Computer Vision and Pattern Recognition, 2009. CVPR 2009. IEEE Conference on*. IEEE. 2009, pp. 1030–1037.
- [38] Monique Guignard. "Lagrangian relaxation." In: *Top* 11.2 (2003), pp. 151–200.

- [39] Rahul Gupta, Sunita Sarawagi, and Ajit A Diwan. "Collective inference for extraction mrfs coupled with symmetric clique potentials." In: *Journal of Machine Learning Research* 11.Nov (2010), pp. 3097–3135.
- [40] Saurabh Gupta, Ross Girshick, Pablo Arbeláez, and Jitendra Malik. "Learning rich features from RGB-D images for object detection and segmentation." In: *European Conference on Computer Vision*. Springer. 2014, pp. 345–360.
- [41] Bharath Hariharan, Pablo Arbelaez, Lubomir Bourdev, Subhransu Maji, and Jitendra Malik. "Semantic Contours from Inverse Detectors." In: *International Conference on Computer Vision (ICCV)*. 2011.
- [42] Bharath Hariharan, Pablo Arbeláez, Ross Girshick, and Jitendra Malik. "Hypercolumns for object segmentation and fine-grained localization." In: *Proceedings of the IEEE Conference on Computer Vision and Pattern Recognition*. 2015, pp. 447–456.
- [43] Kaiming He, Xiangyu Zhang, Shaoqing Ren, and Jian Sun. "Deep residual learning for image recognition." In: *Proceedings of the IEEE Conference on Computer Vision and Pattern Recognition*. 2016, pp. 770–778.
- [44] Derek Hoiem, Alexei A Efros, and Martial Hebert. "Geometric context from a single image." In: *Computer Vision, 2005. ICCV 2005. Tenth IEEE International Conference on*. Vol. 1. IEEE. 2005, pp. 654–661.
- [45] Derek Hoiem, Andrew N Stein, Alexei A Efros, and Martial Hebert. "Recovering occlusion boundaries from a single image." In: *Computer Vision, 2007. ICCV 2007. IEEE 11th International Conference on*. IEEE. 2007, pp. 1–8.
- [46] IBM, Inc. *IBM ILOG CPLEX: High-performance mathematical programming solver for linear programming, mixed integer programming, and quadratic programming*. See <https://www-01.ibm.com/software/commerce/optimization/cplex-optimizer/>. 2017.
- [47] Finn V Jensen, Steffen L Lauritzen, and Kristian G Olesen. "Bayesian updating in causal probabilistic networks by local computations." In: *Computational statistics quarterly* 4 (1990), pp. 269–282.
- [48] Thorsten Joachims, Thomas Finley, and Chun-Nam John Yu. "Cutting-plane training of structural SVMs." In: *Machine Learning* 77.1 (2009), pp. 27–59.
- [49] Jaechul Kim and Kristen Grauman. "Shape sharing for object segmentation." In: *European Conference on Computer Vision*. Springer. 2012, pp. 444–458.
- [50] Alexander Kirillov, Bogdan Savchynskyy, Dmitrij Schlesinger, Dmitry Vetrov, and Carsten Rother. "Inferring M-best diverse labelings in a single one." In: *Proceedings of the IEEE International Conference on Computer Vision*. 2015, pp. 1814–1822.

- [51] Alexander Kirillov, Dmytro Shlezinger, Dmitry P Vetrov, Carsten Rother, and Bogdan Savchynskyy. "M-best-diverse labelings for submodular energies and beyond." In: *Advances in Neural Information Processing Systems*. 2015, pp. 613–621.
- [52] Alexander Kirillov, Alexander Shekhovtsov, Carsten Rother, and Bogdan Savchynskyy. "Joint M-Best-Diverse Labelings as a Parametric Submodular Minimization." In: *Advances in Neural Information Processing Systems*. 2016, pp. 334–342.
- [53] Timo Kohlberger, Vivek Singh, Chris Alvino, Claus Bahlmann, and Leo Grady. "Evaluating segmentation error without ground truth." In: *International Conference on Medical Image Computing and Computer-Assisted Intervention*. Springer. 2012, pp. 528–536.
- [54] Pushmeet Kohli and M Pawan Kumar. "Energy minimization for linear envelope MRFs." In: *Computer Vision and Pattern Recognition (CVPR), 2010 IEEE Conference on*. IEEE. 2010, pp. 1863–1870.
- [55] Pushmeet Kohli, M Pawan Kumar, and Philip HS Torr. "P₃ & beyond: Solving energies with higher order cliques." In: *Computer Vision and Pattern Recognition, 2007. CVPR'07. IEEE Conference on*. IEEE. 2007, pp. 1–8.
- [56] Pushmeet Kohli, M Pawan Kumar, and Philip HS Torr. "P³ & Beyond: Move Making Algorithms for Solving Higher Order Functions." In: *IEEE Transactions on Pattern Analysis and Machine Intelligence* 31.9 (2009), pp. 1645–1656.
- [57] Pushmeet Kohli and Philip HS Torr. "Efficiently solving dynamic markov random fields using graph cuts." In: *Tenth IEEE International Conference on Computer Vision (ICCV'05) Volume 1*. Vol. 2. IEEE. 2005, pp. 922–929.
- [58] Pushmeet Kohli and Philip HS Torr. "Measuring uncertainty in graph cut solutions." In: *Computer Vision and Image Understanding* 112.1 (2008), pp. 30–38.
- [59] Pushmeet Kohli, Philip HS Torr, et al. "Robust higher order potentials for enforcing label consistency." In: *International Journal of Computer Vision* 82.3 (2009), pp. 302–324.
- [60] Pushmeet Kohli, Philip HS Torr, et al. "Robust higher order potentials for enforcing label consistency." In: *International Journal of Computer Vision* 82.3 (2009), pp. 302–324.
- [61] Daphne Koller and Nir Friedman. *Probabilistic graphical models: principles and techniques*. MIT press, 2009.
- [62] Vladimir Kolmogorov and Ramin Zabini. "What energy functions can be minimized via graph cuts?" In: *IEEE transactions on pattern analysis and machine intelligence* 26.2 (2004), pp. 147–159.
- [63] Nikos Komodakis and Nikos Paragios. "Beyond pairwise energies: Efficient optimization for higher-order MRFs." In: *Computer Vision and Pattern Recognition, 2009. CVPR 2009. IEEE Conference on*. IEEE. 2009, pp. 2985–2992.

- [64] Nikos Komodakis, Nikos Paragios, and Georgios Tziritas. "MRF optimization via dual decomposition: Message-passing revisited." In: *2007 IEEE 11th International Conference on Computer Vision*. IEEE. 2007, pp. 1–8.
- [65] Philipp Krähenbühl and Vladlen Koltun. "Efficient Inference in Fully Connected CRFs with Gaussian Edge Potentials." In: *NIPS*. 2011.
- [66] Daniel Kuettel and Vittorio Ferrari. "Figure-ground segmentation by transferring window masks." In: *Computer Vision and Pattern Recognition (CVPR), 2012 IEEE Conference on*. IEEE. 2012, pp. 558–565.
- [67] L'ubor Ladickÿ and Philip HS Torr. *The Automatic Labelling Environment*. 2012.
- [68] L'ubor Ladickÿ, Chris Russell, Pushmeet Kohli, Philip HS Torr, et al. "Associative hierarchical crfs for object class image segmentation." In: *Computer Vision, 2009 IEEE 12th International Conference on*. IEEE. 2009, pp. 739–746.
- [69] L'ubor Ladickÿ, Chris Russell, Pushmeet Kohli, and Philip HS Torr. "Graph cut based inference with co-occurrence statistics." In: *European Conference on Computer Vision*. Springer. 2010, pp. 239–253.
- [70] L'ubor Ladickÿ, Chris Russell, Pushmeet Kohli, and Philip HS Torr. "Graph cut based inference with co-occurrence statistics." In: *European Conference on Computer Vision*. Springer. 2010, pp. 239–253.
- [71] L'ubor Ladickÿ, Paul Sturgess, Karteek Alahari, Chris Russell, and Philip HS Torr. "What, where and how many? combining object detectors and crfs." In: *European conference on computer vision*. Springer. 2010, pp. 424–437.
- [72] Lubor Ladickÿ, Paul Sturgess, Chris Russell, Sunando Sengupta, Yalin Bastanlar, William Clocksin, and Philip HS Torr. "Joint optimization for object class segmentation and dense stereo reconstruction." In: *International Journal of Computer Vision* (2012), pp. 1–12.
- [73] Steffen L Lauritzen and David J Spiegelhalter. "Local computations with probabilities on graphical structures and their application to expert systems." In: *Journal of the Royal Statistical Society. Series B (Methodological)* (1988), pp. 157–224.
- [74] Eugene L Lawler. "A procedure for computing the k best solutions to discrete optimization problems and its application to the shortest path problem." In: *Management science* 18.7 (1972), pp. 401–405.
- [75] Jonathan Long, Evan Shelhamer, and Trevor Darrell. "Fully convolutional networks for semantic segmentation." In: *Proceedings of the IEEE Conference on Computer Vision and Pattern Recognition*. 2015, pp. 3431–3440.
- [76] David G Lowe. "Object recognition from local scale-invariant features." In: *Computer vision, 1999. The proceedings of the seventh IEEE international conference on*. Vol. 2. Ieee. 1999, pp. 1150–1157.

- [77] Michael Maire, Pablo Arbeláez, Charless Fowlkes, and Jitendra Malik. "Using contours to detect and localize junctions in natural images." In: *Computer Vision and Pattern Recognition, 2008. CVPR 2008. IEEE Conference on*. IEEE. 2008, pp. 1–8.
- [78] Jitendra Malik, Serge Belongie, Jianbo Shi, and Thomas Leung. "Textons, contours and regions: Cue integration in image segmentation." In: *Computer Vision, 1999. The Proceedings of the Seventh IEEE International Conference on*. Vol. 2. IEEE. 1999, pp. 918–925.
- [79] Marcin Marszalek and Cordelia Schmid. "Accurate object localization with shape masks." In: *Computer Vision and Pattern Recognition, 2007. CVPR'07. IEEE Conference on*. IEEE. 2007, pp. 1–8.
- [80] Jiri Matas, Ondrej Chum, Martin Urban, and Tomáš Pajdla. "Robust wide-baseline stereo from maximally stable extremal regions." In: *Image and vision computing 22.10* (2004), pp. 761–767.
- [81] Mohammadreza Mostajabi and Iman Gholampour. "A framework based on the Affine Invariant Regions for improving unsupervised image segmentation." In: *ISSPA*. 2012.
- [82] Mohammadreza Mostajabi, Payman Yadollahpour, and Gregory Shakhnarovich. "Feedforward semantic segmentation with zoom-out features." In: *Proceedings of the IEEE Conference on Computer Vision and Pattern Recognition*. 2015, pp. 3376–3385.
- [83] Roozbeh Mottaghi. "Augmenting deformable part models with irregular-shaped object patches." In: *Computer Vision and Pattern Recognition (CVPR), 2012 IEEE Conference on*. IEEE. 2012, pp. 3116–3123.
- [84] Dennis Nilsson. "An efficient algorithm for finding the M most probable configurations in probabilistic expert systems." In: *Statistics and computing 8.2* (1998), pp. 159–173.
- [85] Timo Ojala, Matti Pietikäinen, and David Harwood. "A comparative study of texture measures with classification based on featured distributions." In: *Pattern recognition 29.1* (1996), pp. 51–59.
- [86] Timo Ojala, Matti Pietikainen, and Topi Maenpaa. "Multiresolution gray-scale and rotation invariant texture classification with local binary patterns." In: *IEEE Transactions on pattern analysis and machine intelligence 24.7* (2002), pp. 971–987.
- [87] George Papandreou and Alan L Yuille. "Perturb-and-map random fields: Using discrete optimization to learn and sample from energy models." In: *Computer Vision (ICCV), 2011 IEEE International Conference on*. IEEE. 2011, pp. 193–200.
- [88] Dennis Park and Deva Ramanan. "N-best maximal decoders for part models." In: *2011 International Conference on Computer Vision*. IEEE. 2011, pp. 2627–2634.

- [89] Jacob Porway and Song-Chun Zhu. "C⁴: Exploring Multiple Solutions in Graphical Models by Cluster Sampling." In: *IEEE transactions on pattern analysis and machine intelligence* 33.9 (2011), pp. 1713–1727.
- [90] Ruifang Ge Raymond and J Mooney. "Discriminative reranking for semantic parsing." In: *Proceedings of the COLING/ACL on Main conference poster sessions*. Association for Computational Linguistics. 2006, pp. 263–270.
- [91] Jos BTM Roerdink and Arnold Meijster. "The watershed transform: Definitions, algorithms and parallelization strategies." In: *Fundamenta informaticae* 41.1, 2 (2000), pp. 187–228.
- [92] Amir Rosenfeld and Daphna Weinshall. "Extracting foreground masks towards object recognition." In: *Computer Vision (ICCV), 2011 IEEE International Conference on*. IEEE. 2011, pp. 1371–1378.
- [93] Carsten Rother, Vladimir Kolmogorov, and Andrew Blake. "Grabcut: Interactive foreground extraction using iterated graph cuts." In: *ACM transactions on graphics (TOG)*. Vol. 23. 3. ACM. 2004, pp. 309–314.
- [94] Carsten Rother, Tom Minka, Andrew Blake, and Vladimir Kolmogorov. "Cosegmentation of image pairs by histogram matching-incorporating a global constraint into mrfs." In: *Computer Vision and Pattern Recognition, 2006 IEEE Computer Society Conference on*. Vol. 1. IEEE. 2006, pp. 993–1000.
- [95] Carsten Rother, Pushmeet Kohli, Wei Feng, and Jiaya Jia. "Minimizing sparse higher order energy functions of discrete variables." In: *Computer Vision and Pattern Recognition, 2009. CVPR 2009. IEEE Conference on*. IEEE. 2009, pp. 1382–1389.
- [96] Olga Russakovsky et al. "ImageNet Large Scale Visual Recognition Challenge." In: *International Journal of Computer Vision (IJCV)* 115.3 (2015), pp. 211–252. DOI: [10.1007/s11263-015-0816-y](https://doi.org/10.1007/s11263-015-0816-y).
- [97] Bryan C Russell, William T Freeman, Alexei A Efros, Josef Sivic, and Andrew Zisserman. "Using multiple segmentations to discover objects and their extent in image collections." In: *Computer Vision and Pattern Recognition, 2006 IEEE Computer Society Conference on*. Vol. 2. IEEE. 2006, pp. 1605–1614.
- [98] Chris Russell, Pushmeet Kohli, Philip HS Torr, et al. "Exact and approximate inference in associative hierarchical networks using graph cuts." In: *arXiv preprint arXiv:1203.3512* (2012).
- [99] Chris Russell, Pushmeet Kohli, Philip HS Torr, et al. "Exact and approximate inference in associative hierarchical networks using graph cuts." In: *arXiv preprint arXiv:1203.3512* (2012).
- [100] Koen EA Van de Sande, Jasper RR Uijlings, Theo Gevers, and Arnold WM Smeulders. "Segmentation as selective search for object recognition." In: *Computer Vision (ICCV), 2011 IEEE International Conference on*. IEEE. 2011, pp. 1879–1886.

- [101] Benjamin Sapp, Alexander Toshev, and Ben Taskar. "Cascaded models for articulated pose estimation." In: *European conference on computer vision*. Springer. 2010, pp. 406–420.
- [102] Yaar Schnitman, Yaron Caspi, Daniel Cohen-Or, and Dani Lischinski. "Inducing semantic segmentation from an example." In: *Asian conference on computer vision*. Springer. 2006, pp. 373–384.
- [103] Libin Shen, Anoop Sarkar, and Franz Josef Och. "Discriminative reranking for machine translation." In: *HLT-NAACL*. 2004, pp. 177–184.
- [104] Jianbo Shi and Jitendra Malik. "Normalized cuts and image segmentation." In: *IEEE Transactions on pattern analysis and machine intelligence* 22.8 (2000), pp. 888–905.
- [105] Naum Zuselevich Shor. *Minimization methods for non-differentiable functions*. Vol. 3. Springer Science & Business Media, 2012.
- [106] Jamie Shotton, John Winn, Carsten Rother, and Antonio Criminisi. "Textonboost: Joint appearance, shape and context modeling for multi-class object recognition and segmentation." In: *European conference on computer vision*. Springer. 2006, pp. 1–15.
- [107] Jamie Shotton, John Winn, Carsten Rother, and Antonio Criminisi. "Textonboost for image understanding: Multi-class object recognition and segmentation by jointly modeling texture, layout, and context." In: *International Journal of Computer Vision* 81.1 (2009), pp. 2–23.
- [108] Karen Simonyan and Andrew Zisserman. "Very deep convolutional networks for large-scale image recognition." In: *arXiv preprint arXiv:1409.1556* (2014).
- [109] Vikas Sindhwani and S Sathiya Keerthi. "Large scale semi-supervised linear SVMs." In: *Proceedings of the 29th annual international ACM SIGIR conference on Research and development in information retrieval*. ACM. 2006, pp. 477–484.
- [110] Paul Sturgess, Karteek Alahari, Lubor Ladicky, and Philip HS Torr. "Combining appearance and structure from motion features for road scene understanding." In: *BMVC 2012-23rd British Machine Vision Conference*. BMVA. 2009.
- [111] Daniel Tarlow, Inmar E Givoni, and Richard S Zemel. "HOP-MAP: Efficient Message Passing with High Order Potentials." In: *AISTATS*. Vol. 5. 2010, p. 6.
- [112] Daniel Tarlow and Richard S Zemel. "Structured Output Learning with High Order Loss Functions." In: *AISTATS*. 2012, pp. 1212–1220.
- [113] Daniel Tarlow, Kevin Swersky, Richard S Zemel, Ryan Prescott Adams, and Brendan J Frey. "Fast exact inference for recursive cardinality models." In: *arXiv preprint arXiv:1210.4899* (2012).
- [114] Ioannis Tsochantaridis, Thorsten Joachims, Thomas Hofmann, and Yasemin Altun. "Large margin methods for structured and interdependent output variables." In: *Journal of machine learning research* 6.Sep (2005), pp. 1453–1484.

- [115] Jasper Uijlings, Koen van de Sande, Arnold Smeulders, Theo Gevers, Nicu Sebe, and Cees Snoek. "The Most Telling Window for Image Classification." In: *ICCV Pascal VOC Workshop*. 2011.
- [116] Andrea Vedaldi and Stefano Soatto. "Quick shift and kernel methods for mode seeking." In: *European Conference on Computer Vision*. Springer. 2008, pp. 705–718.
- [117] Paul Viola and Michael J Jones. "Robust real-time face detection." In: *International journal of computer vision* 57.2 (2004), pp. 137–154.
- [118] Martin J Wainwright, Tommi S Jaakkola, and Alan S Willsky. "MAP estimation via agreement on trees: message-passing and linear programming." In: *IEEE transactions on information theory* 51.11 (2005), pp. 3697–3717.
- [119] Martin J Wainwright, Michael I Jordan, et al. "Graphical models, exponential families, and variational inference." In: *Foundations and Trends® in Machine Learning* 1.1–2 (2008), pp. 1–305.
- [120] Song Wang and Jeffrey Mark Siskind. "Image segmentation with ratio cut." In: *IEEE Transactions on Pattern Analysis and Machine Intelligence* 25.6 (2003), pp. 675–690.
- [121] David J Weiss and Benjamin Taskar. "Structured Prediction Cascades." In: *AISTATS*. 2010, pp. 916–923.
- [122] David Weiss, Benjamin Sapp, and Ben Taskar. "Sidestepping intractable inference with structured ensemble cascades." In: *Advances in Neural Information Processing Systems*. 2010, pp. 2415–2423.
- [123] Tomas Werner. "A linear programming approach to max-sum problem: A review." In: *IEEE transactions on pattern analysis and machine intelligence* 29.7 (2007), pp. 1165–1179.
- [124] Zifeng Wu, Chunhua Shen, and Anton van den Hengel. "Wider or Deeper: Revisiting the ResNet Model for Visual Recognition." In: *CoRR* abs/1611.10080 (2016). URL: <http://arxiv.org/abs/1611.10080>.
- [125] Payman Yadollahpour, Dhruv Batra, and Gregory Shakhnarovich. "Discriminative re-ranking of diverse segmentations." In: *Proceedings of the IEEE Conference on Computer Vision and Pattern Recognition*. 2013, pp. 1923–1930.
- [126] Payman Yadollahpour and Gregory Shakhnarovich. "Region ranking for figure-ground segmentation." 2014.
- [127] Chen Yanover and Yair Weiss. "Finding the M most probable configurations using loopy belief propagation." In: *Advances in neural information processing systems* 16 (2004), p. 289.
- [128] Jian Yao, Sanja Fidler, and Raquel Urtasun. "Describing the scene as a whole: Joint object detection, scene classification and semantic segmentation." In: *Computer Vision and Pattern Recognition (CVPR), 2012 IEEE Conference on*. IEEE. 2012, pp. 702–709.

- [129] Hengshuang Zhao, Jianping Shi, Xiaojuan Qi, Xiaogang Wang, and Jiaya Jia. "Pyramid Scene Parsing Network." In: *arXiv preprint arXiv:1612.01105* (2016).

Part I

APPENDIX

A

APPENDIX A

A.1 SAMPLE OF DIVMBEST SOLUTIONS FROM FIGURE-GROUND MODEL

For overall document size considerations the results in this appendix section have been moved to <http://ttic.uchicago.edu/~pyadolla/papers/thesis.pdf>.

A.2 SAMPLE OF RESULTS WHEN DIVMBEST IS APPLIED TO MULTI-CATEGORY SEGMENTATION

For overall document size considerations the results in this appendix section have been moved to <http://ttic.uchicago.edu/~pyadolla/papers/thesis.pdf>.

B

APPENDIX B

B.1 EXAMPLE RE-RANKING RESULTS

For overall document size considerations the results in this appendix section have been moved to <http://ttic.uchicago.edu/~pyadolla/papers/thesis.pdf>.

B.2 HIGHEST RANKED VS. MAP

For overall document size considerations the results in this appendix section have been moved to <http://ttic.uchicago.edu/~pyadolla/papers/thesis.pdf>.